SYNTHESIS OF SAMARIUM DOPED TiO_2 CATALYSTS FOR PHOTODREGADATION OF POLYCYCLIC AROMATIC HYDROCARBONS (PAHs)

INTRODUCTION

Recently, Titania (TiO_2) is an effective and widely use as photocatalyst for degradation of many organic compounds. Due to its good properties such as mechanical, thermal and anticorrosive properties, therefore its can be use as good catalyst for oxidation or photodegradation reaction. However, there is disadvantage of TiO_2, high band gap energy (3.2 eV), which limits its wide application in the visible light range also the charge carrier recombination and phase transfer occurs very fast, as a consequence, its photocatalytic properties is limited.

There were many reports that the doping of various transition metal can effectively modify the properties of TiO_2. Lanthanide doped TiO_2 has attracted more attention due to the many profitable potential application in photoelectric devices and optical communication. This interest is mainly due to their optical properties. Some important results were achieved in research on lanthanide doped TiO_2. For example, TiO_2 doped with Er(III) and Nd(III) have an intense characteristic emission in the infrared region. Moreover, phase transition from anatase to rutile phase was decrease. The crystallize size of doped catalyst may also decrease, then it has more effective properties as a consequence (Saif, 2007)

OBJECTIVES

1. To study the effect of doping Sm on the photocatalytic activities of TiO_2. Synthesized Sm doped TiO_2 catalysts were characterized and reported their properties.

2. To compare the catalytic activity between undoped TiO_2 catalyst and various Sm doped TiO_2 catalysts for photodegradation of PAHs such as phenanthrene and benzo[a]anthracene in visible light range and studies the effect of Sm doping with different percentage.

LITERATURE REVIEW

1. Photocatalysis

The photocatalysis is the catalysis reaction using photocatalyst which can eliminate harmful substances such as organic compounds via oxidation reaction under the light at various wavelengths. The catalyst component is oxides and cation which have several oxidation state and can be rapidly reduced and reoxidized.

The function of the photocatalyst can be divided into five major categories as follows:

1. Purifying water
2. Preventing contamination
3. Anti-bacteria
4. Deodorizing
5. Purifying the air

The performance of catalyst is judged from its activities, selectivity and stability. These properties are influenced by many physical and chemical variables. Thus, each catalyst should be characterized the properties before use to know that each catalyst can be compatible with different reaction.

2. Titanium dioxide (TiO_2)

Titanium(IV)oxide or titania (TiO_2) is widely used in industrial applications as a catalyst support, dye-sensitized photoelectrochemical solar cells, ingredient in cosmetic products such as sunscreens, lipsticks, body powder and also use as photocatalyst. It has been used for oxidation of various organic compounds due to its good properties, nontoxic and long time stability. TiO_2 is white pigment, has three

common polymorphs as tetragonal rutile, tetragonal anatase and orthorhombic brookite as shown in Figure 1. The properties of TiO_2 also presents in Table 1.

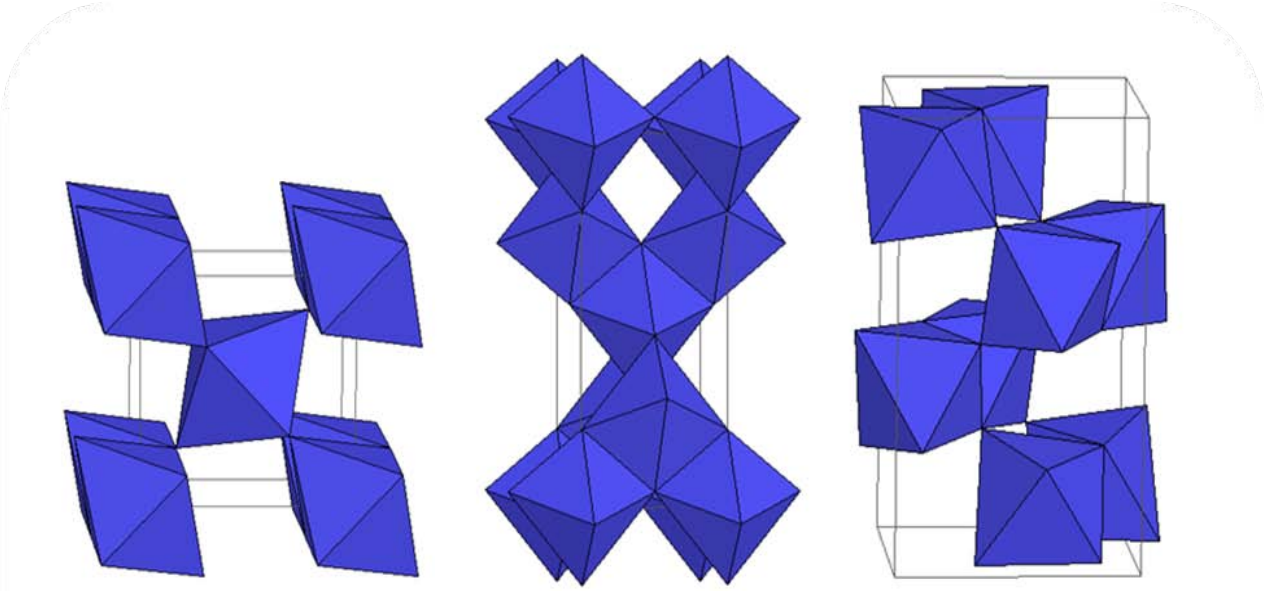

(a) (b) (c)

Figure 1 3-D structure of TiO_2 unit cell. (a) tetragonal rutile, each of TiO_6 unit cell share neighbor edges, (b) tetragonal anatase and (c) orthorhombic brookite, each of TiO_6 unit cell share neighbor conners in both structure.

Source: Smyth (2009)

Table 1 Properties of TiO_2.

Properties	Parameters
Density	4 g/cm^3
Thermal expansion (from room temp. to 1000^{o}C)	9 x 10^{-6} K^{-1}
Thermal conductivity (at 25^{o}C)	11.7 W m^{-1} K^{-1}
Melting point	1843 ^{o}C
Boiling point	2927 ^{o}C
Band gap energy	~ 3.05-3.26 eV
Toxicity	Low
Solubility in water	Insoluble
Characteristic	White powder or crystal

Source: Winter (1993)

The structures of rutile, anatase and brookite can be discussed in terms of (TiO_6^{2-}) octahedrals. The three crystal structures differ by the distortion of each octahedral and by the patterns of the octahedral chains. Anatase are connected by their vertices, in rutile, the edges are connected, and in brookite, both vertices and edges are connected (Crap *et al*., 2004).

The anatase form is more active than two other forms due to its structure is conner share. Then, it was widely used as photocatalyst for various organic compounds. However, there is disadvantage of anatase form. It can be distorted in the structure against the high temperature (550-1000^{o}C). Then it has poor thermal stability at high temperature. As a result, the phase transformation from anatase to rutile would occur and surface area decreases. As decreasing of surface area, the catalytic activity also decreases. Then, to improve the properties of anatase TiO_2, doping with transition metal can enhance the efficiency of its.

3. Doping

Doping the TiO_2 with various transition metal ions may lead to enhanced the efficiency of the photocatalytic systems (Carp *et al*., 2004). This method of improving photocatalytic activity is mainly used in aqueous media.TiO_2 particles can be simply substituted or interstitial doped with different cations to form mixed oxides or a mixture of oxides. The effect of metal ion dopants, concentration of dopants and the temperature treatment have effect on the photocatalytic activity. The alteration of the photocatalytic activity is made up from these changes which occur in:

a) the light absorption of TiO_2 photocatalyst
b) adsorption capacity of substrate molecules on the surface of catalyst
c) interfacial charge transfer rate (e^-/h^+ recombination)

Many results were reported that the method of doping leads to different morphology and crystalline properties of the photocatalyst. Impregnation, coprecipitation and sol–gel methods are used to introduce dopant into the catalyst structure. Different dopant and dopant content also have directly influenced to the properties of photocatalyst such as e^-/h^+ recombination rate (Xie *et al*., 2005).

To improve the thermal stability of TiO_2, it can be doped other atoms into TiO_2 in order to decrease the thermal expansion. However, TiO_2 has wide band gap energy (3.2 eV for anatase) and high e^-/h^+ recombination rate (Xiao *et al*., 2007), means that these disadvantages also have to be improved. To solve the problems, one of several approaches is doping lanthanide ion with 4f electron configuration into TiO_2 lattice, which could eliminate or retard the recombination of electron-hole significantly and also extend the wavelength response toward visible region.

Recently, there were many reports used lanthanide metals for doping on TiO_2 catalyst. The results showed that lanthanide ion could improve the properties of catalyst toward photocatalytic reaction of various organic compounds as show below.

Xie *et al*. (2004) prepared TiO_2 doped with Nd^{3+} ion by coprecipitation–peptization method. The particles were distributed in colloidal system with average size of nm. The conversion of Nd doped TiO_2 from amorphous to crystalline phase was achieved at 62 ^oC and pH 1.0 within 12 hours. Photocatalytic activity of Nd doped TiO_2 was evaluated by photodegradation of Phenol under visible light. It was found that concentration of phenol decreased from 100 mg/l to 5.29 mg/l. This result indicated that Nd doped TiO_2 nanoparticles exhibited photocatalytic activity in the visible range. Nd^{3+} ion in TiO_2 structure introduced electron state into the band gap of TiO_2 to form the new lowest unoccupied molecular orbital. Band gap of TiO_2 can be reduced by Nd doping, as a consequence. The reaction mechanism of Nd doped TiO_2 in photocatalysis reaction was also proposed.

Xie *et al*. (2005) also attempted to improve the photocatalytic activity of TiO_2 catalysts and extend the light absorption towards the visible light region, three types of the lanthanide ion doped TiO_2 catalysts were prepared by coprecipitation–peptization mathod. The structure and morphology of Ln doped TiO_2 catalysts were characterized by atomic force microscope (AFM), particle size distribution, and X-ray diffraction spectroscopy. The results showed that these catalysts had better particles distribution and interfacial adsorption ability than the powder catalysts in suspension. The photocatalytic degradation of azo dye (X-3B) was studied to determine photocatalytic activity of the crystallized Ln doped TiO_2 catalysts. The results showed that both TiO_2 and Ln doped TiO_2 catalysts have higher photocatalytic activity than Deggusa P-25 TiO_2 powder catalyst significantly. The experiments also confirmed that the modification of TiO_2 with lanthanide ions doping can improve the efficiency of interfacial adsorption and photocatalytic reactivity with azo dye. The photoresponse of catalysts under visible light showed that the Ln doped TiO_2 catalysts had significant absorption to visible light.

Zhang *et al*. (2005) prepared a series of $Nd^{3+,}$, Pr^{3+}, Er^{3+} and Dy^{3+} (0.25–5 %) doped TiO_2 by sol–gel technique, and the effect of lanthanide doping on the photocatalytic activity in the degradation of Rhodamine B (RB) in aqueous solution was studied. Concentration of the lanthanide dopant and calcination temperature

showed significant affect to the photodegradation of RB. The photocatalytic activity of pure TiO_2 was decreased when it was calcined at 700 °C, while the high photocatalytic activity was still maintained in Ln doped TiO_2. HPLC-MS method was used to study the degradation process. The results showed that the photocatalytic degradation of RB via Ln doped TiO_2 was a stepwise de-ethylation photochemical process.

Iliev *et al*. (2006) modified the commercially TiO_2 catalyst (Degussa P-25) with nanosized Pt and Ag particles by the photoreduction method to obtain different metal loading (0.5 and 1 wt.%). The characterization of synthesized catalysts were carried out by BET method, XPS, TEM and the adsorption of the model pollutant. The photodegradation of oxalic acid using TiO_2 modified with nanosized Pt or Ag particles was studied in aqueous solution. The photocatalytic activity of modified TiO_2 is approximately double compare to unmodified TiO_2. The adsorption properties of the catalysts influence to the efficiency of the photocatalytic process. The reaction rate of photocatalytic degradation of the oxalic acid follows a zero kinetic order according to the Langmuir–Hinshelwood model. The formation of Schottky barriers on the metal dopant–TiO_2 interface can serve as efficient electron traps, preventing the e^-/h^+ recombination.

In this work, Samarium was chosen to improve the properties of TiO_2 by acting as active species loaded on TiO_2 preparing by sol-gel method. Due to Sm is the effective catalyst using for oxidation reaction of organic compounds (Xiao, 2007) which has widely application and has appropriate properties (shows in Table 2). As expectation, Sm doping could improve the activity and light sensitivity of TiO_2 for photocatalytic degradation of polycyclic aromatic hydrocarbons (PAHs) compounds under visible light.There were reports used Sm for doping on TiO_2 catalyst. The results showed that Sm could improve the properties of catalyst toward photocatalytic reaction of various organic compounds.

Xiao *et al*. (2007) studied the photocatalytic activity of Sm doped TiO_2 which prepared by sol–gel technique under visible light. The prepared catalysts were

characterized by X-ray diffraction (XRD), UV–vis diffuse reflectance spectroscopy and photoluminescence (PL) spectra. UV–vis diffuse reflectance spectra showed that slightly shift to longer wavelengths and extension of the absorption in the visible region for almost all Sm doped TiO_2 were occured, compared to undoped TiO_2. The results from photodegradation of methylene blue (MB) over TiO_2 doped with 0.5 mol% of Sm prepared at various calcination temperatures showed that the catalyst which calcinated at 600 $^{\circ}$C and consists of mixed phases with 51.61% rutile gave the highest photocatalytic activity. Doping with Sm significantly enhanced the photocatalytic activity for MB degradation under visible light because the larger specific surface area and the lower e^-/h^+ recombination rate.

Saif (2007) was successfully synthesized mesoporous Ln doped TiO_2 (Ln = Tb, Eu, Sm) nanomaterials by using sol-gel technique. XRD, FT-IR, SEM and Raman spectoscopy were used to characterize all prepared catalysts. The prepared Ln doped TiO_2 nanoparticles had anatase phase and exhibited Ti–O–Ln bond. The absorption spectra of all prepared samples reflected the increasing photoresponse of doped catalysts to visible light over pure TiO_2. Surface area was remarkably increased due to Ln doping. In addition, the commercially textile dye Remazol Red RB-133 degradation was used to determine the efficiency of the Ln(III)–TiO_2 photocatalysts. The Ln(III) doping could improve the photocatalytic activity over pure TiO_2.

Table 2 Properties of Samarium.

Properties	Parameters
Stable oxidation state	+2 or +3
Band gap	4.33 eV
Atomic radius	185 pm
Ionic radii	
Sm (II) 8- coordinate	141 pm
Sm(III) 6- coordinate, octahedral	109.8 pm
Sm(III) 8- coordinate	121.9 pm
Characteristic	silver-white metal
Application	- Compounds act as sensitizers for phosphors excited in the infrared. - Samarium oxide is catalytic for the dehydration and dehydrogenation of ethanol and used as catalyst in oxidation reaction of various organic compounds.
Melting point	1072 °C
Boiling point	1803 ^{o}C
Thermal conductivity:	13 W m^{-1} K^{-1}
thermal expansion:	12.7 x 10^{-6} K^{-1}

Source: Winter (1993)

4. The mechanism of TiO_2 in photocatalysis of organic compounds.

As shown in Figure 2, under light irradiation, the electron which occupied in valence band of TiO_2 catalyst was excited by photon at suitable frequency. Then the excited electron is changed into higher energy level, then hole (h^+) occur. Water in the solution of organic compounds react with h^+ to form hydroxyl radical (OH^-) which is the strong oxidizing agent. The hydroxyl radical then reacts with organic compounds which decompose to small molecule such as carbon dioxide and water. The excited electron can also react with oxygen to form superoxide anion (O_2^-) which can be generated hydroxyl radical. All reactions in photocatalytic process of TiO_2 are shown in Figure 3.

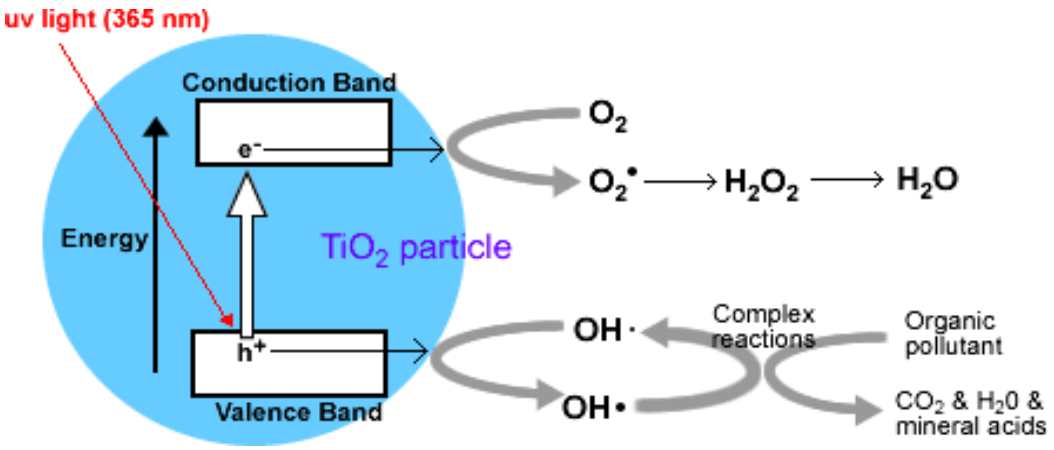

Figure 2 The mechanism of TiO_2 in catalytic photodegradation.

Source: Arena network (1995)

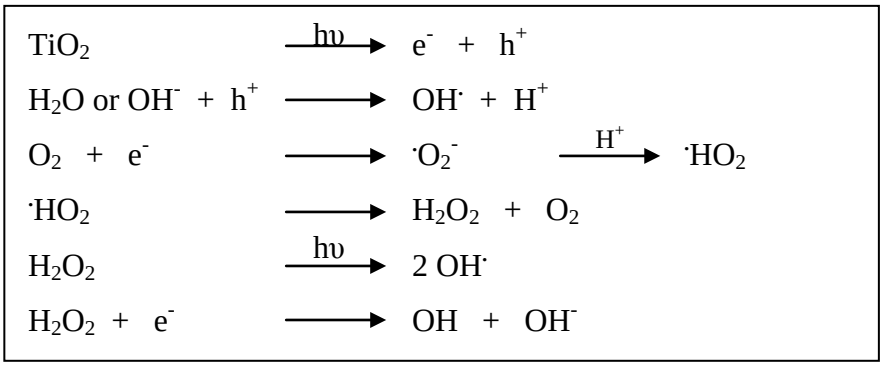

Figure 3 The reaction of TiO_2 in photocatalytic process.

Source: Carp *et al*. (2004)

The photocatalysis process of hydrocarcon compounds involve with radical cracking. First, carbon-carbon bonds undergo random homolysis results in radicals. The resulting redicals abstract hydrogen atom from other molecules to generate the most stable alkyl radical. The major reaction involves breaking of carbon-carbon bonds. The minor reaction occurring include isomerization and alkyl group transfer

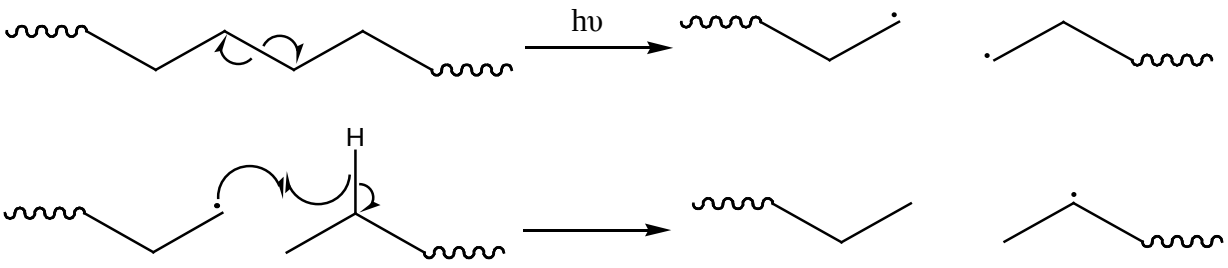

Figure 4 The photocatalytic cracking mechanism of organic compound.

5. Sol-gel method

Sol-gel is a simple method that produces ceramics and glasses with better purity than high temperature conventional process. Prepared materials have high homogeneity, small particle size and high surface area. In addition, this method is low temperature treatment and low cost. Sol-gel has produced a wide range of compositions in several forms, such as powders, fibers, coatings and porous membranes. The sol-gel process involves the hydrolysis (1) and condensation (2) or (3) of metal alkoxides.

$$\text{M-OR} + \text{HOH} \rightarrow \text{M-OH} + \text{ROH} \quad (1)$$
$$\text{M-OH} + \text{RO-M} \rightarrow \text{M-O-M} + \text{ROH} \quad (2)$$
$$\text{M-OH} + \text{HO-M} \rightarrow \text{M-O-M} + \text{HOH} \quad (3)$$

By carefully controlling the synthesis conditions, these reactions may lead to a variety of structures, and to different final states for the materials.

Sol-gel process involves the formation of sol followed by gel formation. Sol is a liquid suspension of solid particles in range of nanometer obtain by hydrolysis and condensation of precursor such as metal alkoxide. The condensation of sol particles produces a three dimensional gel network.

The advantage of sol-gel technique is as follows:

a) Simple method (single step)
b) High purity
c) Homogeneity
d) Low temperature treatment
e) Low pore size distribution
f) Able to control the particle size in nm range.

The four step in sol-gel preparation are as follows: formation of a gel, aging of a gel, removal of solvent and heat treatment.

5.1 The gel formation

The gel formation is initiated with hydrolysis to obtain reactive M-OH groups, then condensation occurs leading to the formation of M-O-M bond. As shown in previous equation. Hydrolysis and condensation are both nucleophillic displacement reactions, the reactivity of metal alkoxides depends on the positive partial charge of metal atom. The reaction rate depends on type and concentration of precursor. Also the amount of water using effects to the reaction rate and gel characteristics. The ratio of water : metal alkoxide must be suitable, gelation would not occur if there is not excess of water. Temperature and solvent are also important parameters.

5.2 Aging

Aging step is between the gel formation and the solvent removal. The cross- different structural linked network of gel was formed and extensive condensation causes the gel shrinked due to solvent being expelled which is a phenomenon called “syneresis”.

5.3 Drying

The pore liquids are evaporate from gel network, associate with capillary pressure of liquid interface within the pore. Using solvent with lower surface tension and supercritical or freeze drying can improve the drying step.

5.4 Calcination/Sintering

Heat treatment is necessary to burn off any residues of organic in gel. Heating is usually done in reactive gas. High temperature leads to sintering and consequently decreases in surface area. This process causes the gel material to crystallize and convert into different structural forms.

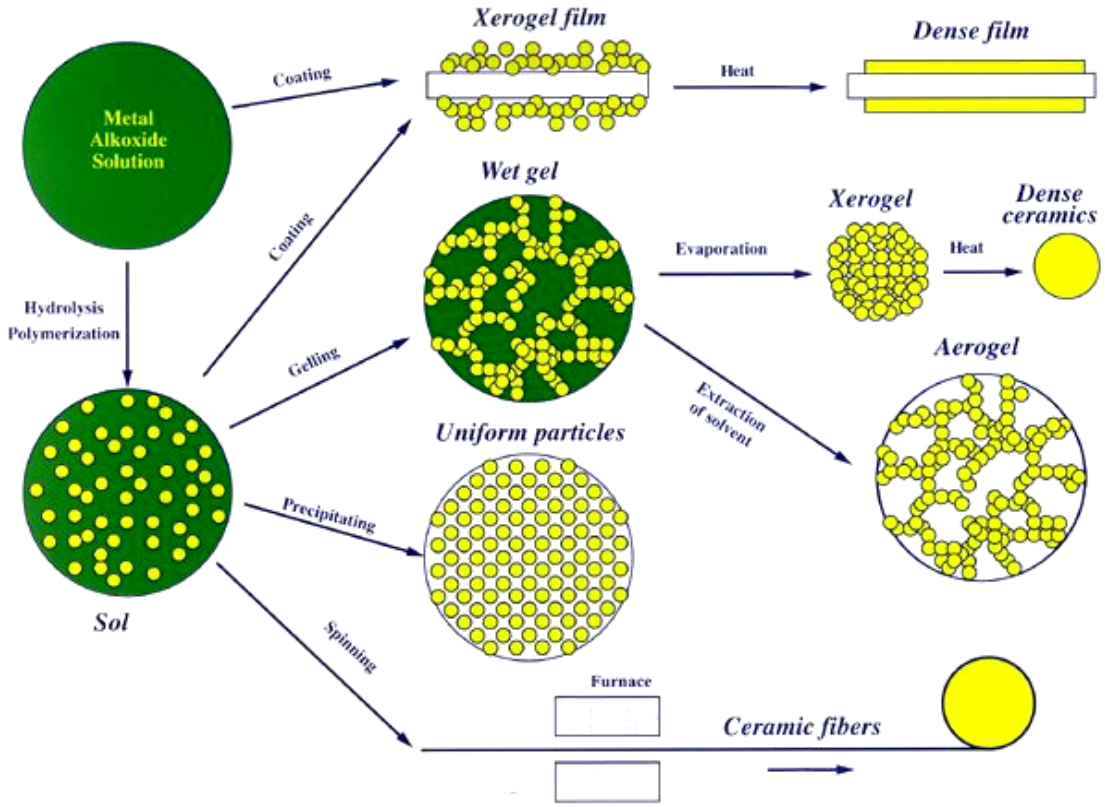

Figure 5 Diagram of sol-gel process and their applications.

Source: Sariyusriati (2008)

In every steps, there are many important parameters involve in sol-gel process as shown in Table 3

Table 3 Important parameters in the various step of sol-gel process.

Step	Important parameter
Solution chemistry	Type of precursor
	Type of solvent
	Water content
	Precursor concentration
	Temperature
	pH
Aging	Temperature
	Time
Drying	Drying method
	Temperature an heating rate
	Time
Calcination/sintering	Temperature an heating rate
	Time
	Gaseous environment

Due to many advantages of sol-gel method, There were reports used sol-gel process to prepared both pure TiO_2 and doped TiO_2 photocatalysts for photodegradation of various organic compounds under UV-visible light.

Pal *et al.* (2000) studied photocatalytic degradation of naphthalene and anthracene over thin films of porous TiO_2 particles on glass substrate, prepared by sol-gel process. Surface morphology and structure of all catalysts were studied by SEM, TEM and Raman spectroscopy. They found that the films were very efficient. Concentration decreased linearly with the irradiation time, and high rate constants were obtained for the degradation of these organic compounds. The pH of the solution

changed with the irradiation time due to the formation of intermediate photoproducts, e.g., 5,8-dihydroxynaphthaquinone, and 9,10-anthraquinone, etc.

Li *et al.* (2004) prepared La^{3+}–TiO_2 photocatalysts by doping lanthanum ion into TiO_2 structure by sol–gel process. The catalyst samples were characterized by XRD and XPS. The analytical results demonstrated that the lanthanum doping could inhibit the phase transformation of TiO_2 and enhance the thermal stability of TiO_2. In addition, it was found that the lanthanum doping could reduce the crystallite size and increase the Ti^{3+} content on the surface of the catalysts with the increase of lanthanum doping.With a purpose of odor control, 2-mercaptobenzothiazole (MBT) was used in this study as a model chemical and both the adsorption isotherm and photocatalytic activity of the La^{3+}–TiO_2 catalysts were evaluated based on the MBT photodegradation in aqueous solution. The kinetics of the MBT photodegradation using different La^{3+}–TiO_2 catalysts was studied. The experiments demonstrated that an optimum doping of lanthanum ion at 1.2% achieved the highest photodegradation rate. It was concluded that the enhancement of MBT photodegradation using the La^{3+}–TiO_2 catalysts mainly involved in both the improvement of the organic substrate adsorption in catalysts suspension and the enhancement of the separation of electron-hole pairs owing to the presence of Ti^{3+}.

Liqiang *et al*. (2004) prepared pure and La doped TiO_2 nanoparticles with different La content by a sol–gel process using $Ti(OC_4H_9)_4$ as raw material, and also were characterized by XRD, TG-DTA, TEM, XPS, DRS and Photoluminescence (PL) spectra. Mainly investigated the effects of calcining temperature and La content on the photocatalytic activity for degrading phenol. The results showed that La^{3+} did not enter into the crystal lattices of TiO_2 and was uniformly dispersed onto TiO_2 as the form of La_2O_3 particles with small size, which possibly made La dopant have a great inhibition on TiO_2 phase transformation. La doped TiO_2 nanoparticles calcined at 600^oC exhibited higher photocatalytic activity, indicating that 600^oC was an appropriate calcination temperature.

Yan *et al.* (2006) prepared anatase TiO_2 doped with Ce up to 5 %mol by sol–gel process. The precursor gel was characterized by infrared spectroscopy and TG/DSC analysis. The XPS measurement showed that Ce(III) was easily oxidized to Ce(IV) at 550 ^{o}C and above. The XRD data, XPS spectra, and TEM selected-area diffraction patterns confirmed that cerium(IV) formed a solid solution in the anatase TiO_2 powder. Doping of CeO_2 into TiO_2 shifted the phase transformation from anatase to rutile structure to a high temperature. When the Ce content was increased, the onset of optical absorption shifted to longer wavelength and extend absorption region in the UV- visible light.

6. Polycyclic Aromatic Hydrocarbons (PAHs)

Polycyclic aromatic hydrocarbons (PAHs) are widely well-known as toxicant organic compounds in environment, consisting of two or more fused benzene rings in linear, angular or cluster arrangement (as shown in Table 4). Substitution of carbon in benzene ring with nitrogen, sulfur, oxygen or other elements gives heterocyclic compounds which are also classified as PAHs. Crystalline solid of PAHs has high melting point and low vapor pressure. Unlike most hydrocarbons, PAHs are usually colored. PAHs are usually produced naturally by combustion processes, e.g. forest fires, volcanic activity and anthropogenically via industrial processes, particularly the combustion of fossil fuels for heating, power and transport. Many kinds of PAHs are strongly considered to be possible or probable human carcinogenic. Due to their properties, chronic health effect and carcinogenicity, microbial recalcitrance, high bioaccumulation potential and low removal efficiency in treatment process. Therefore, to study about how to remove or degrade these toxicant compounds is necessary. The USEPA has specified 16 PAHs compounds as priority pollutants: naphthalene, acenaphthylene, acenaphthene, fluorene, phenanthrene, anthracene, fluoranthene, pyrene, chrysene, benz [a]anthracene, benzo[b]fluoranthene, benzo[k]fluoranthene, benzo[a]pyrene, indeno[1,2,3-c,d]pyrene, benzo[g,h,i]perylene and dibenz[a,h]anthracene. Of these, eleven have been classified as animal carcinogens and all of their chemical structures shown in Figure 6.

There are many reports studied the photodegradation of PAHs compounds using TiO_2 as photocatalyst. Example of these works in Table 5. Almost of these works indicated that TiO_2 photocatalyst could improve the efficiency for photodegradation of PAHs under UV-visible light.

Table 4 Ring patterns and relative stabilities of PAHs.

Ring arrangement	Description	Stability	Example
linear	all rings in line	Least	anthracene naphthalene
cluster	at least one ring surrounded on the three side	intermediate	pyrene benzo[a]pyrene
angular	rings in steps	Most	phenanthrene

Source: Pal *et al.* (2000)

Table 5 Photocatalytic degradation of PAHs using TiO_2 catalyst.

Catalyst	Characterization technique	PAHs	Ref.
TiO_2	XRD Raman	mixture of 16 PAHs	Ireland et al. (1995)
TiO_2	XRD	benzo[a]pyrene	Miller et al. (2000)
TiO_2	SEM TEM Raman	naphthalene anthracene	Pal et al. (2000)
TiO_2	-	chrysene fluorene phenanthrene	Lin et al. (2003)
TiO_2	-	pyrene naphthalene	Garcia et al. (2006)

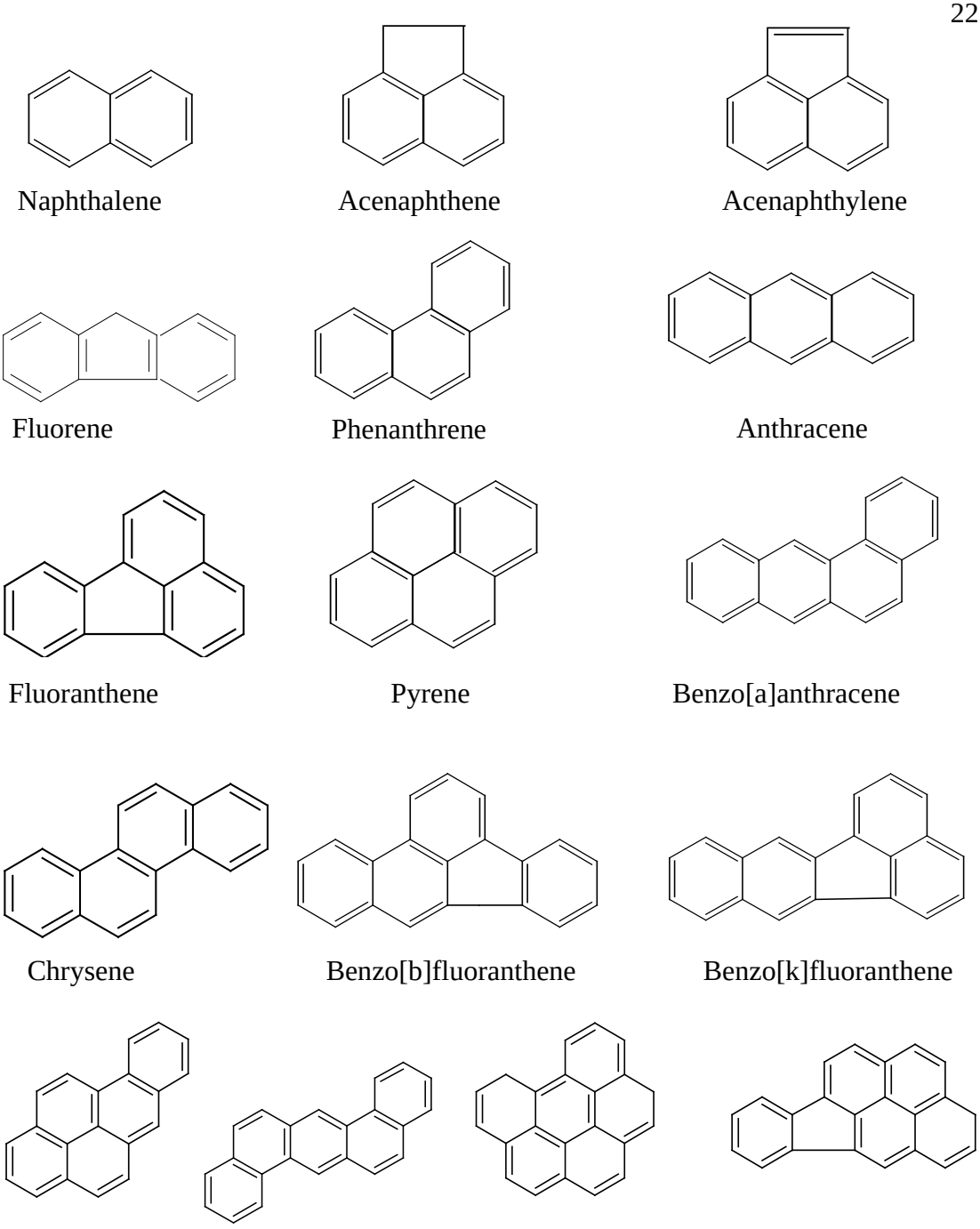

Figure 6 Chemical structures of the 16 PAHs identified by The Environmental Protection Agency (USEPA) as priority pollutants.

Source: Nagpal (1993)

7. Catalyst characterization

To determine the physical and chemical properties of catalyst. They can be identified by a few methods including spectroscopic techniques to obtain information on the physic chemical properties, such as X-ray diffraction spectroscopy (XRD), Raman spectroscopy, Scanning electron microscopy (SEM) and Thermogravimetric analysis (TGA), etc.

7.1 X-ray diffraction spectroscopy

X-ray diffraction spectroscopy (XRD) is commonly used to obtain information about the structure and composition of crystalline materials by comparison with reference patterns. Crystallize size of material can also be determined from X-ray diffraction peaks. The XRD pattern of a powdered sample is measured with a stationary X-ray source (Cu K_α) and moveable detector, which scans the intensity of diffracted radiation as a function of the angle 2Θ between the irradiation and diffracted beams as shown in Figure 4. An image of diffraction lines occurs because a small fraction to the powder samples will be oriented such that certain crystal plane is at the right angle Θ with the incident beam of constructive interference. The relation of a distance between two lattice plane (d) with an angle 2Θ is defied by Bragg's law

$$n\lambda = 2d\sin\Theta$$

where n : the integer called order of the reflection

λ : the wavelength of the X-rays

d : the distance between two lattice planes

Θ : the angle between the incident X-rays and the normal to the reflecting lattice plane

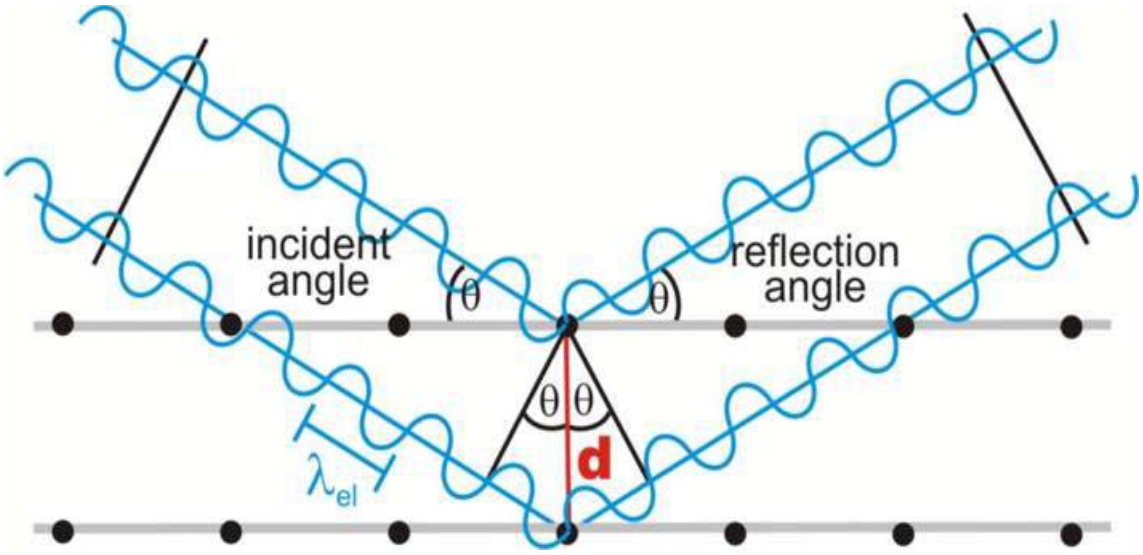

Figure 7 X-ray diffraction correspond to Bragg's law.

Source: Krumeich (2008)

The Bragg's law conditions are satisfied by different d spacing in crystalline materials. By plotting the angular positions and intensities of the resultant diffraction peaks produce a pattern which is characteristic of the sample. Where a mixture of different phase is present, the diffractogram is formed by addition of the individual pattern. The d-spacing of set of planes as the perpendicular distance between any pair of adjacent planes is correlated with unit cell parameters as show in Table 6. And the formula which used for unit cell volume calculation expresses in Table 7.

Table 6 Unit cell parameters of 7 crystal systems.

Crystal system	Unit cell shape	Formula
Cubic	$a = b = c$ $\alpha = \beta = \gamma = 90^o$	$\frac{1}{d^2} = \frac{h^2 + k^2 + l^2}{a^2}$
Tetragonal	$a = b \neq c$ $\alpha = \beta = \gamma = 90^o$	$\frac{1}{d^2} = \frac{h^2 + k^2}{a^2} + \frac{l^2}{c^2}$
Orthorhombic	$a \neq b \neq c$ $\alpha = \beta = \gamma = 90^o$	$\frac{1}{d^2} = \frac{h^2}{a^2} + \frac{k^2}{b^2} + \frac{l^2}{c^2}$
Hexagonal	$a = b \neq c$ $\alpha = \beta = 90^o$ $\gamma = 120^o$	$\frac{1}{d^2} = \frac{4}{3}\frac{h^2 + hk + k^2}{a^2} + \frac{l^2}{c^2}$
Trigonal (Rhombohedral)	$a = b = c$ $\alpha = \beta = \gamma \neq 90^o$	$\frac{1}{d^2} = \frac{(\sin^2\alpha)}{A^*}\frac{h^2 + k^2 + l^2}{a^2} + \frac{2(\cos^2\alpha - \cos\alpha)}{A}\frac{hk+hl+kl}{a^2}$ $^*A = (1 - 3\cos^2\alpha + 2\cos^3\alpha)$
Monoclinic	$a \neq b \neq c$ $\alpha = \gamma = 90^o$ $\beta \neq 90^o$	complex expressions
Triclinic	$a \neq b \neq c$ $\alpha \neq \beta \neq \gamma \neq 90^o$	complex expressions

Source: Wikipedia (2009)

Table 7 Unit cell volume of 7 crystal systems.

Crystal system	Unit cell volume
Cubic	a^3
Tetragonal	a^2c
Orthorhombic	abc
Hexagonal	$\sqrt{3a^2c} / 2$
Trigonal (Rhombohedral)	$a^3\sqrt{1 - 3\cos^2\alpha + 2\cos^3\alpha}$
Monoclinic	abc sinα
Triclinic	$abc \sqrt{1- \cos^2\alpha - \cos^2\beta - \cos^2\gamma + 2 \cos\alpha \cos\beta \cos\gamma}$

Source: Wikipedia (2009)

In catalyst characterization, diffraction patterns are mainly used to identify the crystal phases in catalysts. The information from diffraction peaks can be calculated the parameter of samples such as crystallize size, dimension of unit cell and crystal structure. The calculation will show in results and discussion part.

7.2 Raman spectroscopy

Raman scattering is used to obtain information about structures and properties of molecules from their vibrational transitions due to the change in the polarizability of the molecule with respect to its vibrational motion. When a polar molecule is irradiated by monochromatic light of frequency υ_i, then change in dipole moment in the molecule. The light scattered by the induced dipole of the molecule consists of Rayleigh scattering and Raman scattering two quanta of vibrational energy are involved simultaneously, either by addition or by subtraction. Rayleigh scattering

corresponds to the light scattered at the frequency of the incident radiation υ_i where as the Raman scattering is shift the frequency $\upsilon \pm \upsilon_i$, energy from the frequency of the incident radiation by the vibration energy that is gain or lost in the molecule. If the molecule gains vibrational energy as shown in Figure 8, the scattering is called Stokes Raman scattering $\upsilon - \upsilon_i$, where as if the molecule loses vibrational energy, the process is known as anti-Stokes Raman scattering $\upsilon + \upsilon_i$. Thus Raman spectra are presented as shifts from the incident frequency and call Raman shift $\Delta\upsilon$.

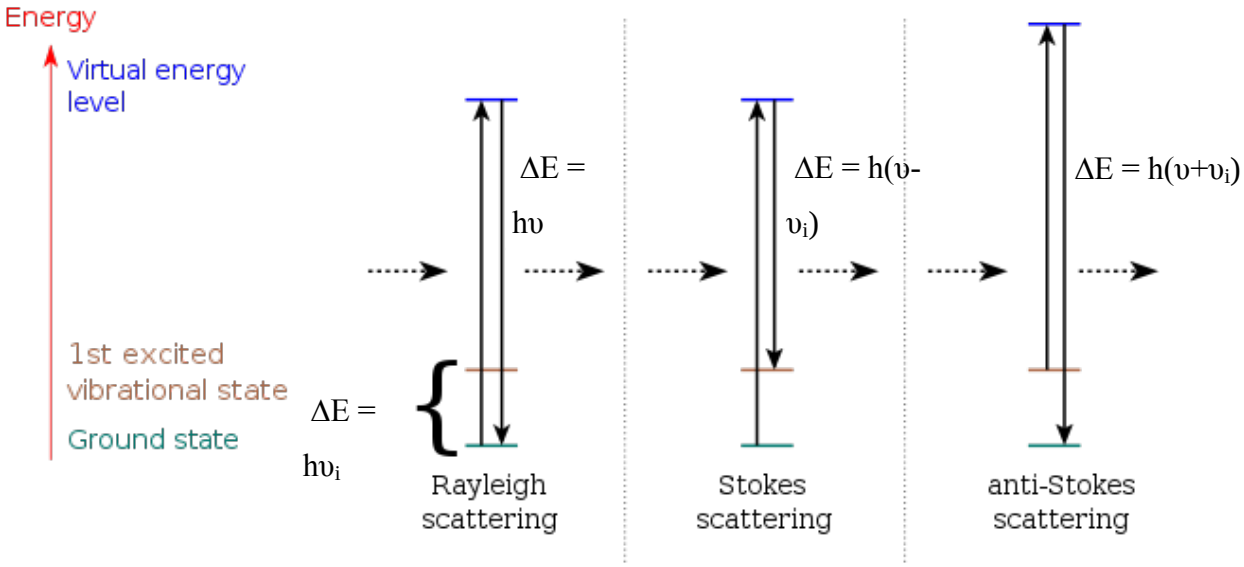

Figure 8 Energy diagram of vibrational transition in Raman scattering.

Source: Abhijeet (2008)

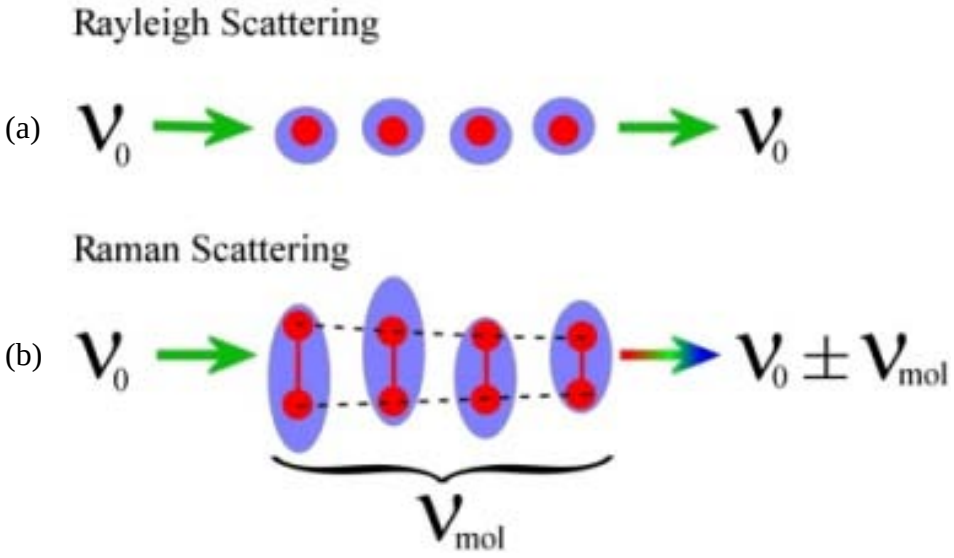

Figure 9 Vibrational transition in molecule changes the polarizability during (a) symmetric and (b) asymmetric stretching .

Source: Kelf (2005)

As has been described, Raman spectroscopy can obtain information about the vibrational spectrum of material. Then leads to identify the chemical composition in sample and also possible to deduce the structure of material for example, bond of each element and each atom in molecule from the usual vibrational frequencies.

7.3 Scanning electron microscopy and energy dispersive X-ray spectroscopy (SEM/EDX)

Scanning electron microscopy (SEM) is the important method to characterize the surface topography of sample. Electron beam from source was bombard on specimen then the scattering of incident beam occur with different types. Different elements and surface topography emit different amounts of electrons. These useful information can be transformed to image which consist of many spots with various intensity on the Cathode-ray tube that correspond to surface morphology and composition of sample. The advantages of SEM over light microscopy include greater

magnification (up to 100,000X) and much greater depth of field. The schematic of scanning electron microscope shows in Figure 10.

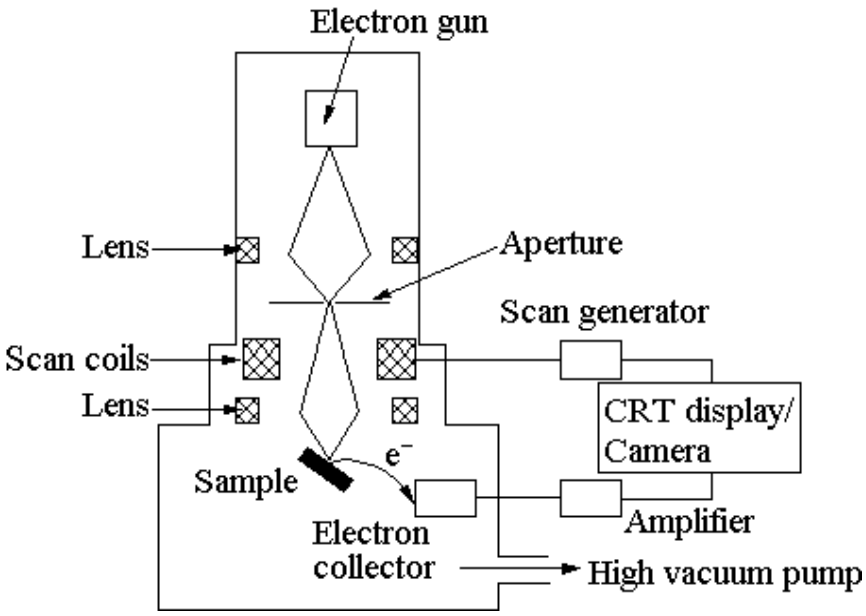

Figure 10 The schematic diagram of Scanning Electron Microscope (SEM).

Source: University of Bristol (2000)

In this work, SEM was used to characterize the surface morphology of TiO_2 catalysts which were prepared with different conditions also identified and quantified the element constituents of the sample by energy dispersive X-ray spectroscopy (EDS or EDX). EDX technique measures the number of characteristic X-rays produced by a solid sample when irradiated by electrons versus the energy of these X-rays. These X-rays are then gathered by the X-ray detector and converted into useful information. An image can be generated and these X-rays emitted from the specimen give information as to the elemental composition of the area. The EDS technique can detect elements from carbon (C) to uranium (U) in quantities as low as 1.0 wt%.

7.4 Transmission electron microscope (TEM)

Transmission electron microscopy (TEM) is a microscopy technique whereby a beam of electrons is transmitted through an ultra thin specimen, interacting with the specimen as it passes through. An image is formed from the interaction of the electrons transmitted through the specimen; the image is magnified and focused onto an imaging device, such as a fluorescent screen, on a layer of photographic film, or to be detected by a sensor such as a CCD camera. TEM columns must be kept under high vacuum to prevent electron beams which easy to be scattered by air molecules. Normally, SEM samples are thick enough for the focussed probe to be contained within the sample. In contrast, TEM samples should be thin enough to be beam transparent, so the ionization volume formed by a focussed probe is much smaller and, therefore, there is much less electron scattering. High beam energies (commonly between 100kV - 400kV) utilized in the analytical TEM also reduce beam scattering. However, due to the relatively small ionization volume, X-ray generation is much lower than for thick samples. The schematic diagram of transmission electron microscope showed in Figure 11.

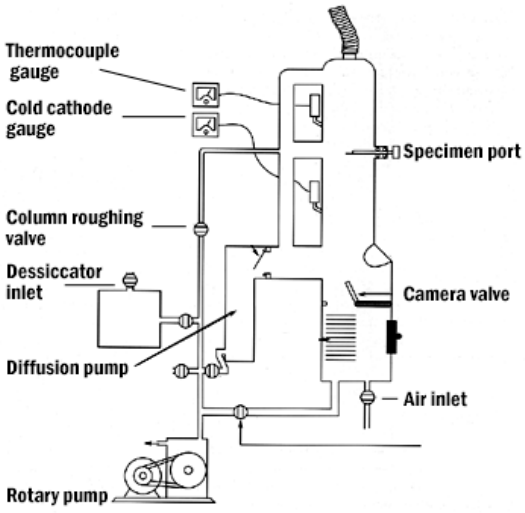

Figure 11 Schematic diagram of transmission electron microscope (TEM).

Source: Wikimedia commons (2008)

7.5 Surface area and porousity

Brunauer-Emmett-Teller (BET) method used to determine the surface area. It uses the information from amount of adsorbed nitrogen on the surface layer of sample which can be calculated from BET equation.

$$\frac{P}{V(P-P_0)} = \frac{1}{V_mC} + \frac{(C-1)P}{V_mCP_0}$$

where V = volume of gas adsorbed at Pressure P

V_m = volume of gas adsorbed in monolayer, same unit as V

P_0 = saturation pressure of adsorbate gas at the experiment temperature

C = a constant related exponentially to the heat of adsorption and liquefaction of gas

From BET equation a graph of $P/V(P_0-P)$ versus P/P_0 should give a straight line. Slope (s) and intercept (i) from linear curve can be used to calculate V_m and C as the following equation:

$$s = \frac{C-1}{V_mC}$$

$$i = \frac{1}{V_mC}$$

The total surface area S_t was calculated as equation:

$$S_t = \frac{V_mNA_{cs}}{M}$$

where N = Avogardro's number (6.02×10^{23} molecule/mol)

M = molecular weight of the adsorbate

A_{cs} = molecular cross-sectional area for nitrogen as 16.2 $Å^2$

The specific surface area (S) of the solid was calculated from the total surface area (S_t) and the sample weight (w), according to equation:

$$S = \frac{S_t}{w}$$

7.6 Thermogravimetric analysis (TGA)

Thermal analysis is a useful technique used to determine thermal stability and composition of solid compounds. When the sample is heated in an atmosphere of nitrogen, helium, air, other gases, or in vacuum with increasing temperature, the amount of weight change of material is measured. Inorganic materials, metals, polymers and plastics, ceramics, glasses, and composite materials can be analyzed. Samples can be analyzed in the form of powder or small pieces, so the interior sample temperature remains close to the measured gas temperature. The data from TGA is in the form of curve plot between %weight of sample versus temperature or time.

MATERIALS AND METHODS

Materials

1. Apparatus

1. X-ray Powder Diffractometer (XRD) Philips X´ Pert X-ray diffractometer
2. Thermal Gravimetric Analyzer (TGA) TGA 7 Perkin Elmer analyzer
3. Raman Imaging Microscope Renishaw Raman Imaging Microscope model 160 series
4. Diffuse Reflectance UV-Vis spectrophotometer (DRS) Perkin Elmer Lambda 650 spectrophotometer
5. Scanning Electron Microscope (SEM) Philips XL30 electron microscope
6. Transmission Electron Microscope (TEM) JEOL TEM 2010
7. Energy Dispersive X-ray spectrometer (EDX) EDAX
8. UV-Vis spectrophotometer Perkin Elmer Lambda 35
9. Luminescence spectrometer Perkin-Elmer LS 55
10. Photoreactor

2. Reagents

1. Titanium(IV) bis(ethyl acetoacetato)diisopropoxide ($C_{18}H_{34}O_8Ti$, Lab. Grade, Aldrich, St. Louis, USA)
2. Methanol (CH_3OH, Analytical Grade, BDH, Poole, England)
3. Acetylacetone ($C_4 H_6 O_3$**,** Analytical Grade, Fluka, Buchs, Switzerland)
4. Ethylene glycol ($C_2H_6O_2$, Lab. Grade, s.d. fine-chem limitted, Mumbai, India)
5. Phenanthrene ($C_{14}H_{10}$, HPLC Grade, Fluka, Buchs, Switzerland)
6. Benz[a]anthracene ($C_{18}H_{12}$, Lab. Grade, Fluka, Buchs, Switzerland)
7. Phenol (C_6H_5OH, Analytical Grade, Carlo Erba, Van de Reuil, France)
8. Samarium(III)acetyl acetonate hydrate (Lab. Grade, Aldrich, St. Louis, USA)

Methods

1. Preparation of catalysts

The Sol-gel synthesized TiO_2 doped Sm was prepared as follow : Titanium(IV)bis(ethylacetoacetato)diisopropoxide 4.2435 g (0.01mol) was added and stirred in acetylacetone 1 ml, ethylene glycol 3 ml and Samarium(III)acetylacetonate hydrate (0.0005-0.0040 mol). Deionized water 2 ml,was added to the mixture and subsequently then stirred under constant magnetic stirring until gel was formed. The sol mixture was dried at 120^{o}C for 5 hours to obtain dry gel. The gel was calcined at various temperatures from 400 to 800 ^{o}C for 2 hours to obtain the desired nanocatalyst. To study effect of Sm, different amount of Sm doping on TiO_2 was varied, shows in Table 8.

Table 8 Amount of Sm loaded on prepared Sm doped TiO_2 catalysts.

Catalyst	mol Ti	wt Ti (g)	mol Sm	wt Sm (g)	%wt Sm	%mol Sm
Sm-TiO_2	0.01	0.4787	0.0005	0.07518	13.57	5
Sm-TiO_2	0.01	0.4787	0.0010	0.15036	23.90	10
Sm-TiO_2	0.01	0.4787	0.0020	0.30072	38.58	20
Sm-TiO_2	0.01	0.4787	0.0040	0.60144	55.68	40

2. Catalyst characterization

The prepared catalyst was characterized by X-ray diffraction spectroscopy, Raman spectroscopy, Thermogravimetric analysis, UV-Vis reflectance to determined the properties of catalyst.

2.1 X-ray powder diffraction spectroscopy (XRD)

All powder catalysts were ground to fine particle and analyzed by a Philips Pw 1830 X-ray diffractometer operated at 40 kV and 35 mA and a Philips X´ Pert X-ray diffractometer operated at 40 kV and 30 mA, both equipped with Cu Kα radiation source at wavelength of 1.54 Å. The XRD data were scanned at 2θ from 20 degree to 70 degree with step size of 0.01 degree. The crystalline phases of all catalysts were confirmed by comparison with the Joint Committee on Powder Diffraction Standards (JCPDS) files.

2.2 Thermal Gravimetric Analysis (TGA)

TGA results were obtained from a TGA 7 Perkin Elmer analyzer. Approximately 4-5 mg of Al_2O_3 reference material was loaded to protect the damaging effect of samples on an alumina pan. This weight was set as zero and then about 10 mg of the powdered sample was added into the pan. The temperature program was set up from 0 to 1000^{o}C with heating rate of 10 ^{o}C /min and nitrogen purge.

2.3 Raman Spectroscopy

Si plate was used to calibrate Raman spectrum, which exhibited Raman shift at 520 cm^{-1}. All powder catalysts were ground to fine particle and then mounted onto the microscope slide glass. Raman spectra were obtained by a Renishaw Raman Imaging Microscope model 160 series operated with Ar^{+} 514.5 nm laser.

2.4 Diffuse Reflectance UV-Vis Spectrophotometry

Diffuse reflectance UV-vis spectra was obtained by a Perkin Elmer Lambda 650 spectrophotometer. All samples were ground to fine particle and then mounted on to the microscope slide glass. Scanning wavelength was in range from 200 nm to 800 nm with slit width of 2 nm.

2.5 Scanning Electron Microscopy and Energy Dispersive X-ray Spectroscopy (SEM/ EDX)

The surface morphology, particle size and the element constituents of all catalysts were determined by SEM recorded on a Philips XL30 electron microscope with tungsten filament electron source, operated at 12 kV. All samples were coated with Au atoms in a sputter coater to improve conductivity. Then they were mounted on SEM stubs by a mounting medium; Ag or Cu tape are most common.

2.6 Transmission electron microscope (TEM)

The morphology, particle size and size distribution of all catalysts were investigated by TEM. All of condensate products were examined by TEM on JEOL TEM 2010 electron microscope fitted with a standard tungsten filament and operated at 120 keV with resolution of 0.19 nm. The sample was prepared by suspending it in water, collecting a drop of the suspension on a small loop of wire and placing it onto a 3 mm carbon coated copper grid. This was then dried and placed into the microscope. Images were recorded digitally using a Mega View II digital camera with Soft Imaging System GmbH analysis 3.0 image analysis software and/or on KODAK Electron Image Film SO-163.

2.7 Surface area and pore size distribution via Brunauer-Emmett-Teller (BET) method.

Surface area and pore size distribution with N_2 adsorption were obtained by Quantachrome instrument model ASIC-2 and analyzed with Autosorp-1 program. Sample weight approximately 0.6 g was in a rod sample cell fitted at an outgas station and maintained at 300^{o}C for 20 hours under vacuum. Then, an empty P_0 cell was placed in a P_0 station. The sample cell and P_0 cell were inserted into the cold trap flasks which were filled with liquid nitrogen. The nitrogen adsorbed on sample surface was measured over a range of relative pressure (P/P_0) at constant temperature, the result was adsorption isotherm. Similarly, desorption isotherm was obtained by

measuring the amout of gas removed from the sample as a relative pressure. The surface area and porosity of samples were calculated by BET equation.

3. Photocatalytic degradation

The photodegradation experiment was carried out in a fixed bed type photocatalytic reactor (Figure 12). Photocatalytic was carried out using Xe arc lamp adjust at 90W and current adaptor has been used for the adjustment of AC 220V to DC 12V. The incident visible radiation from this lamp was filtered with HOYA UV 385 cutoff filter to eliminated light in the UV and IR region. Reaction was set up by adding 0.1 g of catalyst into 125 ml of 20 ppm sample solution. The solution was stirred in the dark for 1 hour at 30^{o}C after the addition of catalyst. Then the visible light was activated, 5 ml of sample was withdrawn every 30 min intervals for analysis of the undegraded compounds remain in the solution via UV-Vis spectrophotometer or Fluorescence spectrometer at characteristic wavelength of each PAHs.

3.1 Concentration measurement of sample after degradation

Phenanthrene were quantified by UV-Vis spectrophotometer Perkin Elmer Lambda 35 at maximum wavelength 251 nm, scanning rate 240 nm/min and slit width 2 nm. Benzo[a]anthracene were quantified by Luminescene spectrometer Perkin Elmer LS55 at excitation wavelength at 287 nm and emission wavelength at 527 nm. Excitation slit width 10 nm and emission slit width 2.5 nm with scanning rate 1000 nm/min. Phenol were quantified by UV-Vis spectrometer Perkin Elmer Lambda 35 at maximum wavelength 270 nm. All analysis were run under the same condition. Each sample was analyzed with 3 replicates, and the results were average data.

Figure 12 The photocatalytic reactor.

RESULTS AND DISCUSSION

1. Preparation of catalysts

Sol mixture of Titanium(IV)bis(ethylacetoacetato)diisopropoxide and Samarium(III) acetylacetonate hydrate consist of deionized water and ethylene glycol was stirred under constant magnetic stirring until gel was formed. In order to obtain nanoparticles, the gel was dried at 120^{o}C for 5 hours.

The prepared gel were calcined at various temperatures from 400 to 800 ^{o}C for 2 hours. The obtained nanocatalyst were characterized by XRD, Raman spectroscopy, TGA, SEM and UV-Vis reflectance spectrophotometry.

The appearance of catalyst was changed upon preparation. The color and phase of sol and gel change in each step, Figure 13 showed the sol-gel synthesis steps. Mixture solution of all precursors were yellow liquid (Figure 12(a)). After stirring until gel was formed, the solution turn into yellow slurry gel (Figure 12(b)). Then it was heated at 120^{o}C to remove the remaining solvent, gel changed to brown solid (Figure 12(c) and (d)). At calcination temperature higher than 500^{o}C, the brown solid changed to fine white particle (Figure 12(e) and (f)). But at temperature lower than 500^{o}C, the color of particle was black. The amount of Sm had effected to the appearance of catalyst, with higher amount of Sm, catalyst was more pale after calcination.

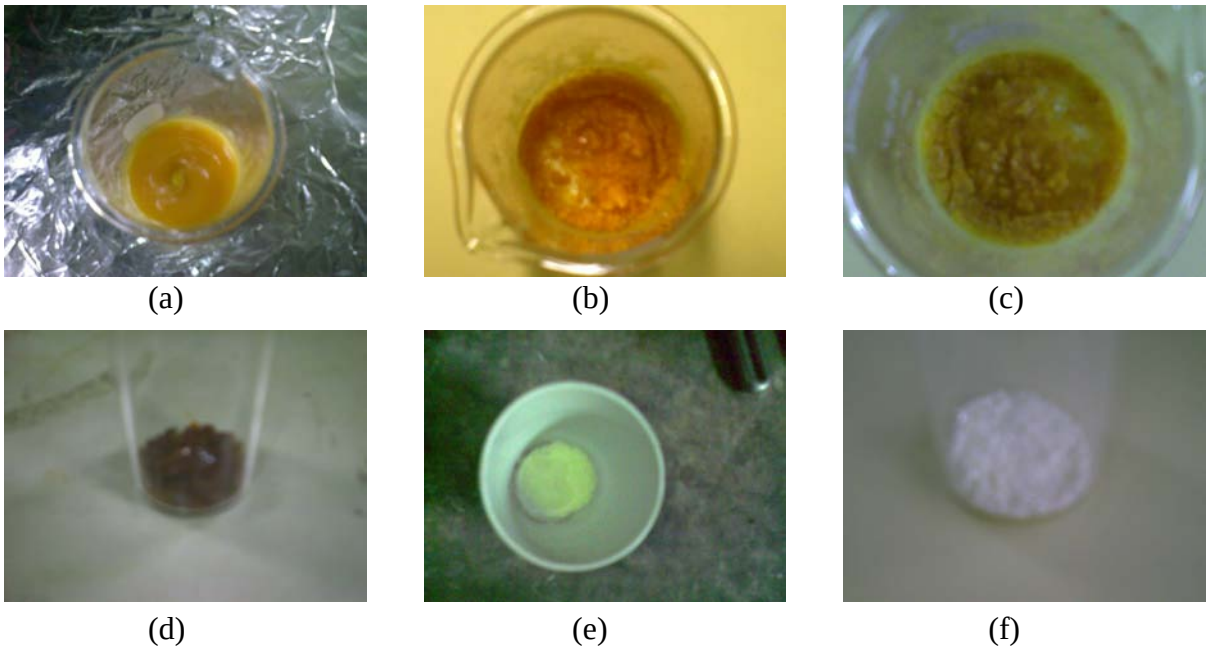

Figure 13 The changing of catalyst appearance in sol-gel process.
(a) mixture solution of all precursors
(b) after stirring until gel was form
(c) and (d) after heated at 120^{o}C to remove solvent
(e) and (f) after calcined at 500^{o}C

2. Catalyst characterization

2.1 X-ray powder diffraction spectroscopy (XRD)

The diffraction data of undoped TiO_2, Sm_2O_3, and Sm doped TiO_2 samples are shown in Figure 14, which were compared with XRD pattern of the standard anatase TiO_2 and standard Sm_2O_3.

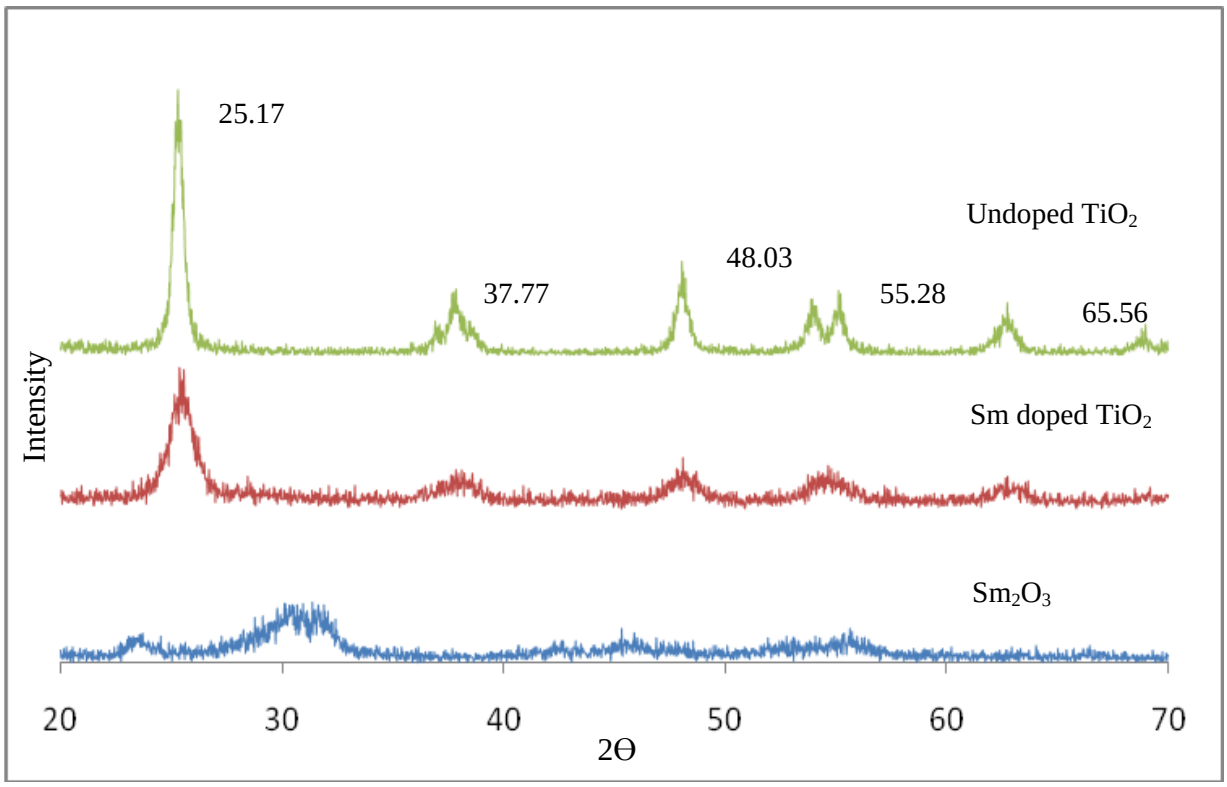

Figure 14 XRD patterns of (a) undoped TiO_2, (b) Sm doped TiO_2 and (c) Sm_2O_3.

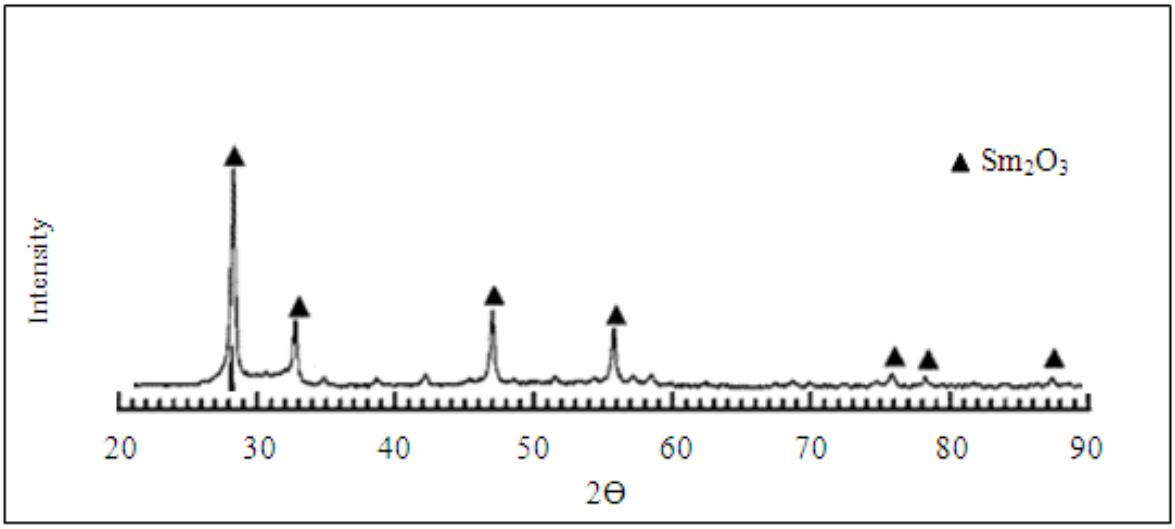

Figure 15 Reference XRD pattern of Sm_2O_3 heated at 400 °C.

Source: Liu *et al*. (2003)

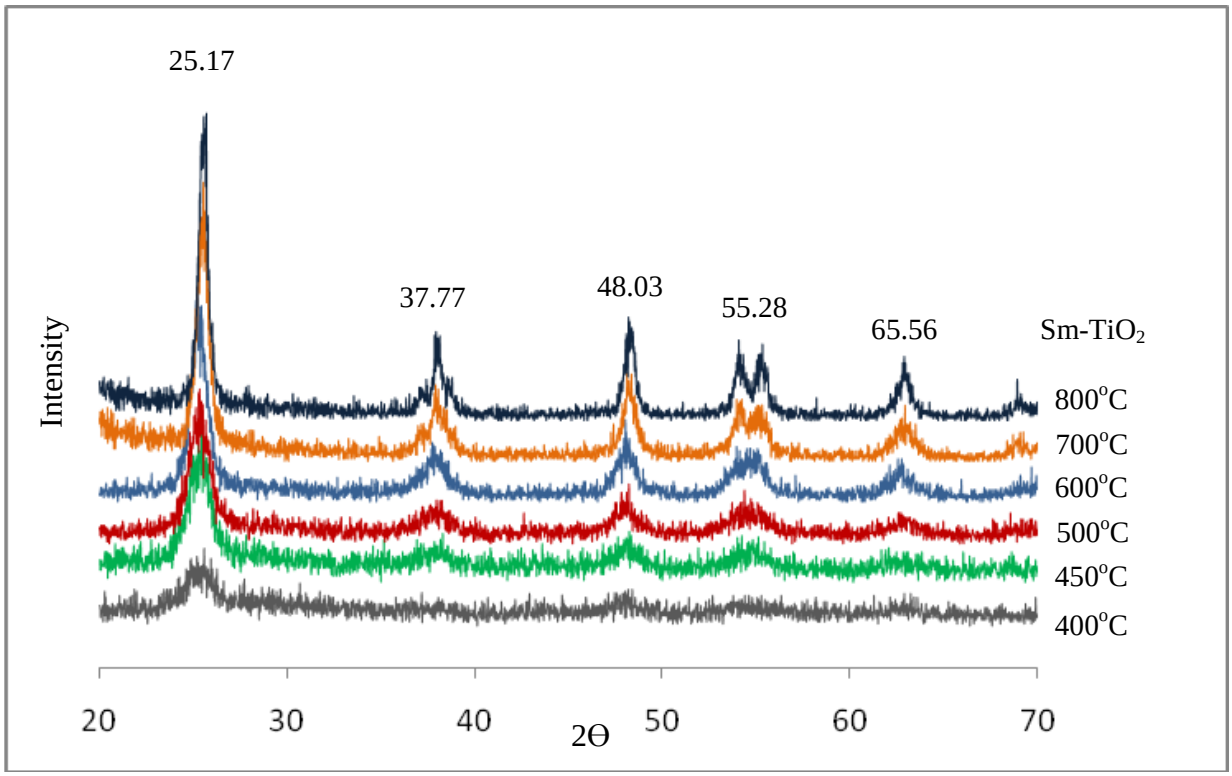

Figure 16 XRD patterns of 13.57 %wt Sm doped TiO_2 calcined at 400°C to 800°C.

Figure 14 (a) (b) and (c) showed the diffractogram of prepared undoped TiO_2, Sm doped TiO_2 and Sm_2O_3 respectively. The XRD peaks of undoped TiO_2 at 2Θ of 25.17^o, 37.77^o, 48.03^o, 55.28^o and 62.56^o indicated the presence of TiO_2 in anatase phase compared with standard diffractogram (Saif, 2004). Sm doped TiO_2 also showed the same peaks indicated that TiO_2 was also in anatase phase. Additionally, comparison between doped and undoped TiO_2, the relative intensity of major peak at 2Θ of 25.17^o of anatase phase decreased significantly in doped TiO_2, indicated that Sm doping inhibits the phase transformation from amorphous to anatase in solid structure, leading to higher thermal stability. The XRD pattern of prepared Sm_2O_3 was resemble to the reference diffractrogram of Sm_2O_3 as shown in Figure 15 with 2Θ peaks 32.8^o $47.2^o$and 55.9^o. The Sm_2O_3 peaks were not present in the prepared Sm doped TiO_2 catalyst which indicated that Sm-O bond was not occur in structure.

Figure 16 showed that the calcination temperature had effect on structure of the prepared catalyst. The catalysts which were calcined at temperature 400^oC – 800^oC were in anatase phase. The major peak was sharper as increasing calcination temperature, this meant the crystallinity of the catalyst was higher with the increasing calcination temperature. According to the previous study, phase transformation from anatase to rutile which decreased the activity of catalyst was occurred in undoped TiO_2 calcined at temperature higher than 500^oC. Sm doped TiO_2 gave different results, the diffractograms of Sm doped TiO_2 calcined at temperature higher than 500^oC gave the XRD pattern corresponding to pure anatase TiO_2. There were many reports study the effect of temperature on phase transformation. They found that at higher calcination temperature than 600^oC, the phase transform from anatase to rutile was occurred in undoped TiO_2 which decreased the photocatalytic activity of TiO_2. The results indicated that doping Sm ion could hinder the phase transformation to rutile in TiO_2 structure during calcinations.

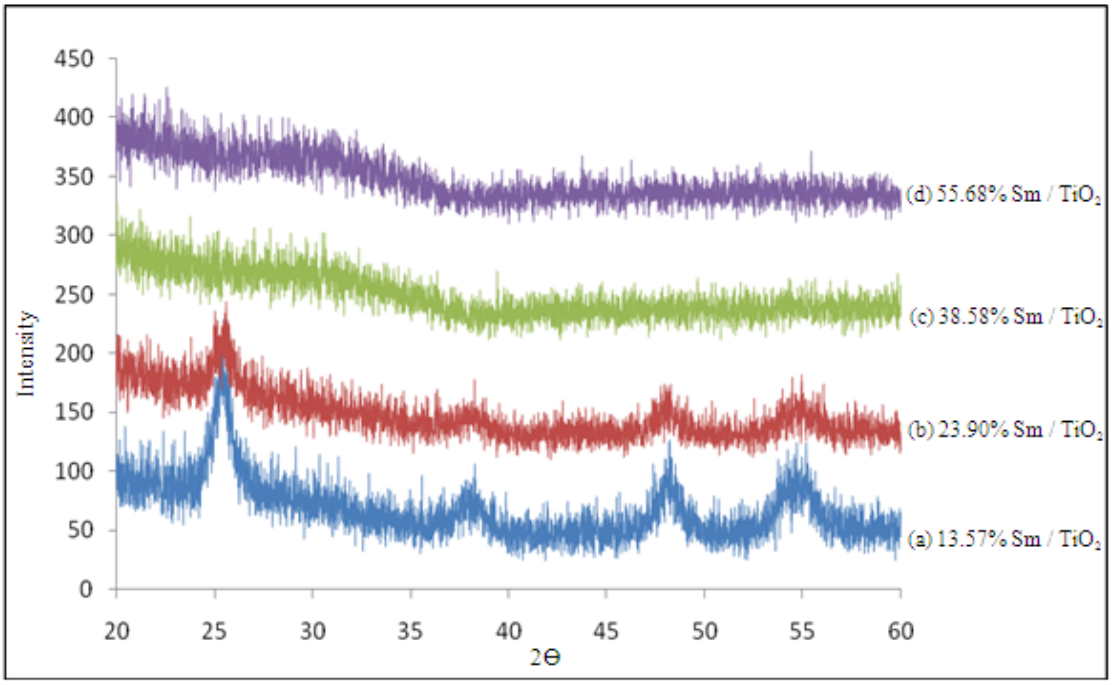

Figure 17 X-ray diffractogram of TiO_2 doped with various amount of %wt Sm loaded. (a) 13.57% Sm, (b) 23.90% Sm, (c) 38.58% Sm and (d) 55.68% Sm, all catalysts were calcined at 500^{o}C at the same preparing condition.

Figure 17 showed the XRD patterns of Sm doped TiO_2 with various amount of Sm loaded. The XRD results of 13.57% and 23.90% Sm doped showed that catalysts were in anatase phase. Higher amount of % Sm showed broad peaks of Samarium oxide (Sm_2O_3) indicated that these catalysts were amorphous and Sm species dispersed on their surface or the Sm_2O_3 was partially formed with increasing amount of Sm loaded which produced the combination of TiO_2 and Sm_2O_3 peaks presence in broad peak which occur at 2Θ of 32^{o}. As a consequence, exceeding amount of Sm doping could decrease catalyst activity.

Table 9 Crystal parameters data of undoped TiO_2 and Sm doped TiO_2 with various % loaded of Sm calcined at 400-800 ^oC for 2 hrs.

Catalyst	Calcination Temp (^oC)	%wt of Sm doped	$\%X_A$*	$\%X_R$*	Diffraction Angle 2Θ	Crystallite size * (nm)
P-25 TiO_2	-	0	74.90	25.10	25.43	22.60
TiO_2	500	0	98.30	1.70	25.31	16.34
TiO_2 + Sm	400	13.57	63.72	36.28	25.59	8.48
TiO_2 + Sm	450	13.57	74.84	25.16	25.99	8.51
TiO_2 + Sm	500	13.57	83.82	16.18	25.35	8.80
TiO_2 + Sm	600	13.57	86.71	13.29	25.19	10.46
TiO_2 + Sm	700	13.57	89.25	10.75	25.55	12.25
TiO_2 + Sm	800	13.57	89.92	10.08	25.57	14.70
TiO_2 + Sm	500	23.90	67.40	32.60	25.14	8.56

* The calculation of $\%X_A$,$\%X_R$ and crystallite size are shown in Appendix A and B respectively.

Table 9 showed that crystallite size of all prepared catalysts are smaller than commercial P-25 TiO_2 and also prepared Sm doped TiO_2 catalysts were smaller than undoped TiO_2. Table 9 also showed the ratio of anatase to rutile of the prepared catalysts which calculated by Liqiang's equation (Saif, 2007). Amount of Sm doped effected to crystallize size and ratio of anatase to rutile in catalyst structure. More amount of Sm doped gave smaller crystallize size and reduced in percentage of anatase. This indicated that Sm ion could hinder the increase of crystallize size during calcinations.

Additionally, calcination temperature also effected to crystallite size and ratio of anatase to rutile in catalyst structure. As increasing temperature, the crystallite size was slightly increased. The crystrallite size was in the range of 8 nm with calcination temperature at 400-500^oC. At higher temperature, the crystallite size was increased significantly and closed to undoped TiO_2 (16 nm). Percentage of anatase in Sm doped TiO_2 also increased with increasing calcination temperature which different from undoped TiO_2, the higher calcination temperature the lower % of anatase form.

As increasing calcination temperature from 400 to 500^oC, the percentage of anatase also increased obviously in range of 20%. At higher temperature (600 to 800^oC), the percentage of anatase was slightly increased from 83 to 89%.

From these experiments, it can conclude that the suitable temperature for calcinations should not lower than 500^oC and should not much higher than this temperature. Unless the crystallite size would be greater and phase transform to rutile would be occurred, which decrease the activity of catalyst, as a result. Amount of Sm also had effected on properties of catalyst. Amount of Sm loaded should not too high, to prevent Sm_2O_3 occured on surface of anatase TiO_2, which decreased the activity of catalyst, as a result.

Table 10 Unit cell parameters of P-25, undoped TiO_2 and 13.57 %wt Sm doped TiO_2 catalysts.

Catalyst	2Θ of anatase		d_{101}* (nm)	a (nm)*	c (nm)*	Volume* (nm^3)
P-25 TiO_2	25.43	37.87	0.3503	0.3767	0.9528	0.1352
Undoped TiO_2	25.31	37.87	0.3469	0.3724	0.9528	0.1321
13.57 %wt Sm doped TiO_2	25.45	37.87	0.3514	0.3781	0.9528	0.1363

* The calculation of unit cell parameters was shown in Appendix C.

Table 10 showed unit cell side (a and c) and unit cell volume of the prepared catalysts. The results showed that unit cell parameters of Sm doped TiO_2 were almost equal to undoped TiO_2 and also P-25. This indicates that unit cell structure of TiO_2 which is tetragonal structure is not changed via doping with Sm.

2.2 Thermogravimetric analysis (TGA)

Figure 18 and 19 showed % weight lost of uncalcined pure TiO_2 and Sm doped TiO_2 respectively. The similar results indicated that weight of both samples decreased by 50% lost, with heating temperature from 0 to 400 ^oC, in 2 steps due to the decomposition of solvent and water which maintain in gel sample after drying. The first weight loss at 100^oC assume to the decomposition of weakly adsorbed of organic solvent and water on catalyst surface. The second weight loss from 100 to 400 ^oC results from stronger adsorption of organic solvent which trapped on catalyst surface. At higher heating temperature, from 400 to 1000^oC, there was no change in weight lost upon undoped samples. In case of doping with Sm, there was slightly % weight lost occurred at 400 to 800 ^oC. This may due to the exist of more difficult and slower decomposition species which could be blocked by Sm^{3+} ion in TiO_2 structure. The removal of solvent and water from empty site occurred slower as a result. However, the boiling point of all precursors using in preparing step are lower than 400 ^oC. This meant that the sample can be calcined at 400^oC to higher temperature without changing in composition but the phase transform would possible occurred.

Figure 18 TGA diagram of uncalcined undoped TiO_2 (heating rate = 10^oC/min).

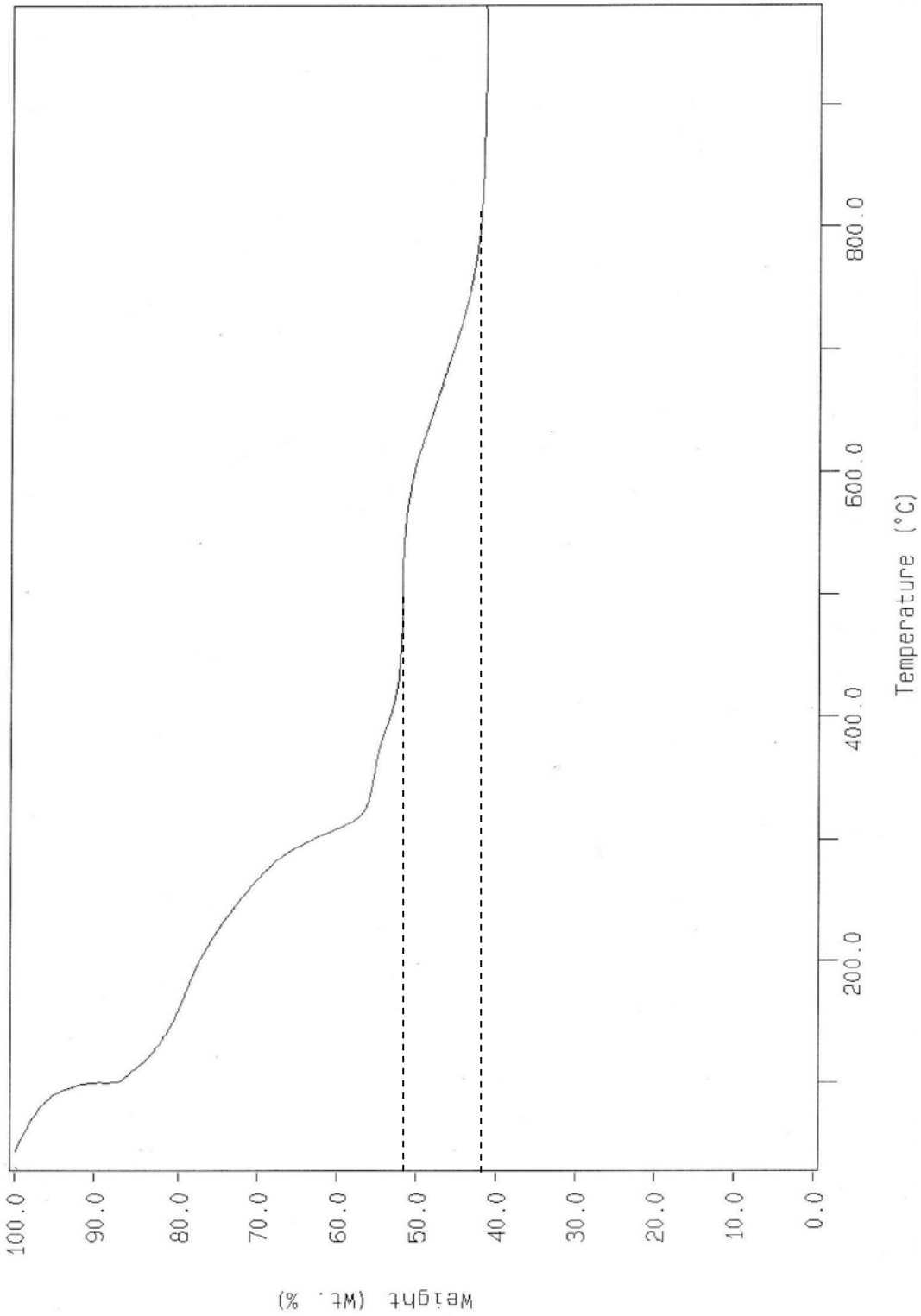

Figure 19 TGA diagrams of uncalcined 13.57 %wt Sm doped TiO_2 (heating rate = 10^oC/min).

2.3 Raman spectroscopy

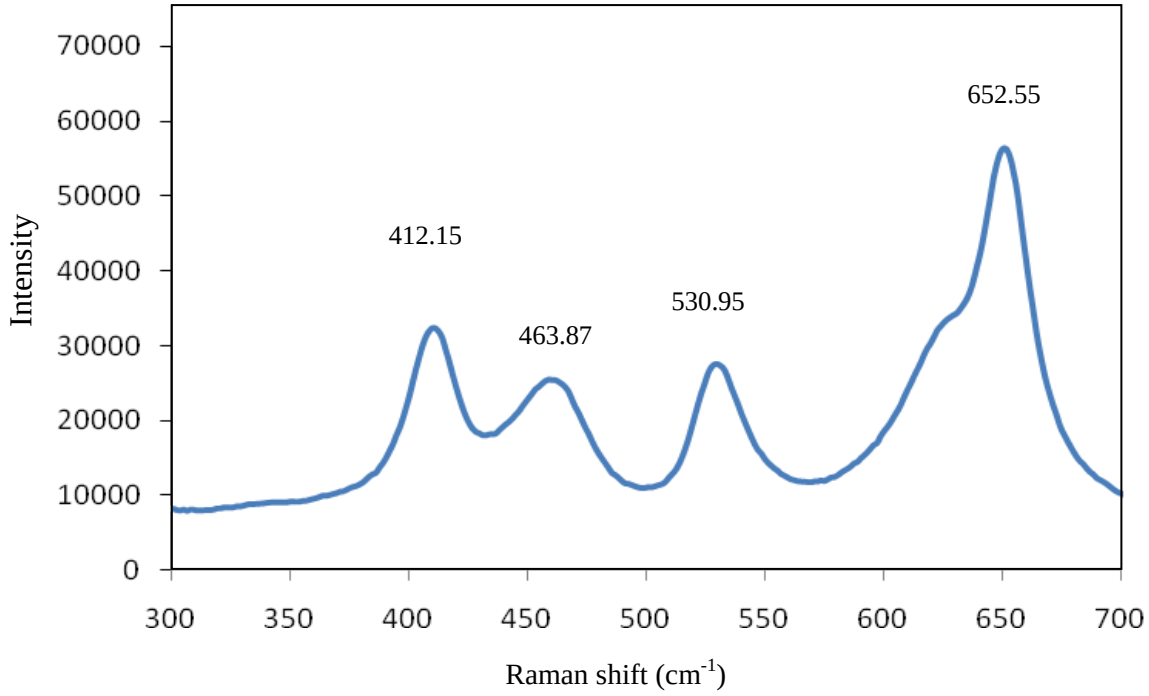

Figure 20 Raman spectrum of P-25 TiO_2.

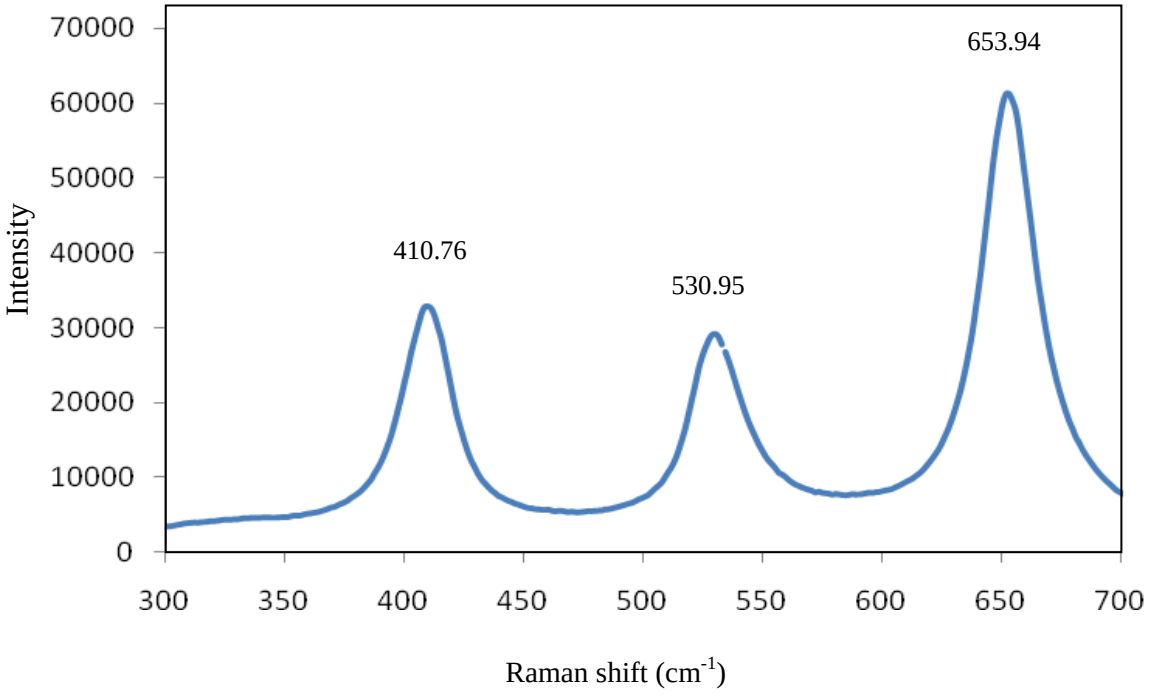

Figure 21 Raman spectrum of undoped TiO_2 calcined at 500^{o}C.

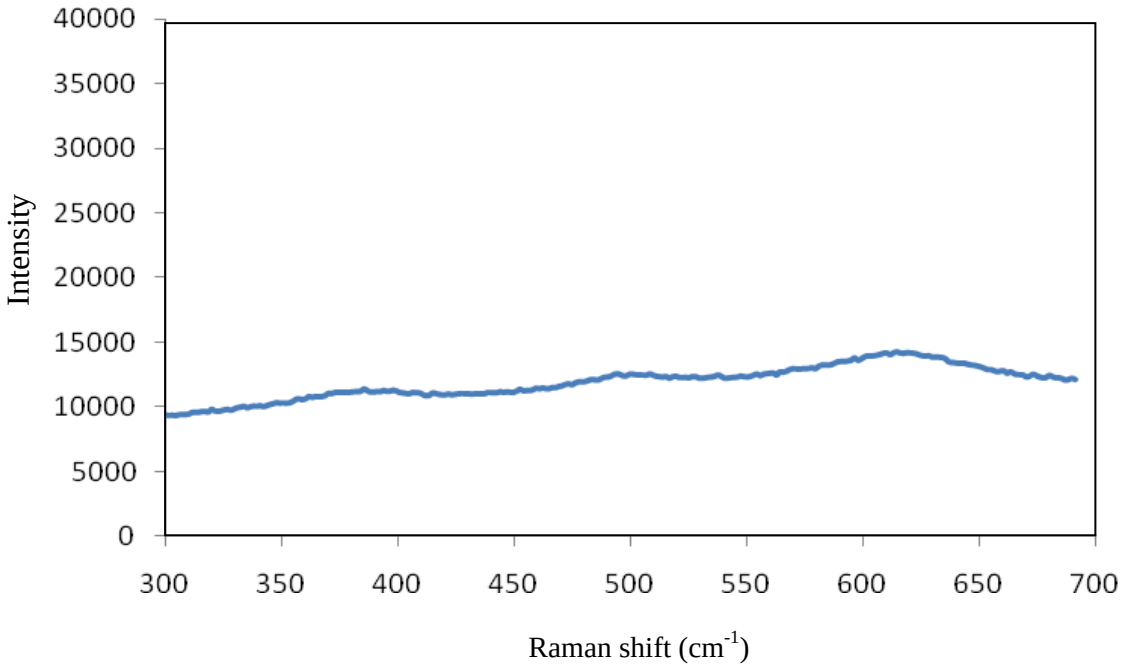

Figure 22 Raman spectrum of prepared 13.57 %wt Sm doped TiO_2 calcined at 400°C.

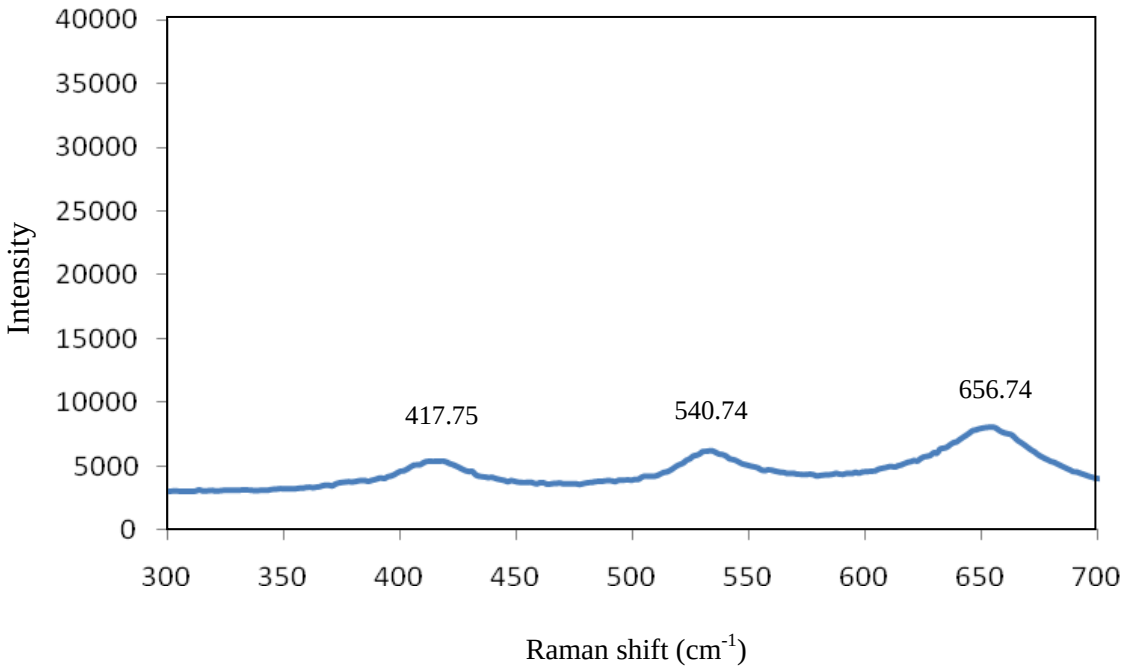

Figure 23 Raman spectrum of prepared 13.57 %wt Sm doped TiO_2 calcined at 450°C.

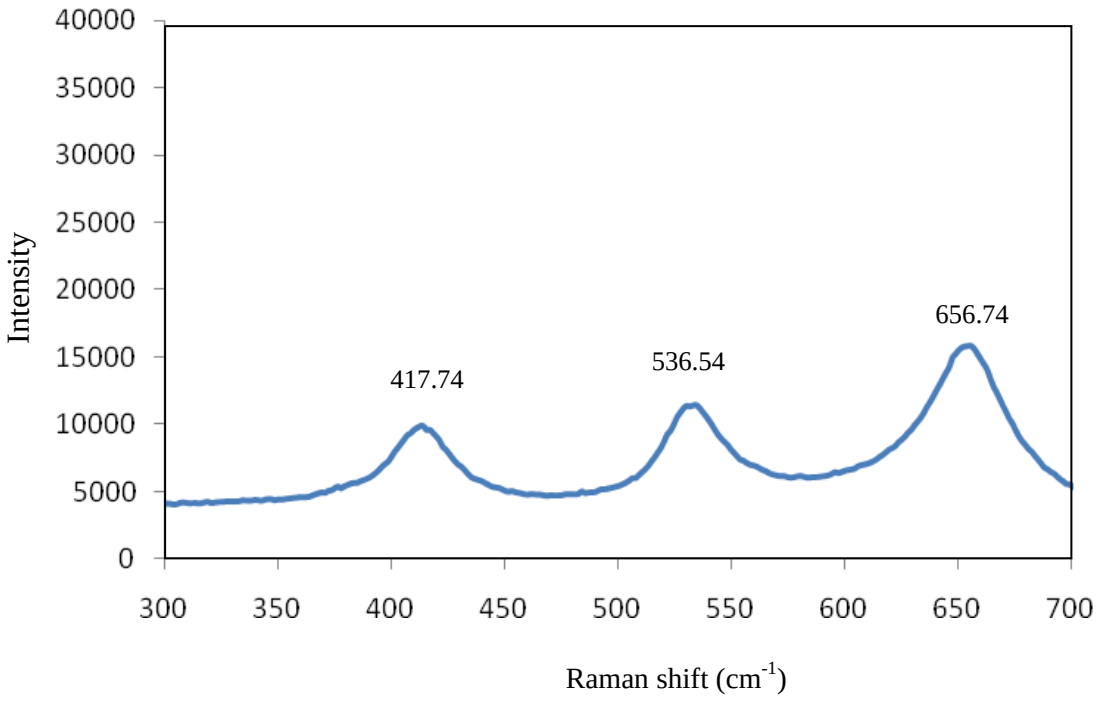

Figure 24 Raman spectrum of prepared 13.57 %wt Sm doped TiO_2 calcined at 500°C.

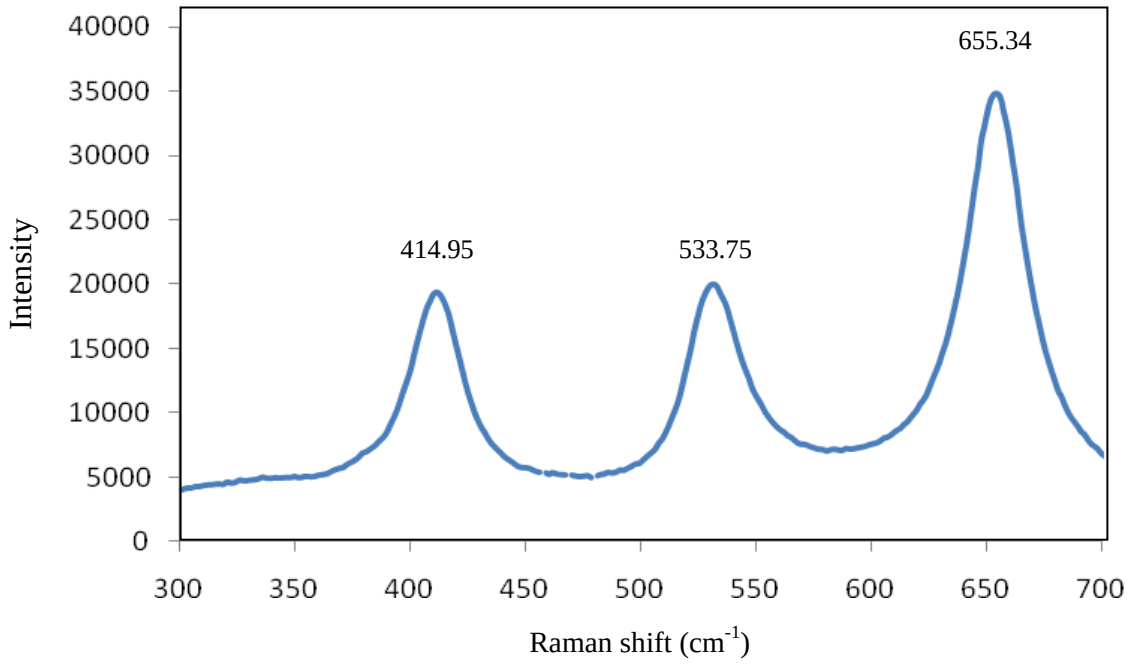

Figure 25 Raman spectrum of prepared 13.57 %wt Sm doped TiO_2 calcined at 600°C.

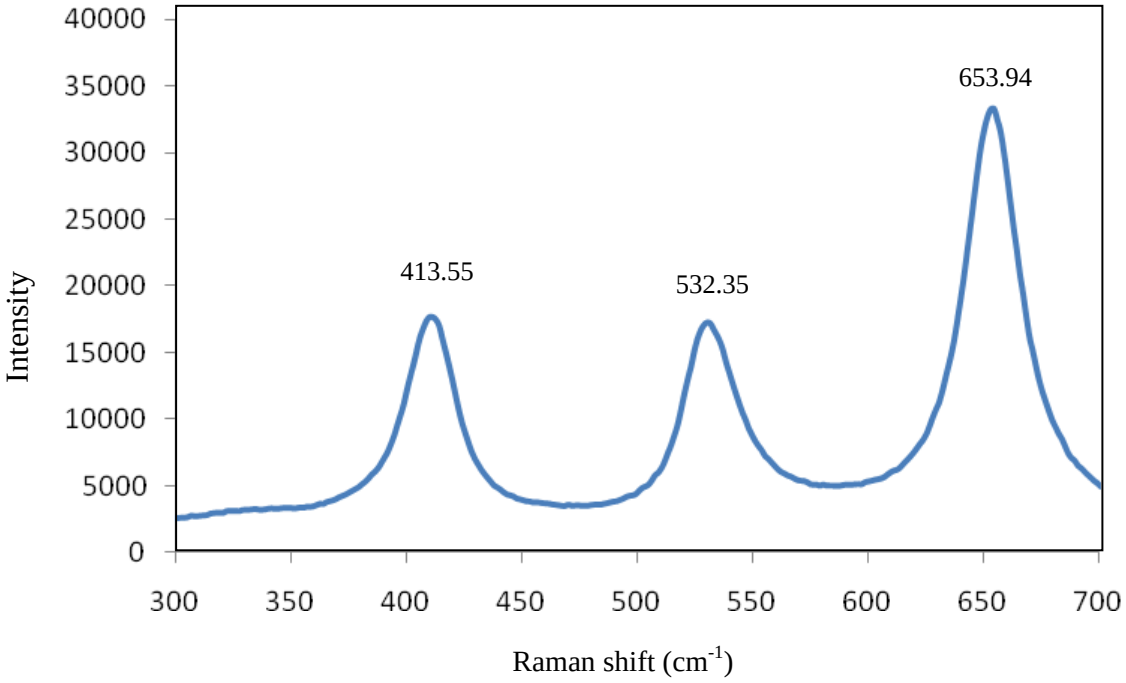

Figure 26 Raman spectrum of prepared 13.57 %wt Sm doped TiO_2 calcined at 700°C.

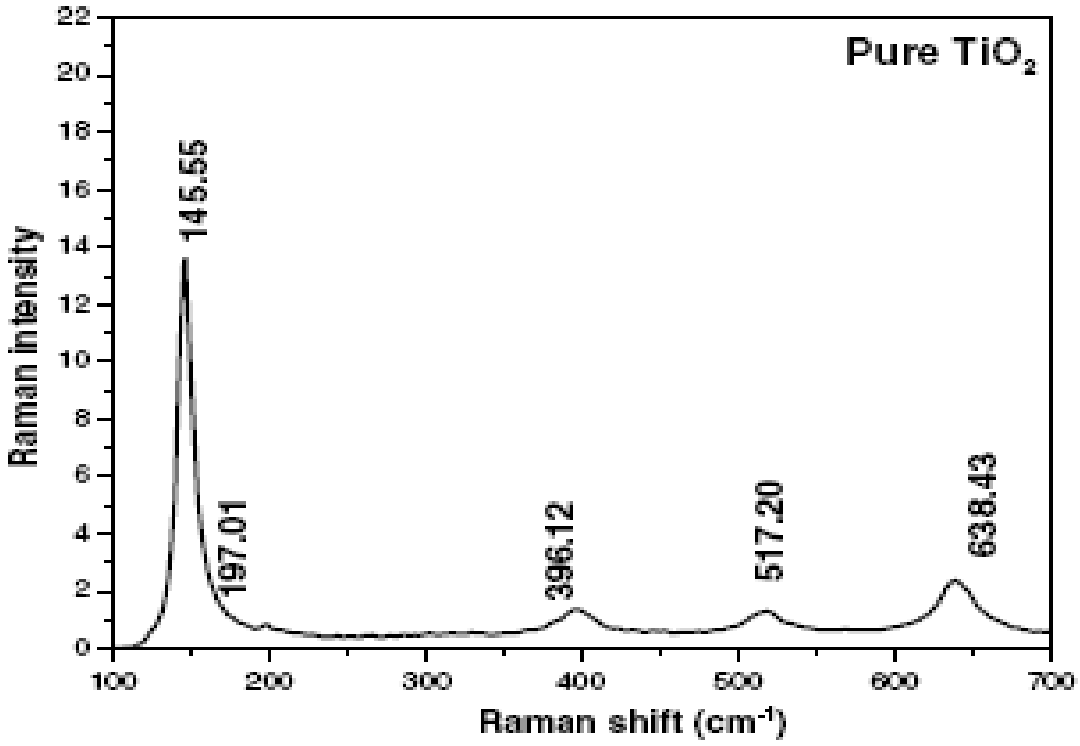

Figure 27 Reference Raman spectrum of undoped anatase TiO_2 calcined at 500°C.

Source: Saif (2007)

Table 11 Raman shift of Ti-O bond in 13.57 %wt Sm doped TiO_2, undoped TiO_2 and P-25 TiO_2.

Catalyst	Calcined temperature (^oC)	Raman shift (cm^{-1}) of Ti-O bond		
		1	2	3
Undoped TiO_2 Ref.	500	396.12	517.20	638.43
P-25 TiO_2	-	412.15	530.95	652.50
Undoped TiO_2	500	410.76	530.95	653.94
Sm doped TiO_2	400	broad	508.54	618.94
Sm doped TiO_2	450	417.75	540.74	656.74
Sm doped TiO_2	500	417.74	536.54	656.74
Sm doped TiO_2	600	414.95	533.75	655.34
Sm doped TiO_2	700	413.55	532.35	653.94

Figure 20 showed the Raman spectrum of P-25 TiO_2 which consisted of 4 characteristic peaks. Three peaks at 412.15, 530.95 and 652.50 cm^{-1} were characteristic peaks of anatase TiO_2 and one peak at 463.87 cm^{-1} and the shoulder peak at 620 cm^{-1} were assigned to rutile phase.

Figure 21 showed the Raman spectrum of undoped anatase TiO_2, characteristic peak at 410.76, 530.95 and 653.94 cm^{-1} which could be assigned to the anatase phase compare to reference Raman spectrum (396.12, 517.20 and 638.43 cm^{-1}) as shown in Figure 26 (Saif, 2007). The spectrum of 13.57% Sm doped TiO_2 which calcined at 400 ^oC (Figure 22) and 450^oC (Figure 23) gave the broad spectrum, indicated that there were less of Ti-O bonds forming and catalyst could be amorphous solid. However, the spectra of Sm doped TiO_2 which calcined at 500 ^oC up to 700 ^oC (Figure 24 to 26) were similar to undoped anatase TiO_2 but slightly shifted to lower frequency and energy as a result of crystal structure modification via doping (Saif, 2007). Additionally, this may suggested the incorporation of Sm into the TiO_2 structure and should be in anatase hole which increased the contraction of Ti-O

bond. Because there were characteristic peaks that fit to reference spectrum of TiO_2 (410.76, 530.95 cm^{-1}) and the slightly shifted on the anatase Ti-O peaks to higher frequency (417.74, 536.54 cm^{-1}) indicated that the Ti-O bond was shorter and stronger due to bond contraction via doping Sm. However, there was no Sm-O peak presence in these spectra. This maybe because the size of Sm atom was much larger than Ti atom, therefore Sm could not substitute the Ti atom and form bond with O atom in TiO_2. Due to these reason, Sm should incorporated into the interstitial site of the TiO_2 catalyst.

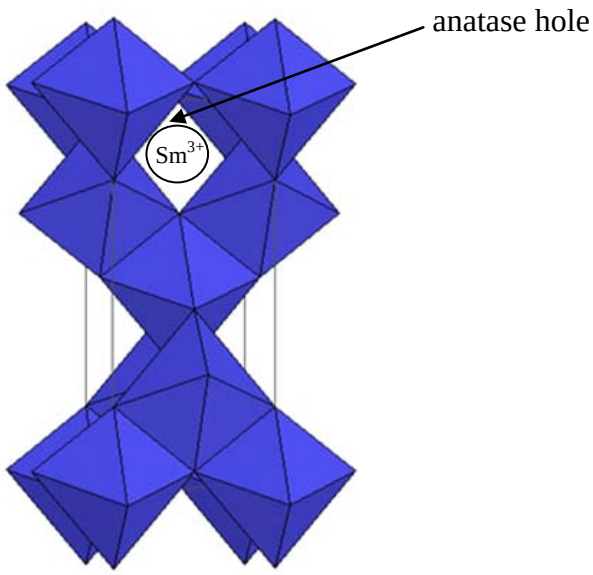

Figure 28 The proposed structure of TiO_2 which Sm^{3+} incorporated into anatase hole.

The proposed structure of the incorporation of Sm^{3+} into anatase hole of TiO_2 is shown in Figure 28. The position of Sm(III) should be in the vacant site of axial Ti-O bond. The larger Sm ion caused Ti-O bond contracted resulting in shorter and stronger bond and hence Raman shifted to higher frequency.

2.4 UV-Vis reflectance spetra

Figure 29 showed the UV-Vis reflectance spectra of TiO_2 and Sm doped TiO_2 in range of 200-800 nm. It can be seen that TiO_2 had no absorption in visible range (> 400 nm). But Sm doped TiO_2 which calcined at 450, 500 and 600 ^oC had significant absorption between 400 to 600 nm. The optical absorption in the visible region was enhanced due to doping of Sm. This may concern with the band gap of TiO_2 which was reduced by Sm doping, which introduced electron into the band gap of TiO_2 to formed the new higher lowest unoccupied molecular orbital (LUMO). Figure 30 also showed that the absorption of visible light range was slightly increased as increasing of %Sm loaded.

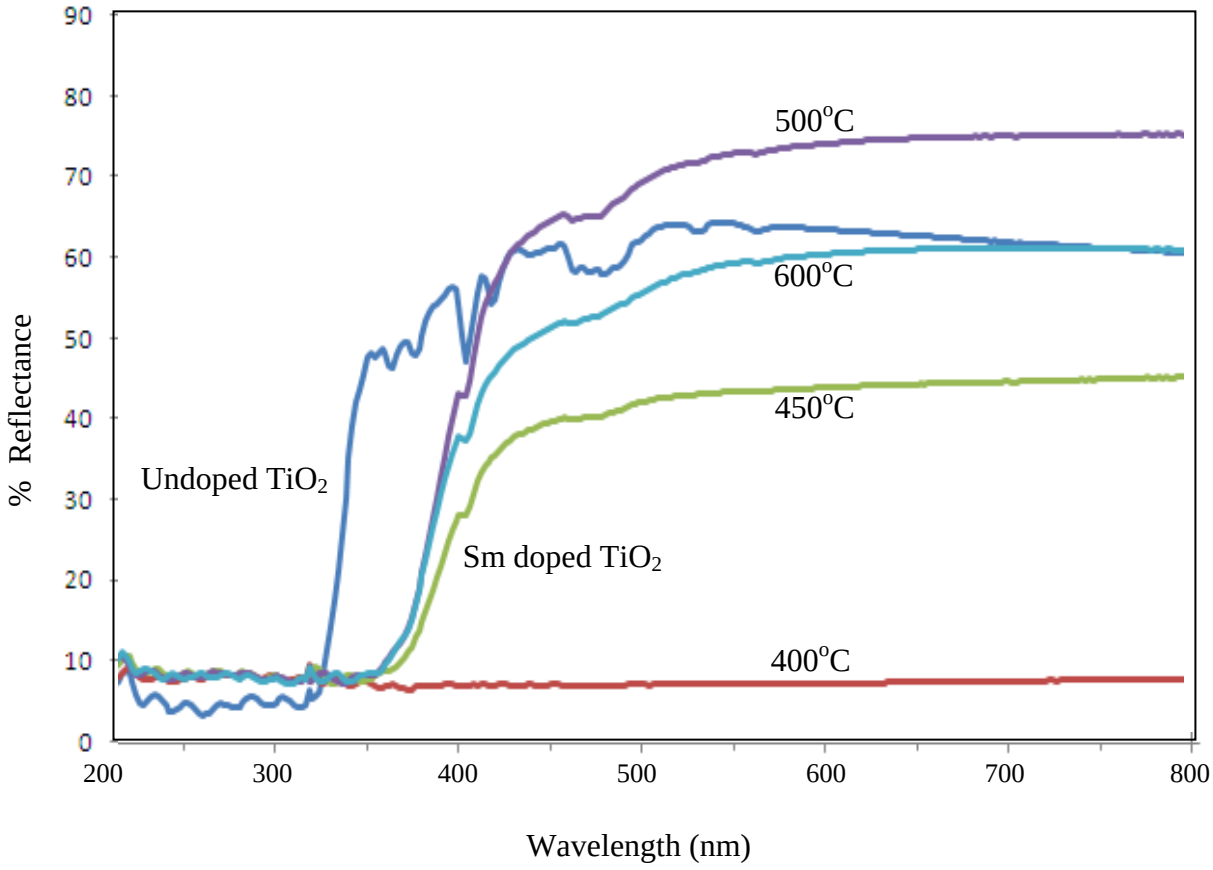

Figure 29 UV-Vis reflectance spectra of undoped TiO_2 and 13.57% Sm doped TiO_2 calcined at various temperatures (400 -600^oC).

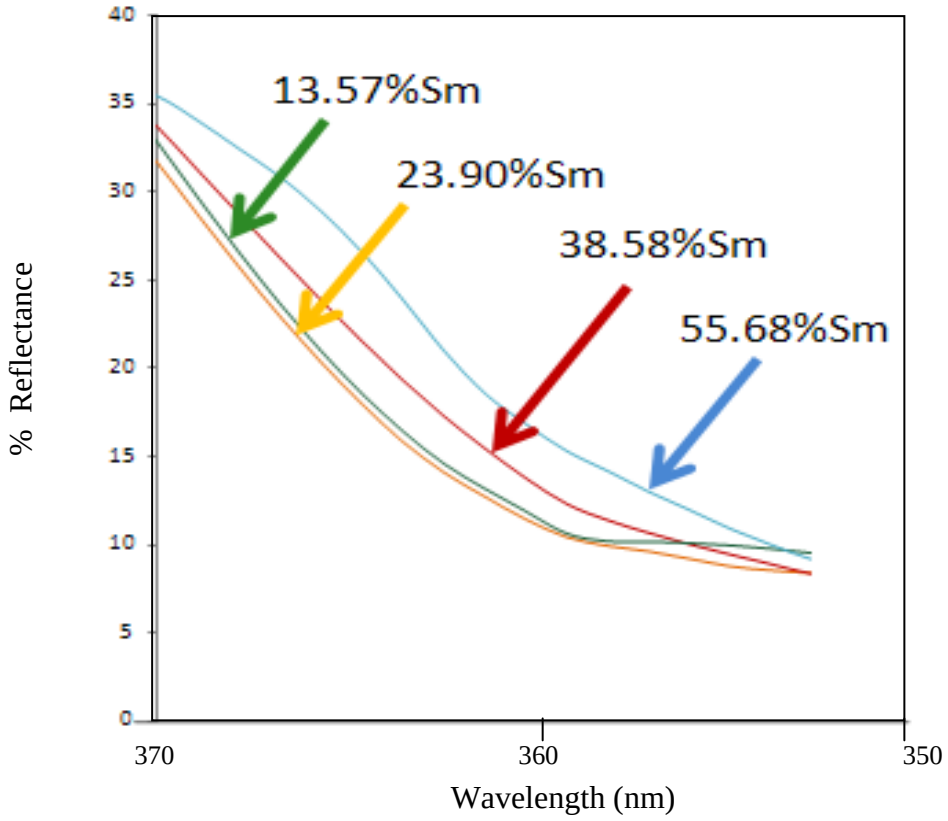

Figure 30 UV-Vis reflectance spectra of TiO_2 doped with various amount of Sm at wavelength of 350-370 nm.

Figure 30 showed the effect of the amount of Sm doping on catalysts. The result showed that Sm doping can extend the photoresponse of TiO_2 in visible light region. However, the adsorption edge was slightly shifted to shorter wavelength when increase amount of Sm doping. As a consequence, it could improve the catalytic activity of TiO_2 for photodegradation of PAHs compounds under visible light.

Additionally, the energy gap can be calculated from absorption edges which resulted from UV-Vis reflectance spectra. The energy gap can be calculated by the equation as follows (Sirisaksoontorn *et al*., 2009);

$$E_g = \frac{1239.8}{\lambda}$$

where E_g is band gap energy (eV)

λ is wavelength (nm)

Table 12 The calculated band gap energy of undoped TiO_2 and Sm doped TiO_2.

Catalyst	Absorption edge λ (nm)	E_g* (eV)
Undoped TiO_2	362	3.42
13.57 %wt Sm doped TiO_2	412	3.01
23.90 %wt Sm doped TiO_2	407	3.05
38.58 %wt Sm doped TiO_2	403	3.08
55.68 %wt Sm doped TiO_2	401	3.09

* Calculation of absorption edge and energy gap was showed in Appendix D.

The calculation of E_g in table 12 indicated that Sm doping could decrease band gap energy of TiO_2 from 3.42 to 3.01-3.09 eV which improved the photoresponse of TiO_2 to visible light region. And the catalytic activity in oxidation reaction would also increased. However, the adsorption edge was slightly shifted to shorter wavelength when increase amount of Sm doping then band gap was slightly increased. This due to Sm species which dispersed on TiO_2 surface occurred with higher amount of Sm doping. As a consequence, band gap was increase.

2.5 Scanning electron microscope and Energy Dispersive X-ray Spectroscopy (SEM/EDX)

To study surface structure of the prepared catalysts, SEM was used. Figure 31 to 39 showed the SEM images of each catalysts at different magnification (200 and 2500X). Figure 31 and 32 are the SEM images of undoped TiO_2. Figure 33 to 40 showed the SEM images of TiO_2 doped with 13.57%, 23.90%, 38.58% and 55.68 % wt of Sm respectively. The results showed that, the size of catalysts was in nanometer range which related to XRD data. The estimate size of undoped TiO_2 was larger than Sm doped TiO_2. Also the TiO_2 particles which doped with higher amount

of Sm had smaller size compared with lower amount of Sm. It can concluded that Sm doping had effect on size of TiO_2 by decrease the size of TiO_2 particle.

The crystal structure of prepared the TiO_2 from SEM images was found to be closed to the tetragonal lattice but almost condensed due to the calcination at high temperature.

Figure 41 and 42 showed reference SEM images of TiO_2 particle at 1000X and 10000X magnification. The structure of prepared TiO_2 catalysts were similar to the reference TiO_2. Also the structure of Sm doped TiO_2 catalysts were not different compared with undoped TiO_2.

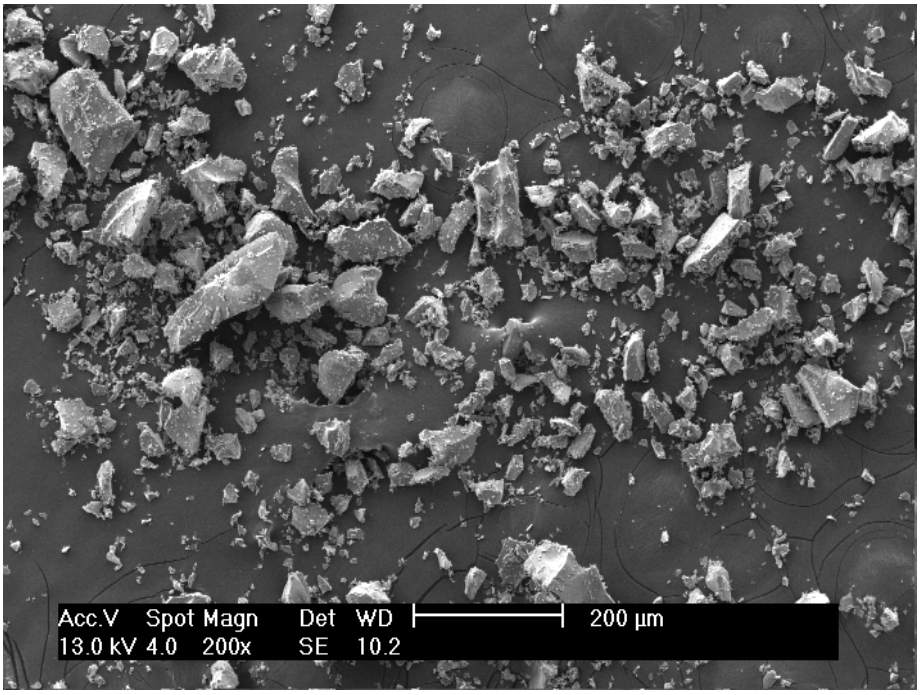

Figure 31 SEM image of undoped TiO_2 calcined at 500^{o}C at 200x magnification.

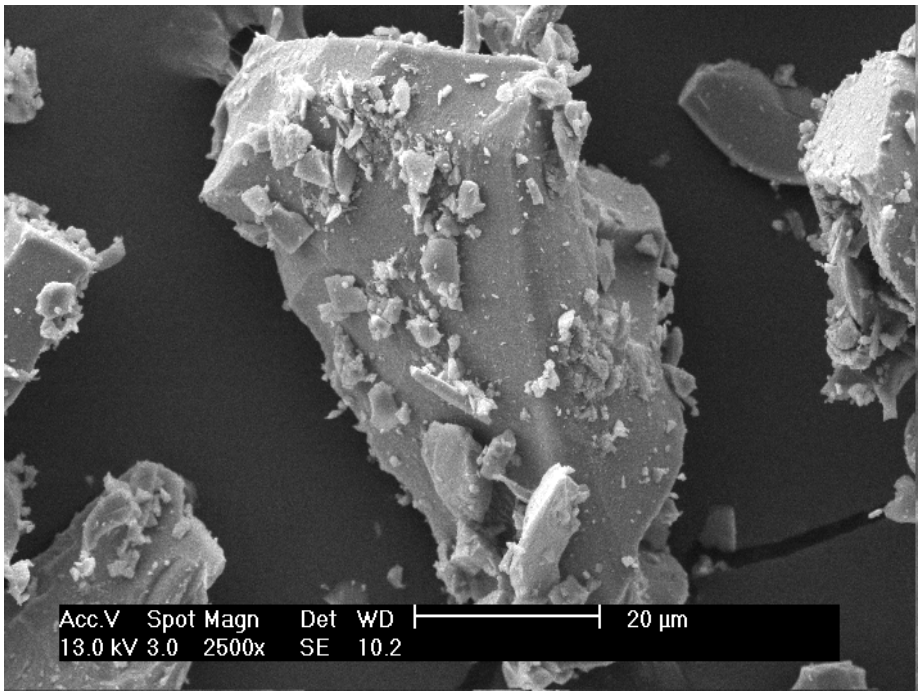

Figure 32 SEM image of undoped TiO_2 calcined at 500^{o}C at 2500x magnification.

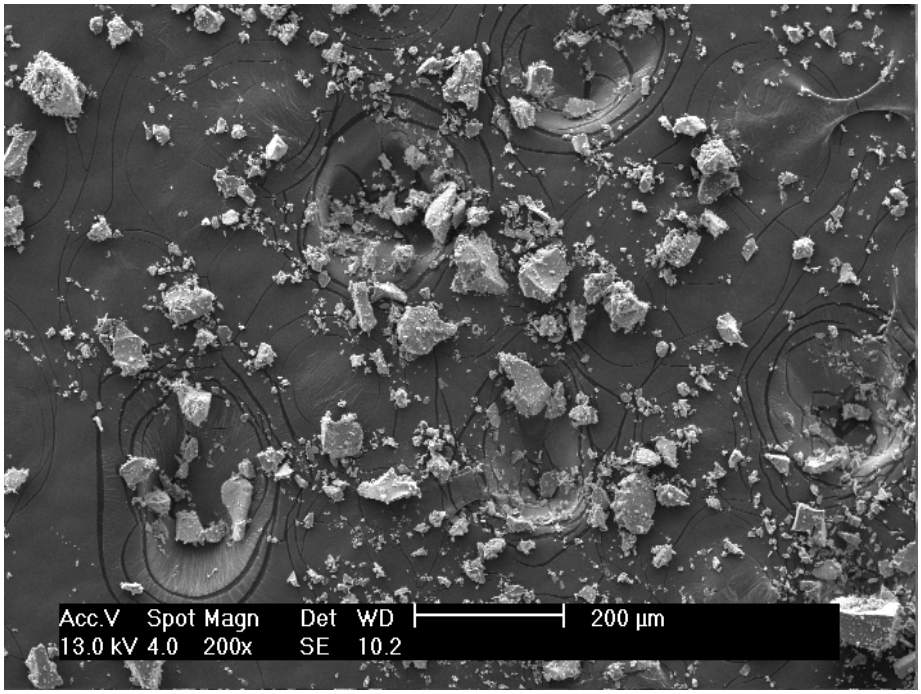

Figure 33 SEM image of 13.57 %wt Sm doped TiO_2 calcined at 500^{o}C at 200x magnification.

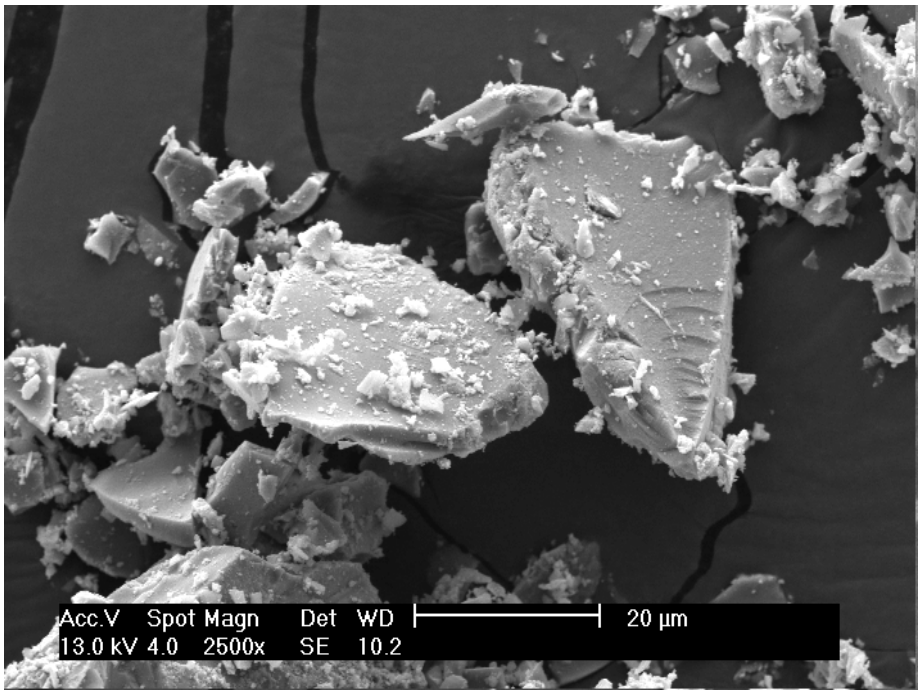

Figure 34 SEM image of 13.57 %wt Sm doped TiO_2 calcined at 500^{o}C at 2500x magnification.

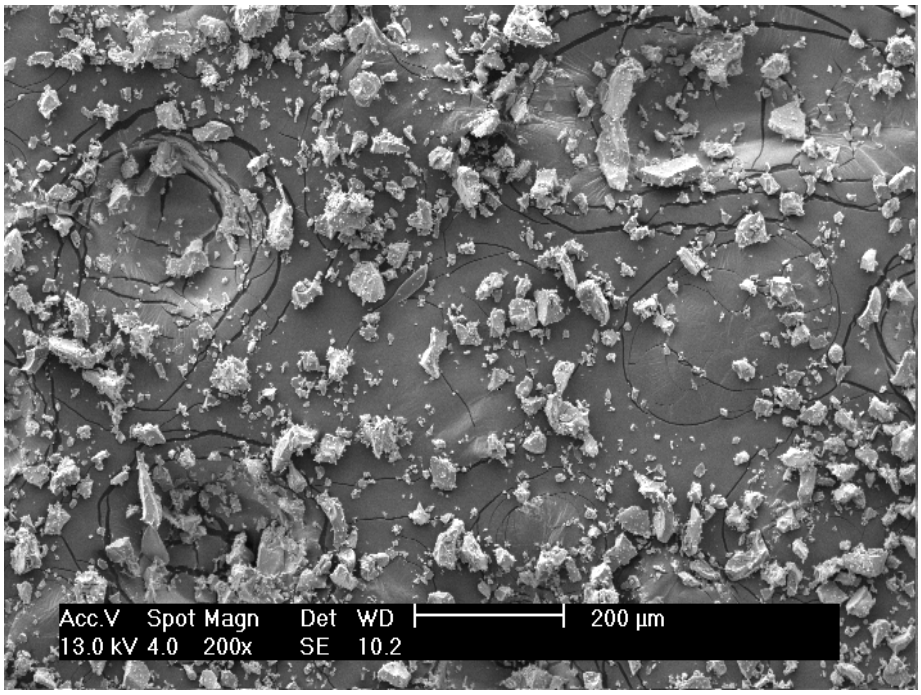

Figure 35 SEM image of 23.90 %wt Sm doped TiO_2 calcined at 500^{o}C at 200x magnification.

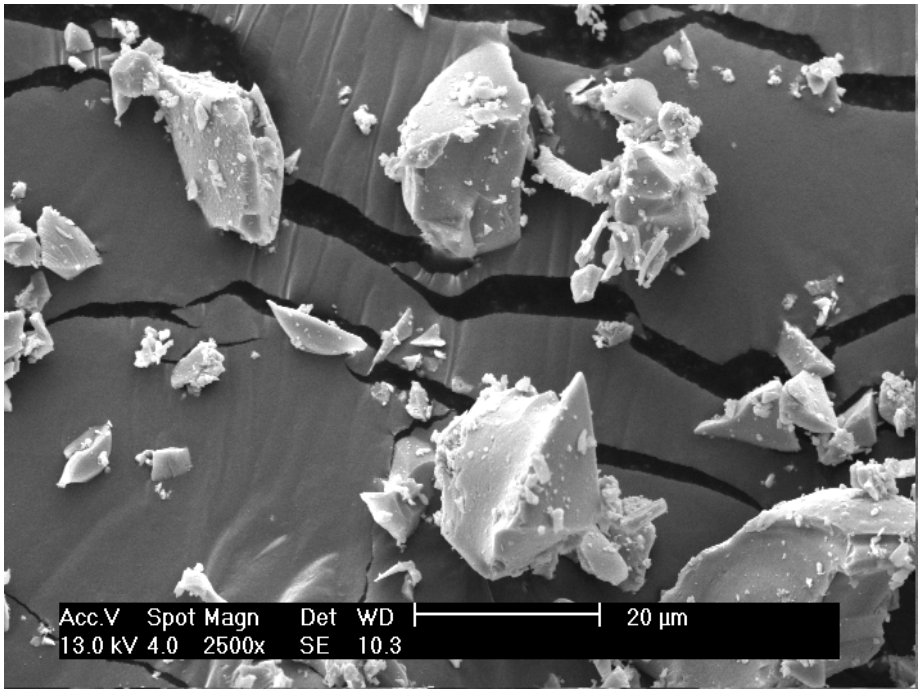

Figure 36 SEM image of 23.90 %wt Sm doped TiO_2 calcined at 500^{o}C at 2500x magnification.

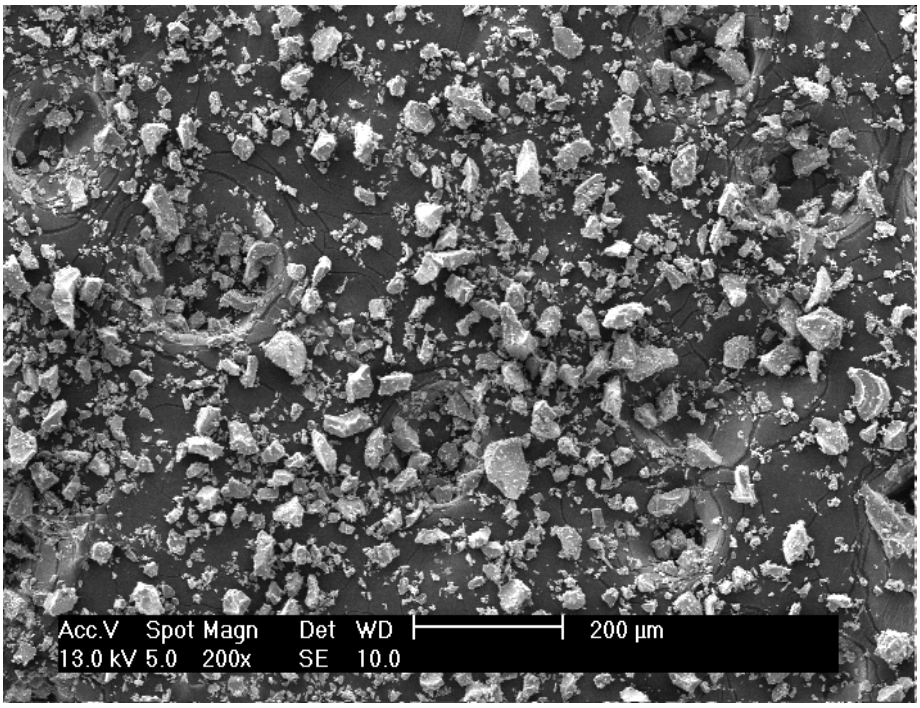

Figure 37 SEM image of 38.58 %wt Sm doped TiO_2 calcined at 500^{o}C at 200x magnification.

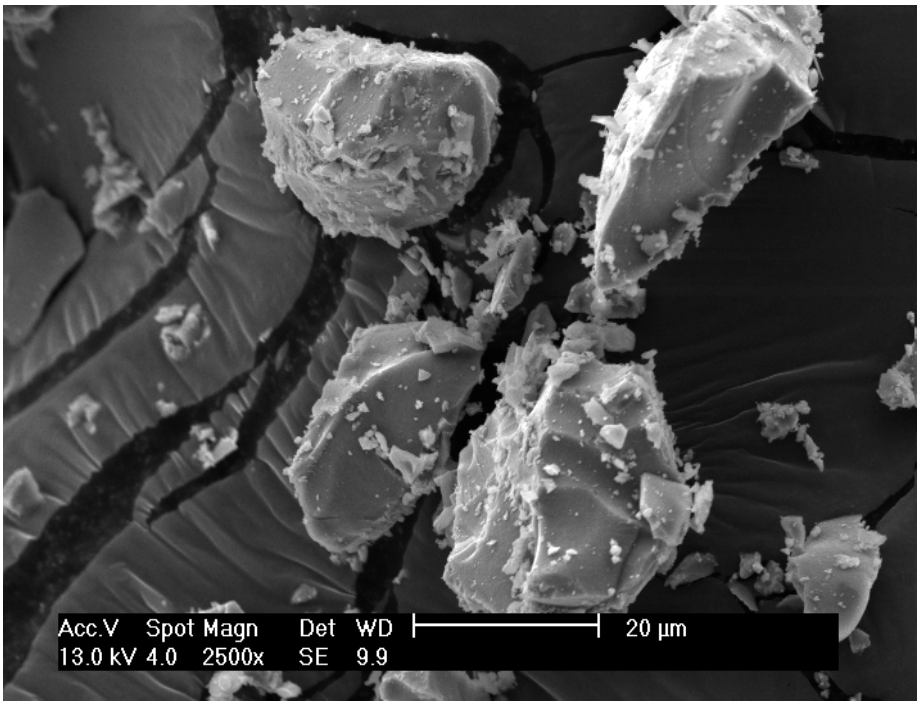

Figure 38 SEM image of 38.58 %wt Sm doped TiO_2 calcined at 500^{o}C at 2500x magnification.

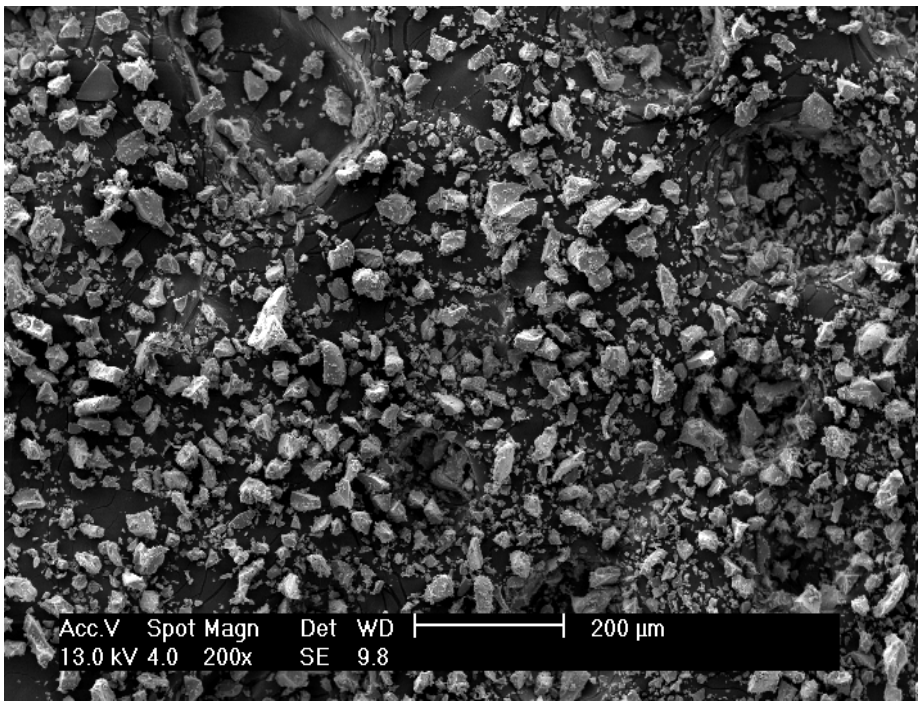

Figure 39 SEM image of 55.68 %wt Sm doped TiO_2 calcined at 500^{o}C at 200x magnification.

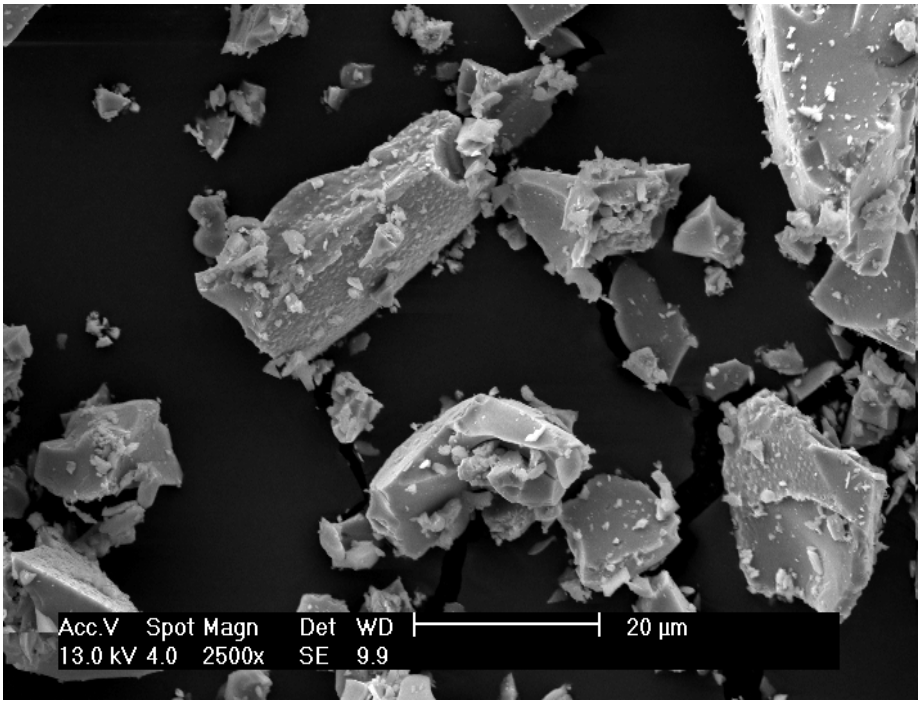

Figure 40 SEM image of 55.68 %wt Sm doped TiO_2 calcined at 500^{o}C at 2500x magnification.

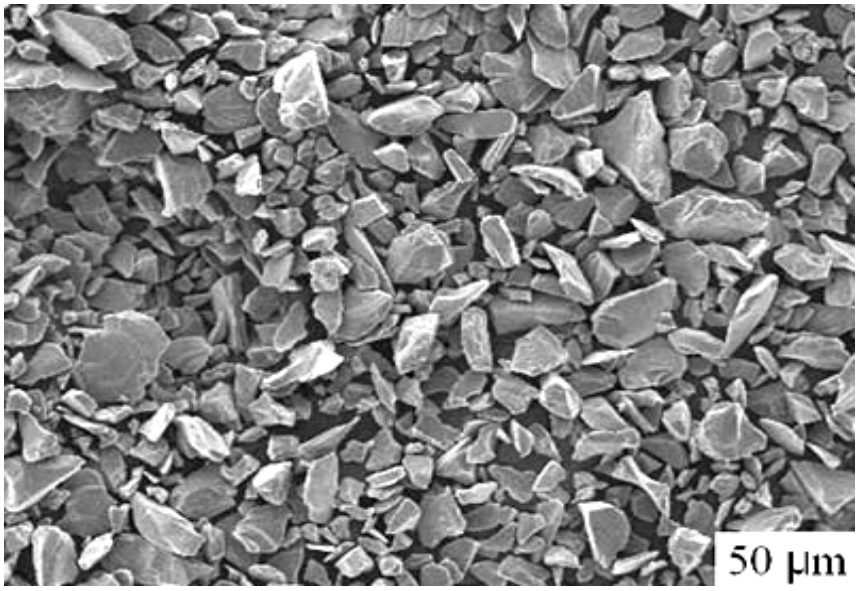

Figure 41 Reference SEM image of TiO_2 at 1000X magnification.

Source: Du (2004)

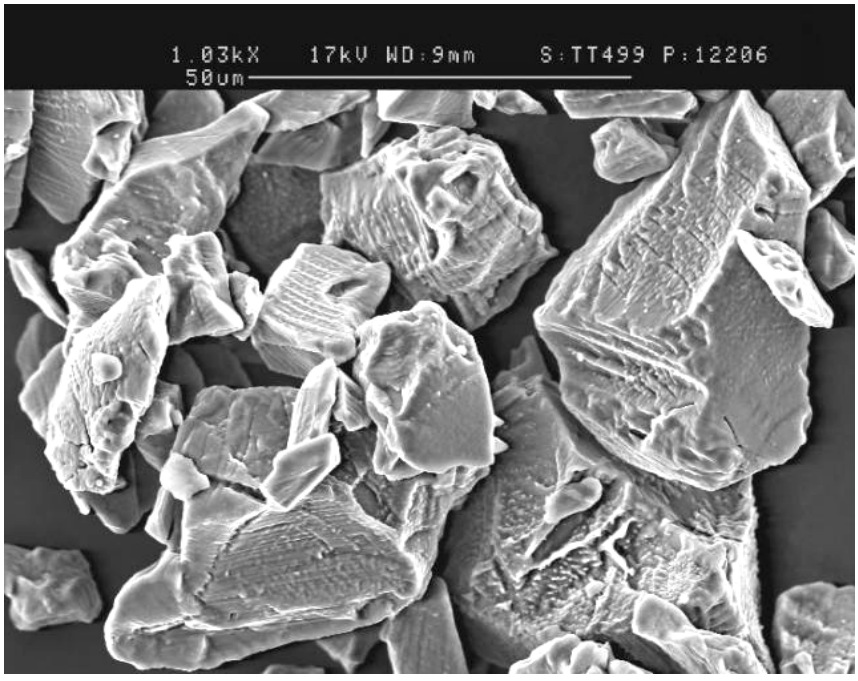

Figure 42 Reference SEM image of TiO_2 at 10000X magnification.

Source: Instituto de Ciencia de Materiales de Madrid (2008)

The estimate amount of element composition in sample was determined by SEM/EDX technique. EDX spectra of undoped TiO_2 and Sm doped TiO_2 with various amount of Sm are shown in Figure 43 to 47. Four major peaks at 0.6, 2.2, 4.5 and 5.7 keV were the characteristic energy of O, Au, Ti and Sm respectively. There were only three peaks of O, Au and Ti in undoped TiO_2. Au peak raised from the Au coating via analysis to improve conductivity of TiO_2. The intensity of Sm peak which appeared only in Sm doped TiO_2 related to amout of Sm in sample.

The EDX data which can be used to determine the amount of Sm doping on TiO_2 was shown in Table 13. However, the % weight of composition data from EDX was only estimate value. It depended on the position of surface on sample , which the Sm composition may or may not homogineity dispersed . However, the average % weight of Sm (n=3) calculated from EDX is almost equivalent to % loading of Sm via preparation. Therefore, almost all of Sm doping on TiO_2 should possessed in the TiO_2 structure. Although TiO_2 was calcined at high temperature, the decomposition of Sm would not occur due to the high melting point and boiling point of Sm which much higher than calcination temperature.

Table 13 The percentage of Sm in undoped TiO_2 and Sm doped TiO_2 catalysts determined by SEM/EDX.

Catalyst	% wt of Sm on doping	%wt of Sm from EDX *
Undoped TiO_2	0	0
Sm doped TiO_2	13.57	13.63 $\pm$ 1.41
Sm doped TiO_2	23.90	28.31 $\pm$ 3.18
Sm doped TiO_2	38.58	35.50 $\pm$ 1.44
Sm doped TiO_2	55.68	50.69 $\pm$ 0.23

* Full data of %wt of Sm from EDX was shown in Appendix E

Figure 43 to 46 showed EDX spectra which indicated only Ti and Sm peaks. Figure 47 showed all peaks which appeared in EDX spectrum, each characteristic peak indicated the exist of each element such as Ti, O, Sm and also Au which used to coat on TiO_2 sample to improve conductivity.

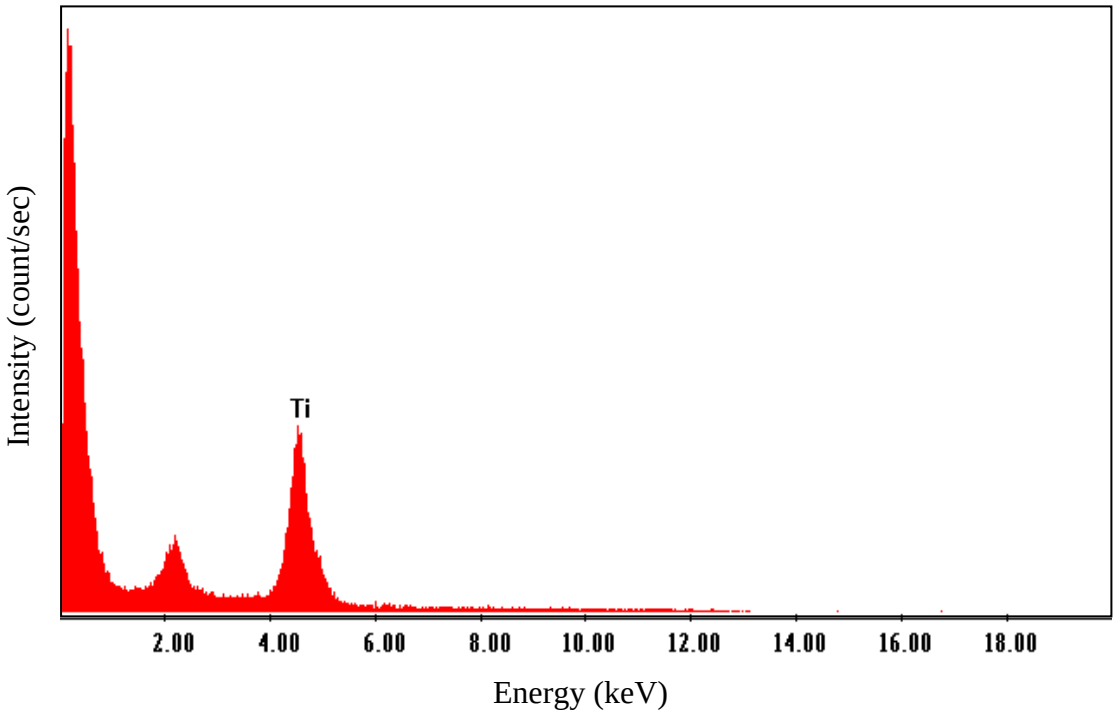

Figure 43 EDX spectrum shows the semiquantification of each elements composition in undoped TiO_2 catalyst calcined at 500^{o}C.

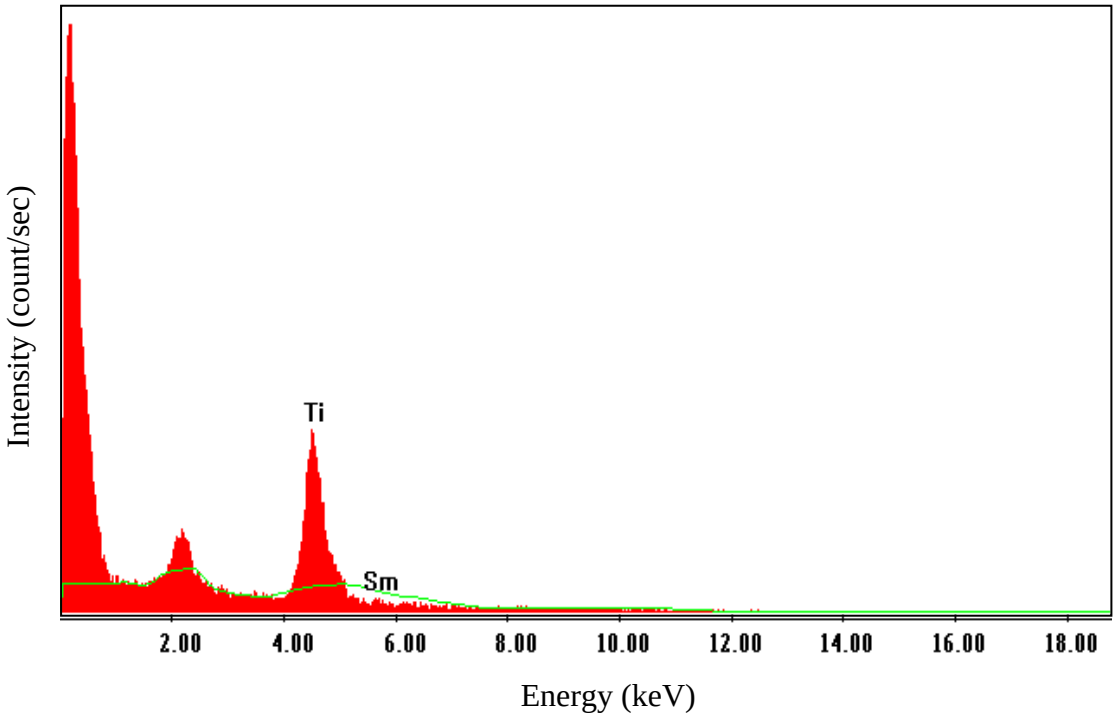

Figure 44 EDX spectrum shows the semiquantification of each elements composition in 13.57 %wt Sm doped TiO_2 catalyst calcined at 500^{o}C.

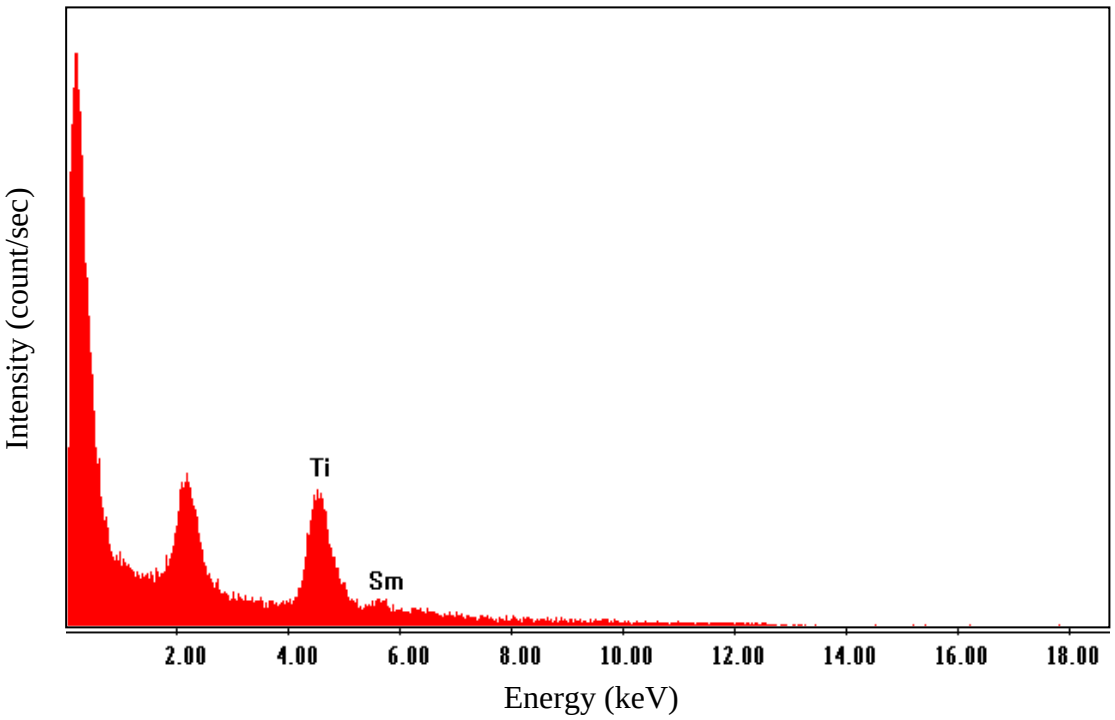

Figure 45 EDX spectrum shows the semiquantification of each elements composition in 23.90 %wt Sm doped TiO_2 catalyst calcined at 500^{o}C.

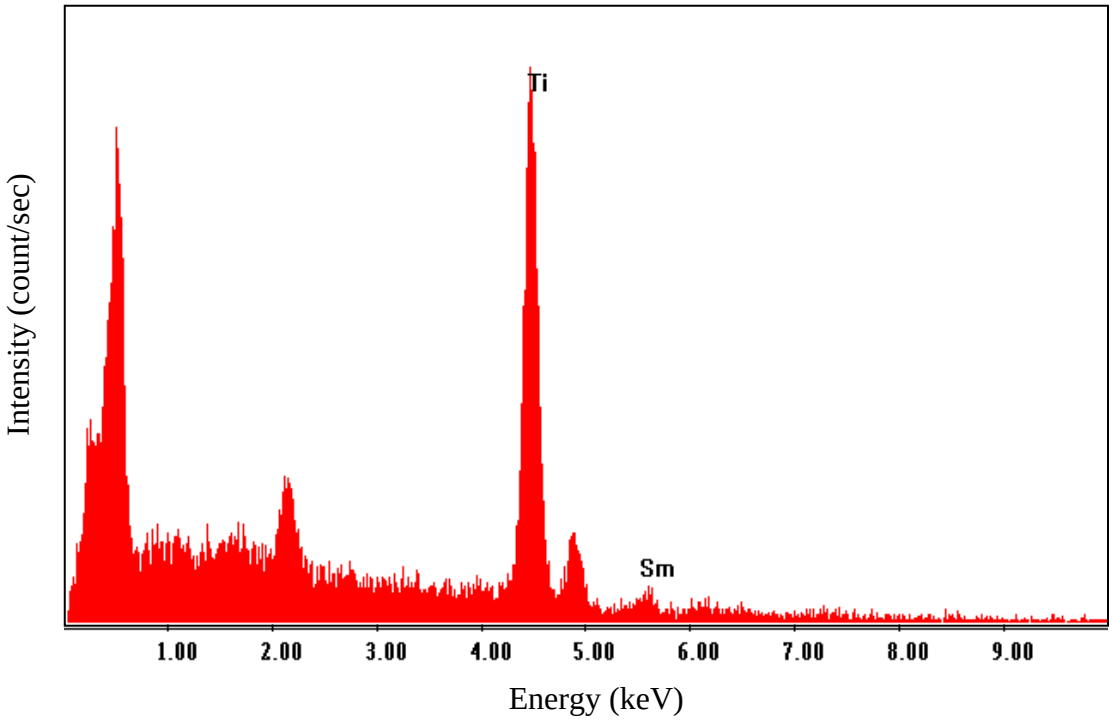

Figure 46 EDX spectrum shows the semiquantification of each elements composition in 38.58 %wt Sm doped TiO_2 catalyst calcined at 500^{o}C.

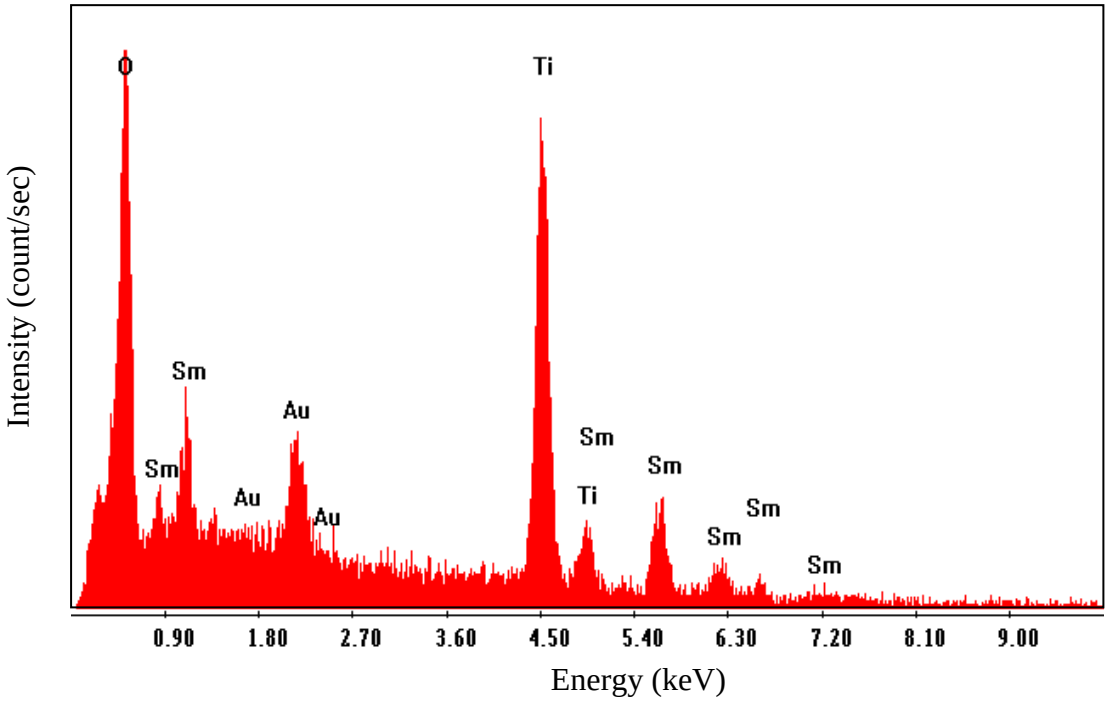

Figure 47 EDX spectrum shows the semiquantification of each elements composition in 55.68 %wt Sm doped TiO_2 catalyst calcined at 500^{o}C.

2.6 Transmission electron microscope (TEM)

The particle size of all catalysts were determined by TEM images. Figure 48 showed TEM image of P-25 TiO_2 which can obviously notice the difference in size of particles. In contrast, TEM images of the prepared catalysts (Figure 49 to 53) showed that size of particles were in nanometer range and the average size distribution of each particle was not much different from each other. In case of Sm doping, the distribution range of particle size was much more narrow than the undoped TiO_2 and P-25. These concluded that Sm ion could hinder the increase of particle size and decrease the extension of size distribution during agglomeration in calcination step. Additionally, the dark area appear on the cluster of particle would be generated from Sm atoms which disperse in TiO_2 structure from doping. Due to higher atomic weight of Sm, the less light transmitting as a result, then dark area can be generated. The results indicated that Sm atoms were homogeneous dispersed in TiO_2 structure .This corresponded to SEM/EDX results which used to quantified the amount of Sm doping, amount of Sm doping analyzed by EDX were similar to amount of Sm doping in the preparation process.

The size distribution from TEM data are shown in Figure 54 to 59. Particle size of Sm doped TiO_2 was smaller than the undoped TiO_2.The average particle size of P-25 and prepared catalysts calculated from TEM data were in range of 10 to 36 nanometers as shown in Table 14. With higher calcination temperature, the particle size was increased, resemble with the calculation data from XRD. These can conclude that Sm ion could hinder the increase of crystallite size during calcinations as described before.

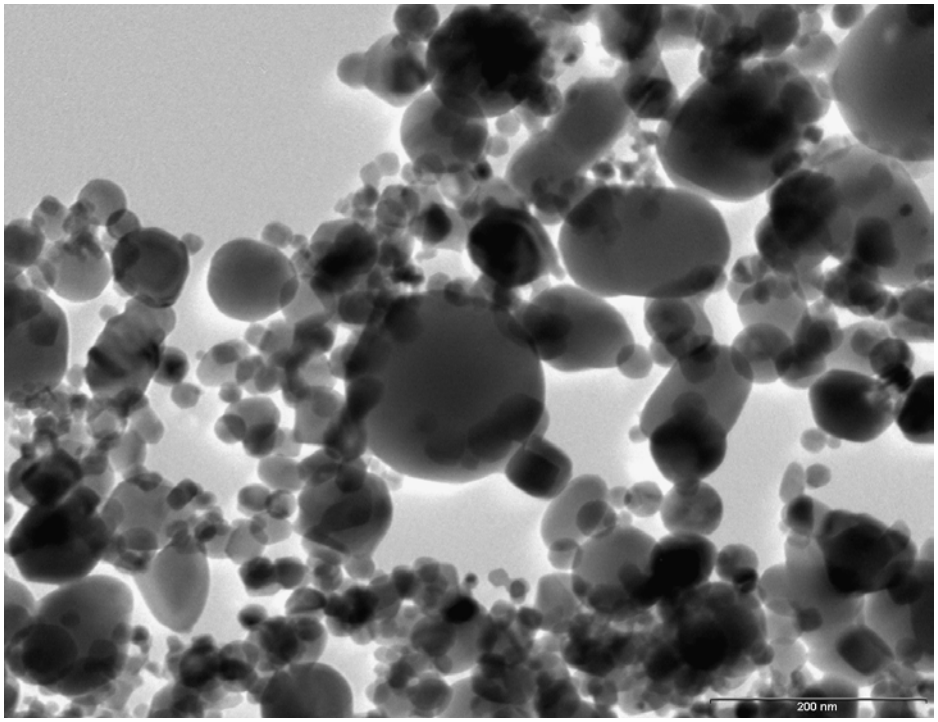

Figure 48 TEM image of P-25 TiO_2 at 1000X magnification.

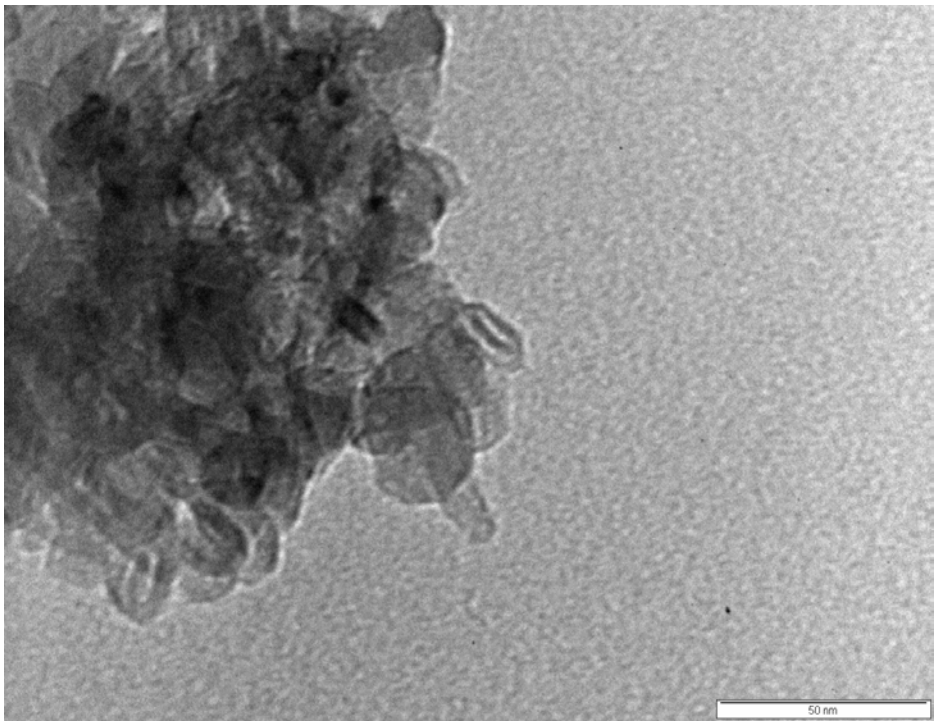

Figure 49 TEM image of undoped TiO_2 calcined at 500^oC at 1000X magnification.

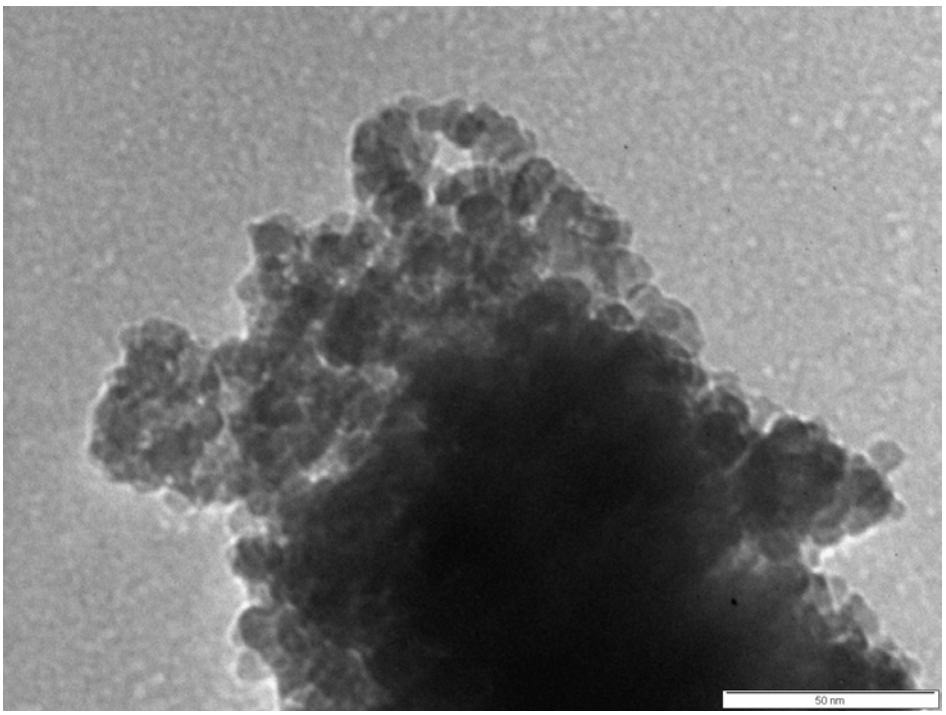

Figure 50 TEM image of 13.57 %wt Sm doped TiO_2 calcined at 500^{o}C at 1000X magnification.

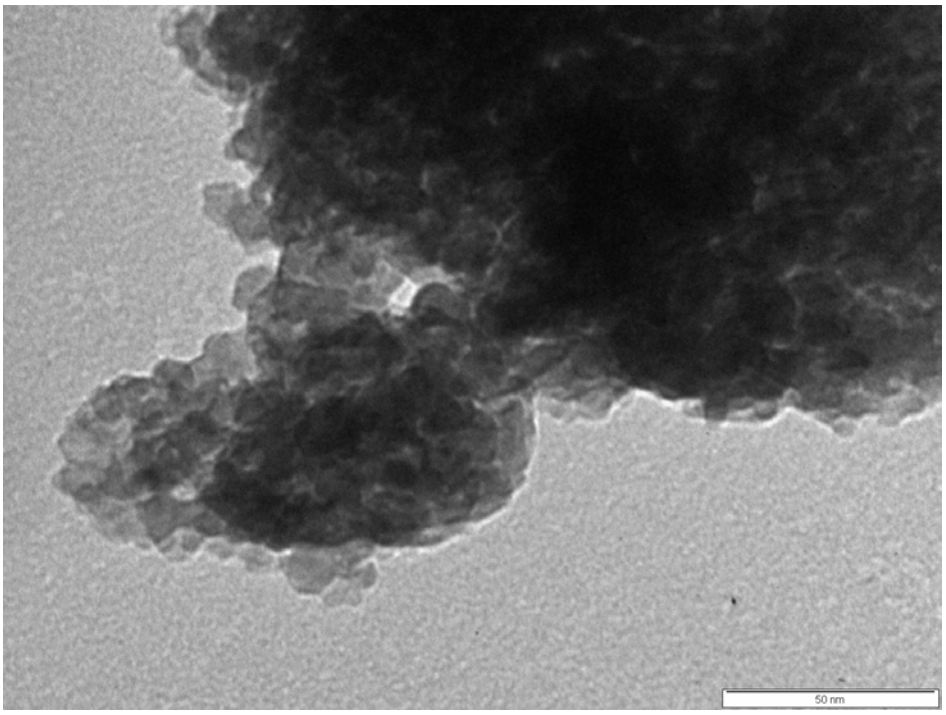

Figure 51 TEM image of 23.90 %wt Sm doped TiO_2 calcined at 500^{o}C at 1000X magnification.

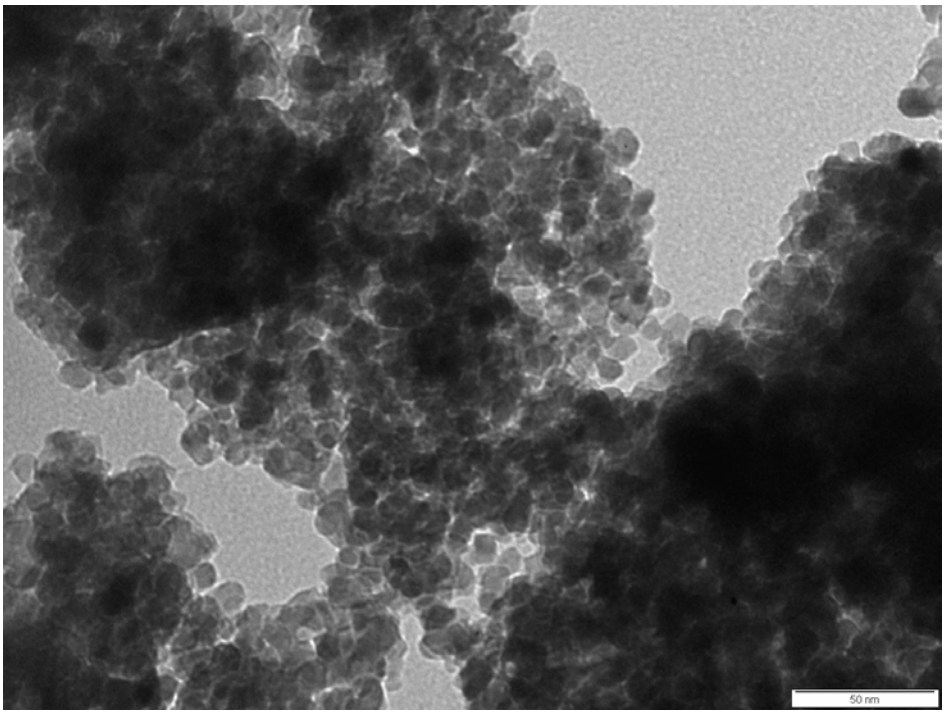

Figure 52 TEM image of 55.68 %wt Sm doped TiO_2 calcined at 500^{o}C at 1000X magnification.

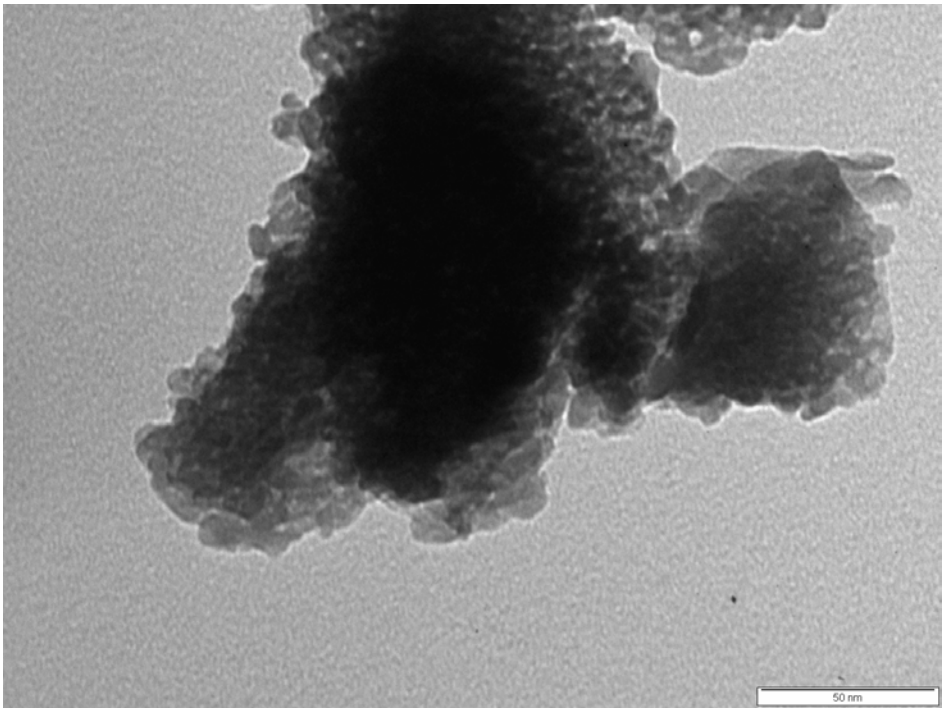

Figure 53 TEM image of 13.57 %wt Sm doped TiO_2 calcined at 700^{o}C at 1000X magnification.

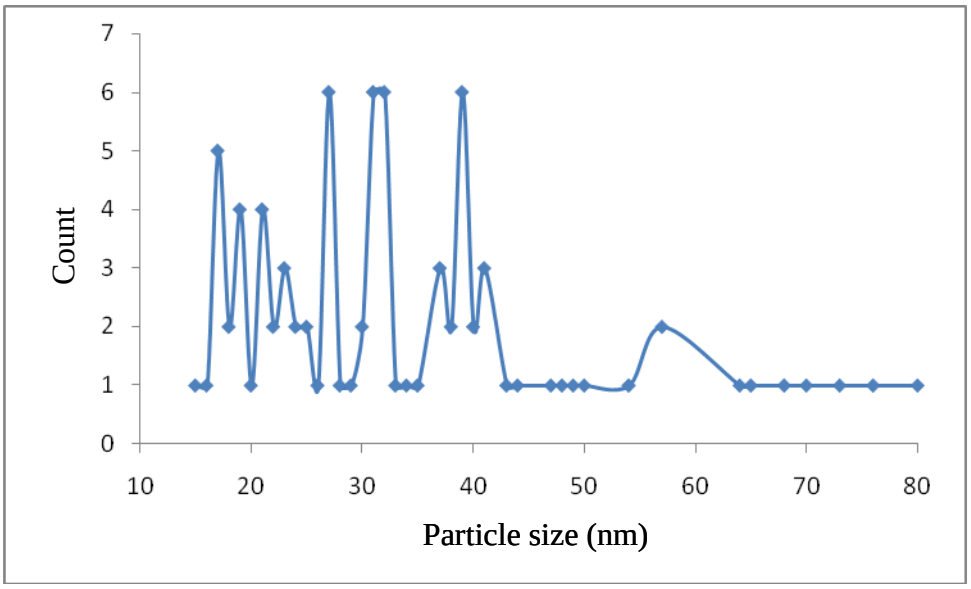

Figure 54 Size distribution from TEM data of P-25 TiO_2.

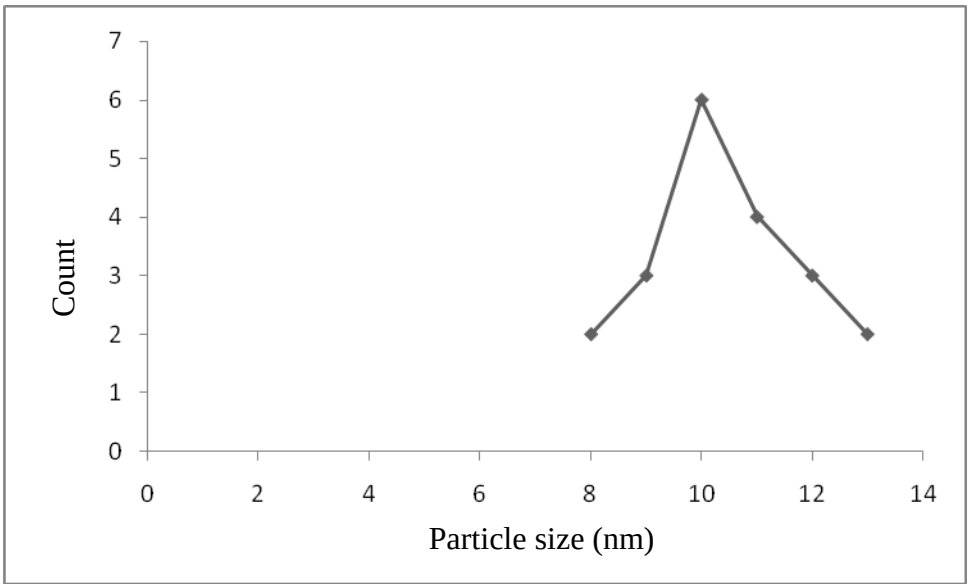

Figure 55 Size distribution from TEM data of 13.57 %wt Sm doped TiO_2 calcined at 500^{o}C.

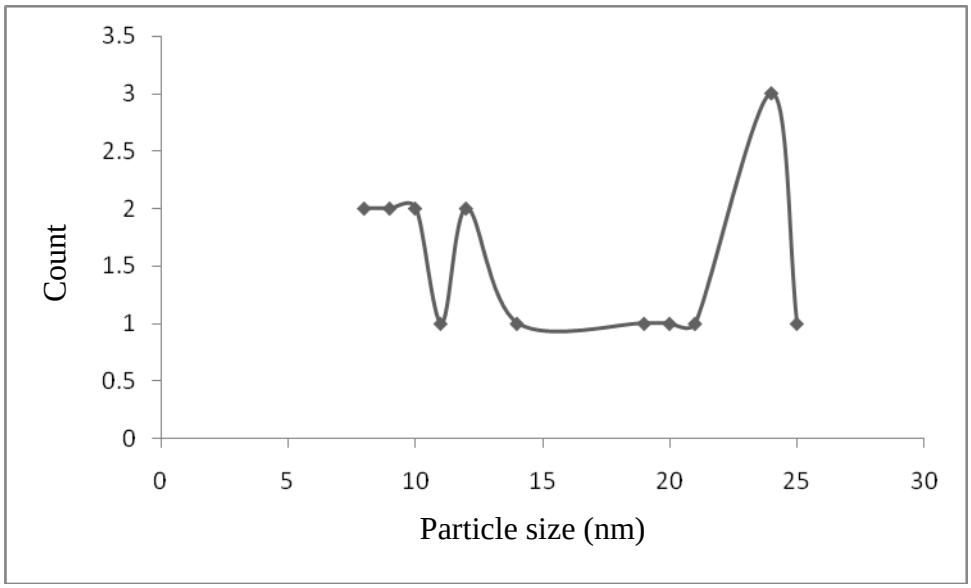

Figure 56 Size distribution from TEM data of 23.90 %wt Sm doped TiO_2 calcined at 500^{o}C.

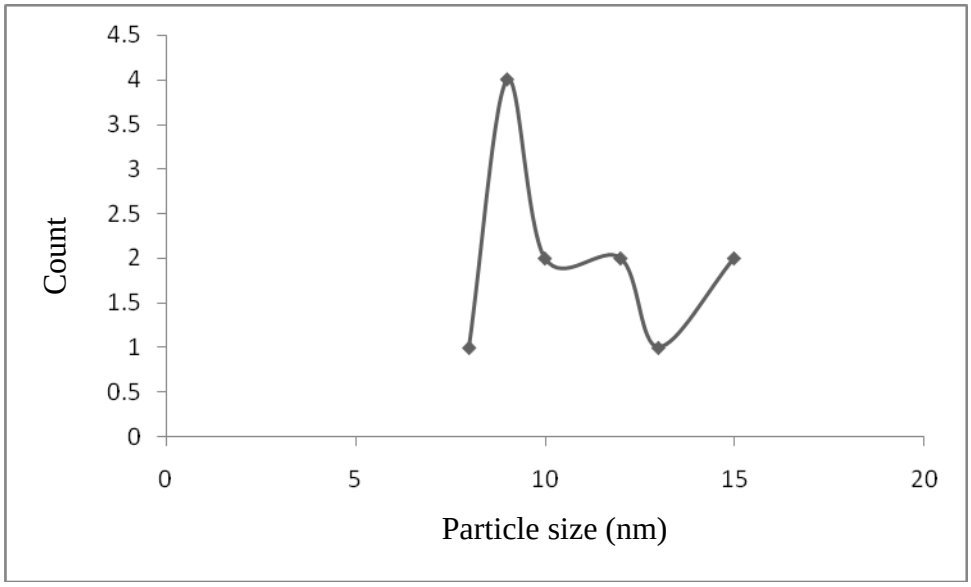

Figure 57 Size distribution from TEM data of 55.68 %wt Sm doped TiO_2 calcined at 500^{o}C.

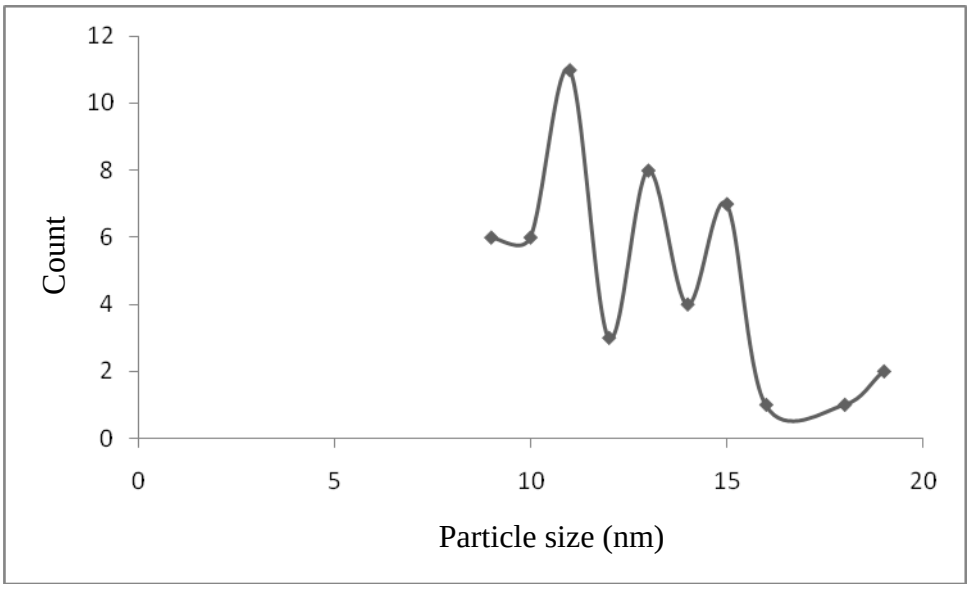

Figure 58 Size distribution from TEM data of 13.57 %wt Sm doped TiO_2 calcined at 600^{o}C.

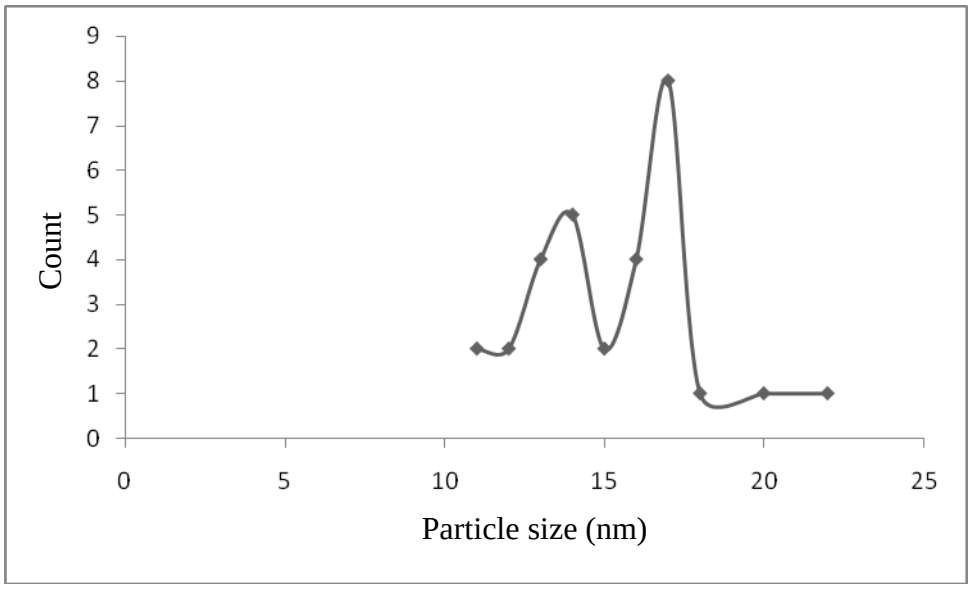

Figure 59 Size distribution from TEM data of 13.57 %wt Sm doped TiO_2 calcined at 700^{o}C.

Table 14 Average size of prepared TiO_2 catalysts compared to P-25 TiO_2 determined by TEM data.

Catalyst	Amount of Sm (%wt)	Calcination temperature (^oC)	Average size* (nm)
P-25 TiO_2	-	-	36.89
Sm doped TiO_2	13.57	500	10.32
Sm doped TiO_2	13.57	600	12.35
Sm doped TiO_2	13.57	700	15.31
Sm doped TiO_2	23.90	500	11.06

* The full data of particle size from TEM was shown in Appendix F.

2.7 Brunauer-Emmett-Teller (BET)

Table 15 Surface information of the prepared catalysts compared to P-25 TiO_2 calculated by BET method.

Catalyst	%wt of Sm	BET surface area (m^2/g)	Langmuir surface area (m^2/g)	Average pore size (Å)
P-25 TiO_2	0	98.71	75.13	52.77
Undoped TiO_2	0	12.98	13.94	53.52
Sm doped TiO_2	13.57	113.84	108.68	46.69
Sm doped TiO_2	23.90	120.27	112.30	28.47

From the surface area data (Table 15), both BET surface area and Langmuir surface area of prepared undoped TiO_2 catalyst are much less than P-25 TiO_2. This indicated that the particle size of prepared undoped TiO_2 catalysts was larger than P-25. But the surface area of Sm doped TiO_2 were higher than undoped TiO_2 and also P-25. This evidence showed that Sm doping had effected on particle size and surface area of the prepared catalysts. With Sm doping, the particle size was decreased then surface area increased. More amount of Sm doped gave higher surface area and smaller size. Correspond to the XRD data, this indicated that Sm ion could hinder the increase of particle size during calcinations.

3. Photocatalysis of PAHs compounds

3.1 Calibration curve of standard phenanthrene

A series of solutions of phenanthrene was quantified by UV-Vis spectroscopy. The absorbance of maximum wavelength at 251 nm were plotted against concentration of phenanthrene from 0 to 20 ppm as shown in Figure 60.

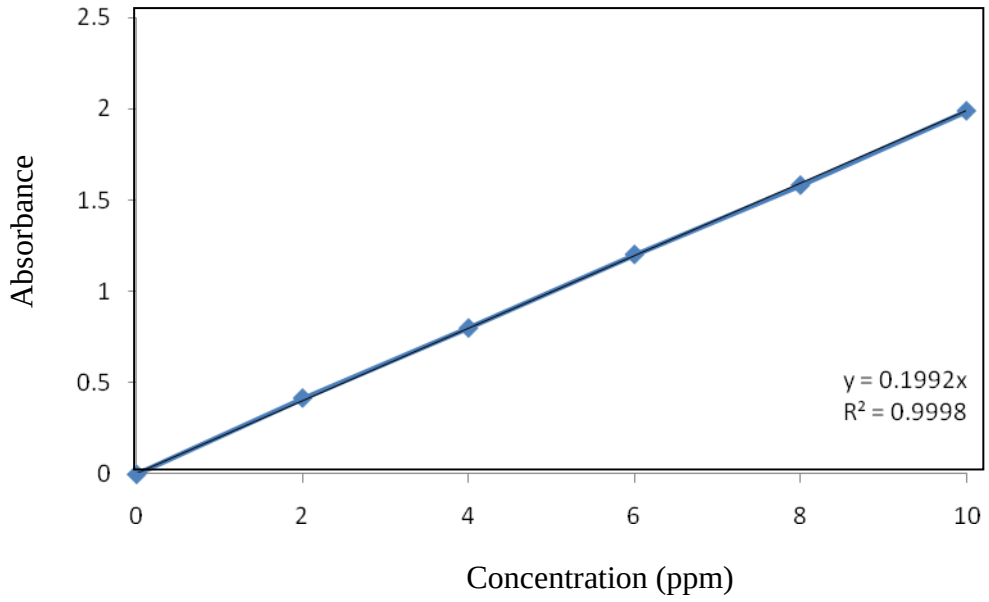

Figure 60 Calibration curve of phenanthrene at concentration from 0-10 ppm.

3.2 Photodegradation of phenanthrene

The absorbance of phenanthrene after degraded in each 30 minutes interval under visible light were quantified by UV-Vis spectroscopy at the maximum wavelength of 251 nm. The photodegradation results are shown in Figure 61 to 66. Figure 61, 62, 63 and 64 showed the photodegradation of phenathrene without catalyst, using P-25 TiO_2, undoped TiO_2 and Sm doped TiO_2 catalyst respectively, under the same condition, 125 ml of 200 ppm phenanthrene solution with 0.1 grams of catalyst. All catalysts were calcined at 500^{o}C. The photodegadation of phenanthrene without catalyst was very slow. The conversion of phenanthrene was only 4.58% within 4.5 hours. However, the degradation using catalyst gave much higher % of conversion. The results indicated that Sm doped TiO_2 catalyst was more effective for degradation of phenanthrene in optimized condition than preparing undoped TiO_2 and P-25 in overall degradation reaction. Although P-25 could degraded phenathrene faster than both preparing catalysts at the beginning of degradation. However at the end, the remaining of phenanthrene using Sm doped TiO_2 was lower than undoped TiO_2 and P-25. The reason for the faster degradation rate of phenanthrene using P-25 at the beginning may due to the particle size of catalyst. The particle size of P-25 was very fine with higher surface area than the preparing catalyst due to the milling process in commercial industry.

In case of Sm doped catalyst, the degradation rate of phenanthrene was faster than P-25 and undoped TiO_2. Propose that the rate of degradation was the first order reaction from the plotting between log of concentration versus time, which was linear relation as shown in Figure 67 to 70. The rate constant (k) was related to the slope of the plot which can be calculated by assumption that the degradation of phenanthrene was first order reaction. The rate constants (k) of photocatalytic degradation of phenanthrene with different catalysts were shown in Table 16. The calculation in full was shown in Appendix G.

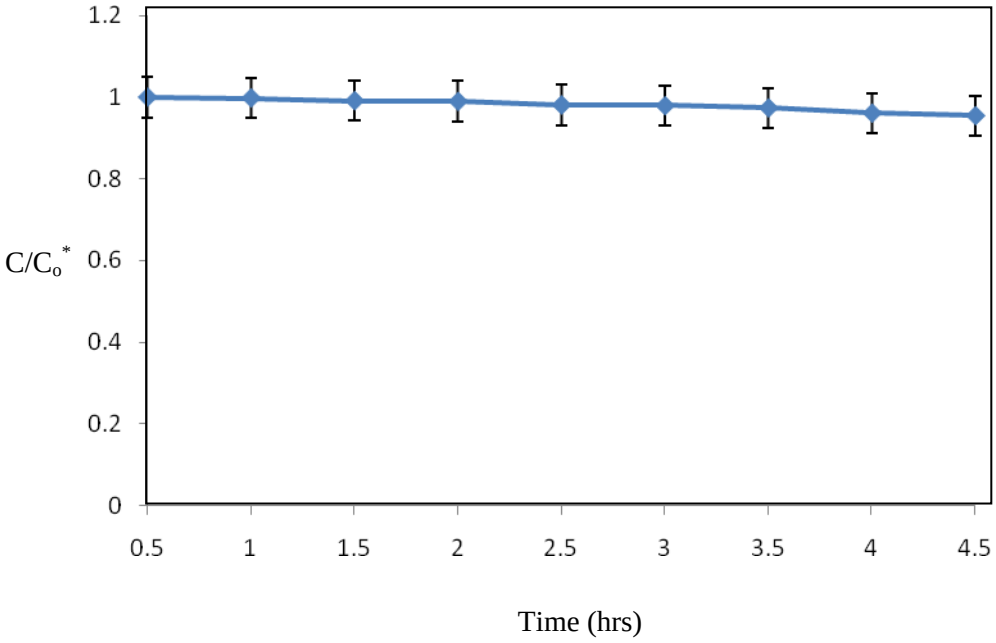

Figure 61 The photodegradation of phenanthrene without catalyst.

* C/C_0 is the ratio of remain concentration of sample divide by the initial concentration.

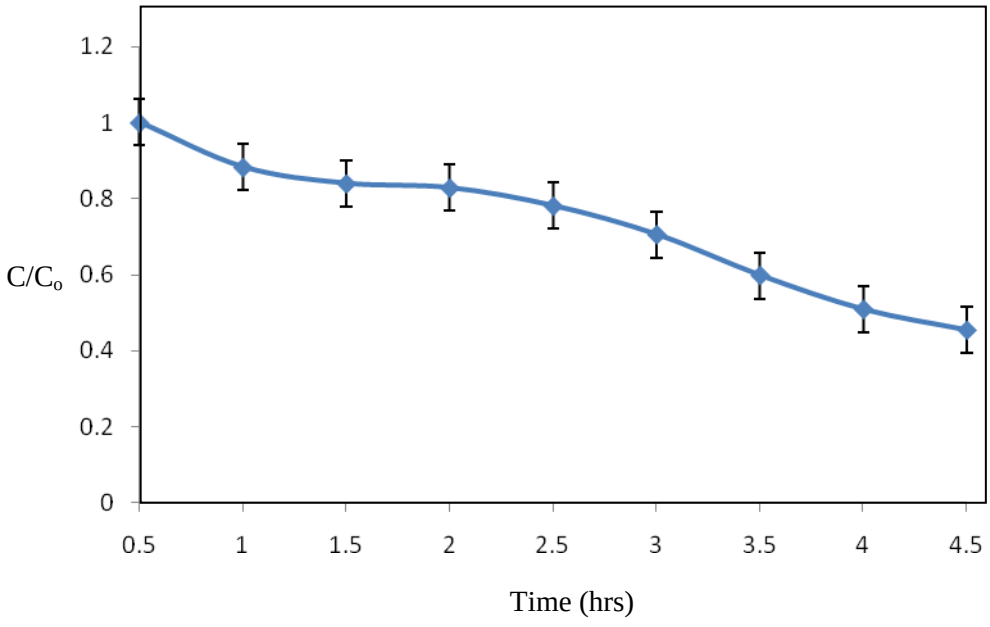

Figure 62 The photodegradation of 20 ppm phenanthrene using 0.1 g of P-25 TiO_2.

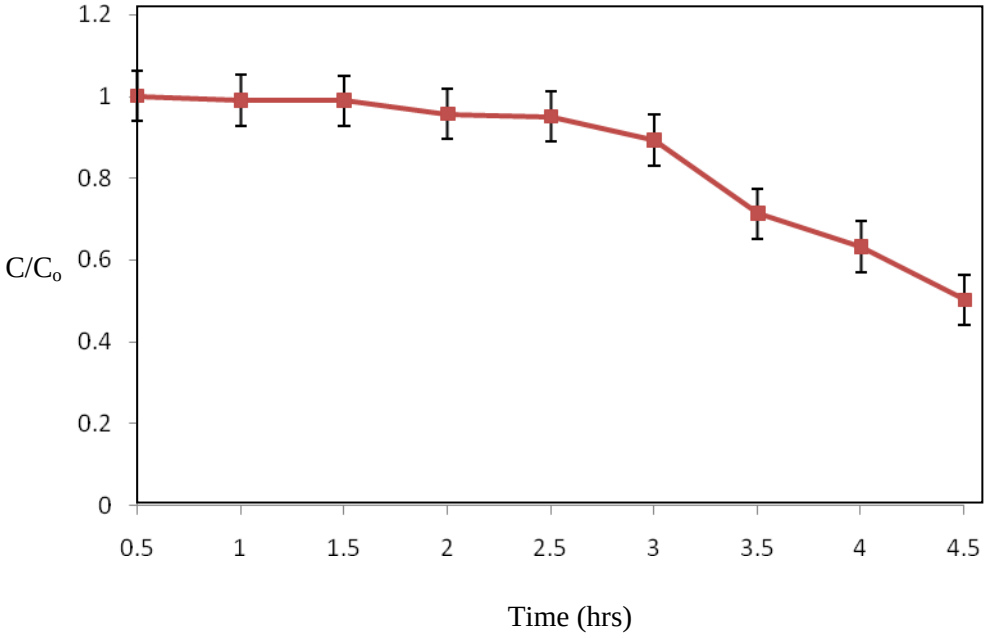

Figure 63 The photodegradation of 20 ppm phenanthrene using 0.1 g of undoped TiO_2.

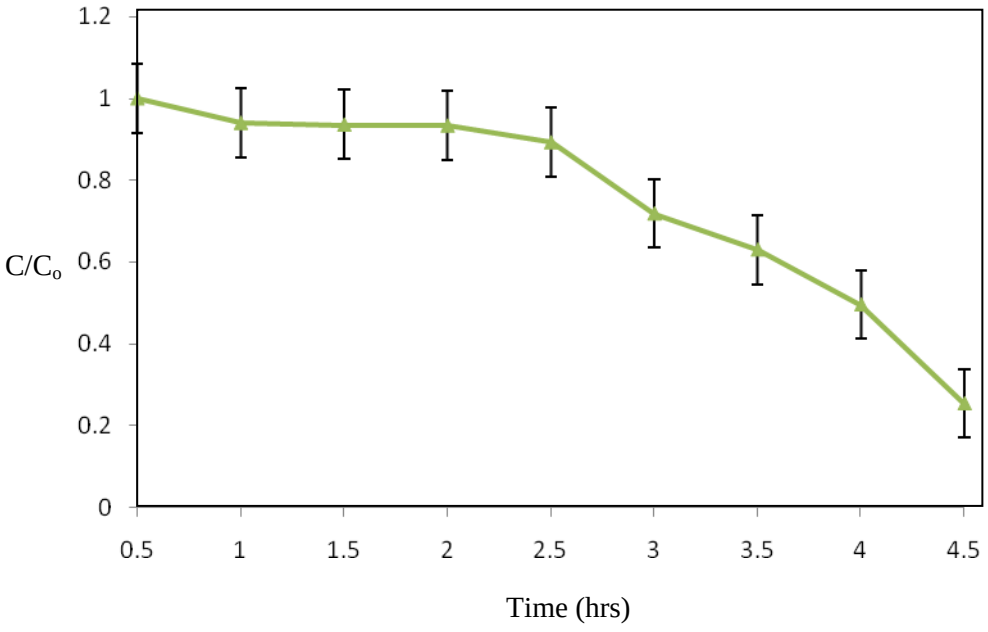

Figure 64 The photodegradation of 20 ppm phenanthrene using 0.1g of 13.57 %wt

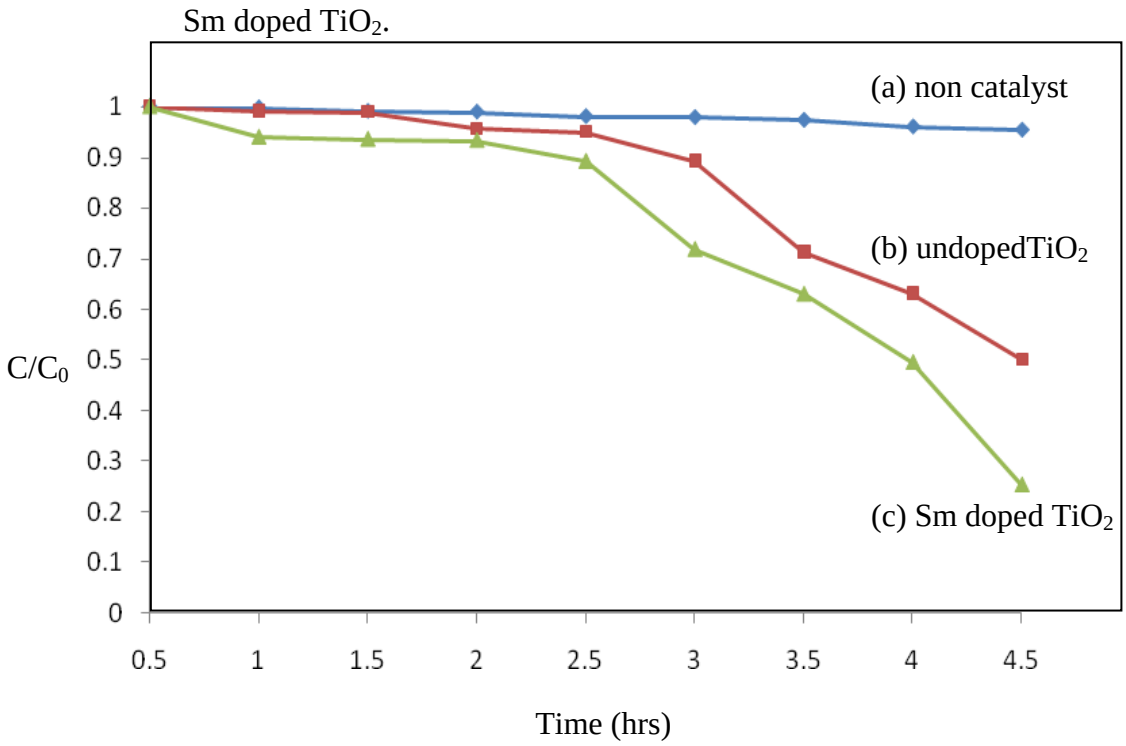

Figure 65 The photodegradation of 20 ppm phenanthrene (a) without catalyst, (b) using 0.1 g of undoped TiO_2 and (c) 0.1 g of 13.57% Sm doped TiO_2 catalysts calcined at 500^{o}C.

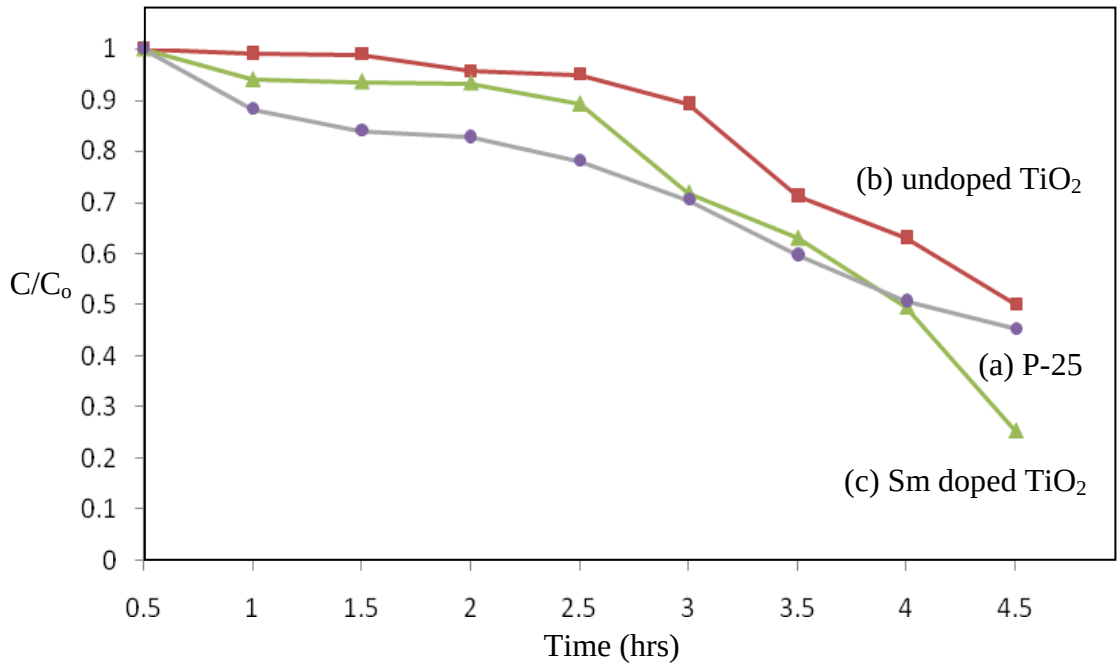

Figure 66 The photodegradation of 20 ppm phenanthrene using (a) 0.1 g of P-25 TiO_2, (b) 0.1 g of undoped TiO_2 and (c) 0.1 g of 13.57 %wt Sm doped

TiO_2 catalysts calcined at 500^oC.

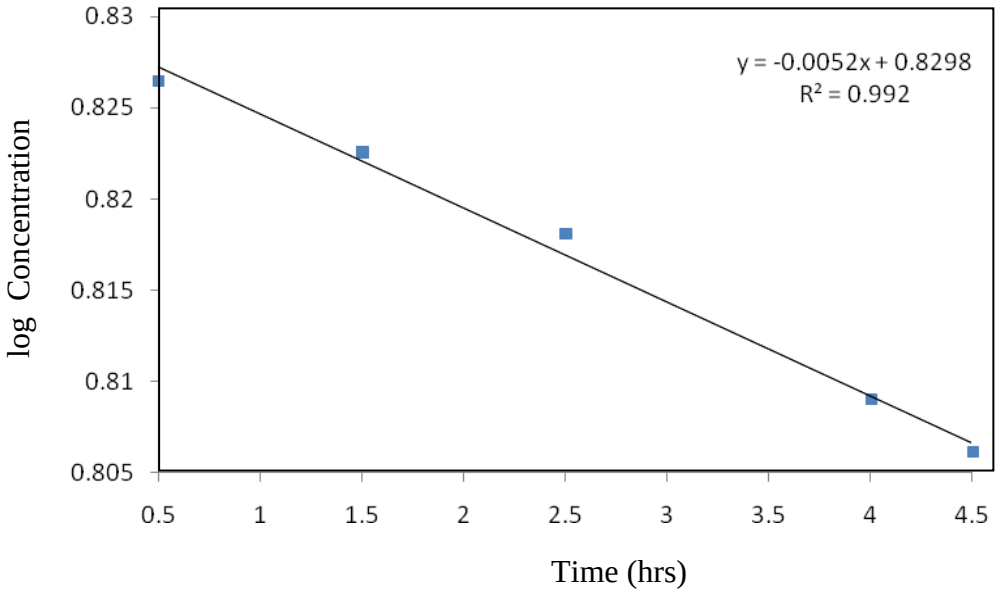

Figure 67 Plotted of log concentration versus time to determine the photodegradation rate of 20 ppm phenanthrene under visible light without catalyst.

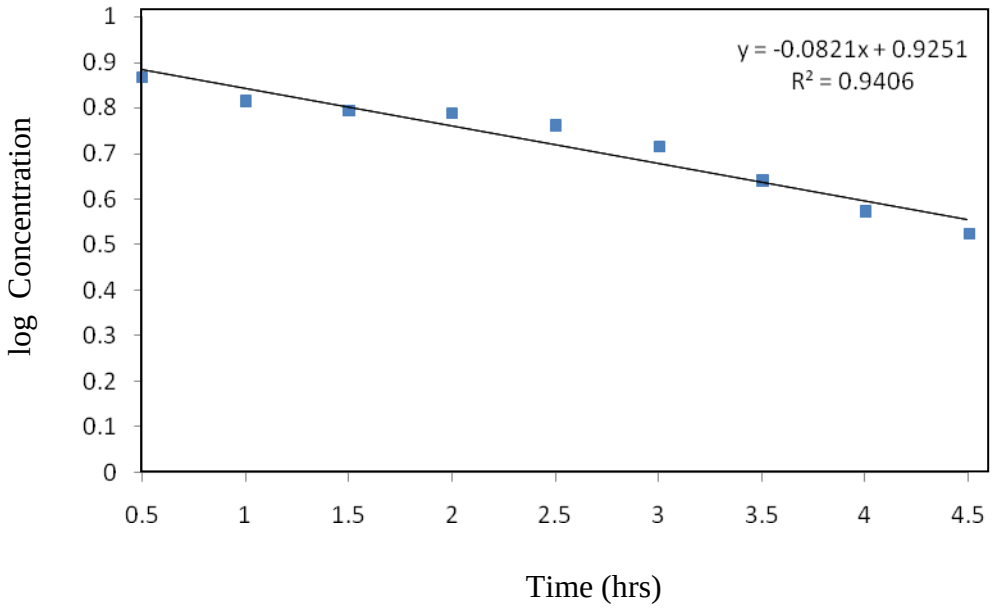

Figure 68 Plotted of log concentration versus time to determine the photodegradation rate of 20 ppm phenanthrene under visible light using 0.1g of P-25 TiO_2.

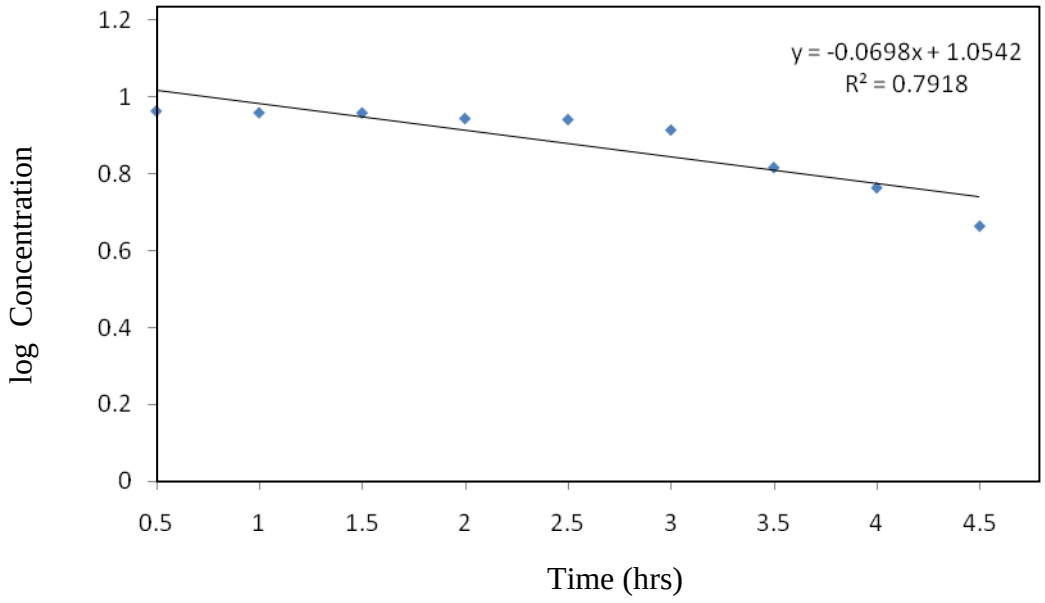

Figure 69 Plotted of log concentration versus time to determine the photodegradation rate of 20 ppm phenanthrene under visible light using 0.1 g of undoped TiO_2 catalyst calcined at 500^oC.

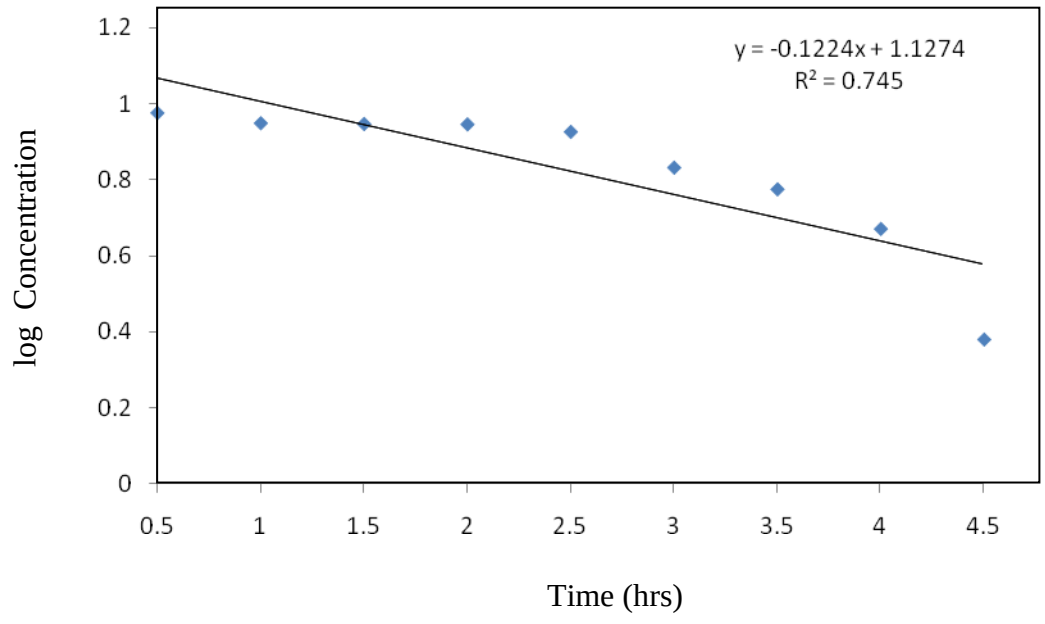

Figure 70 Plotted of log concentration versus time to determine the photodegradation rate of 20 ppm phenanthrene under visible light using 0.1g of 13.57 %wt Sm doped TiO_2 catalyst calcined at 500^oC.

Table 16 Rate constant and half life of photodegradation of 20 ppm phenanthrene without catalyst and using 0.1 g of P-25 TiO_2, 0.1 g of undoped TiO_2 and 0.1 g of 13.57 %wt Sm doped TiO_2 catalysts.

Catalyst	% Conversion	R^2	Rate constant (hrs^{-1})	$t_{1/2}$ (hrs)
Non catalyst	4.58	0.992	0.0119	57.86
P-25 TiO_2	54.63	0.941	0.1891	3.67
Undoped TiO_2	49.76	0.792	0.1608	4.31
Sm doped TiO_2	74.62	0.745	0.2819	2.46

* Calculation of all parameters are shown in Appendix E.

From table 16, the rate constant of photodegradation using Sm doped TiO_2 was faster than using P-25 TiO_2 and undoped TiO_2, the conversion of phenanthrene using Sm doped TiO_2 was more effective. Conclude that Sm doping could improve the catalytic activity of TiO_2 under visible light.

The results also showed the half life of phenanthrene under photocatalytic degradation using TiO_2 and Sm doped TiO_2 were in the range of 2 to 5 hours. Usually, the half life of phenanthrene in atmosphere and soil are 2 - 20 hours and 16 - 200 days, respectively (Sanghvi, 2005).

Different calcination temperatures gave different results (Figure 71 to 74), catalyst which calcined at 500^{o}C was the most effective catalyst compared with calcined at 450^{o}C and 600^{o}C in the same condition and the same amount of Sm doping.

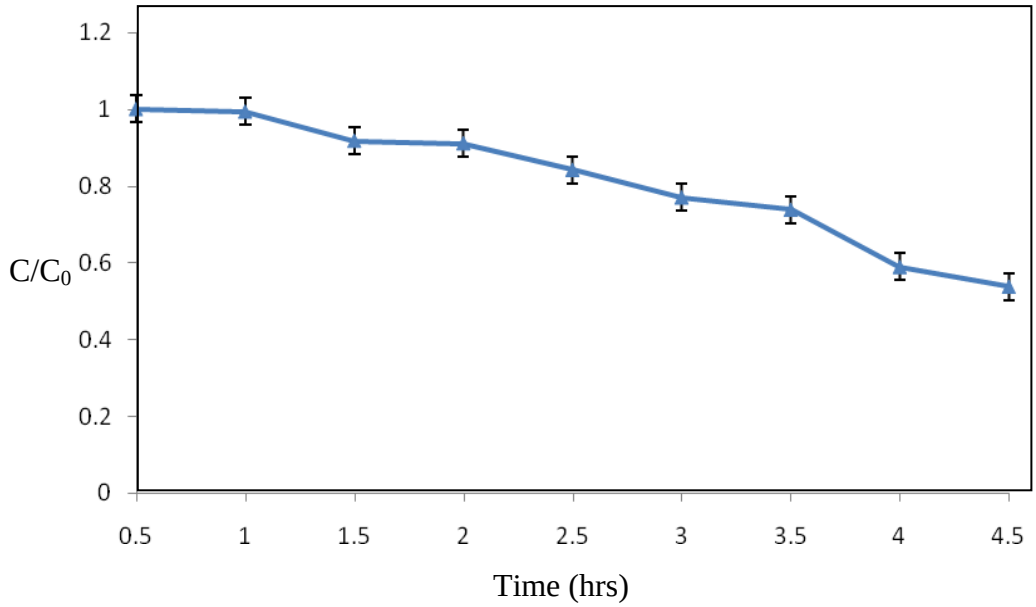

Figure 71 The photodegradation of 20 ppm phenanthrene using 0.1g of 13.57 %wt Sm doped TiO_2 calcined at 450^{o}C.

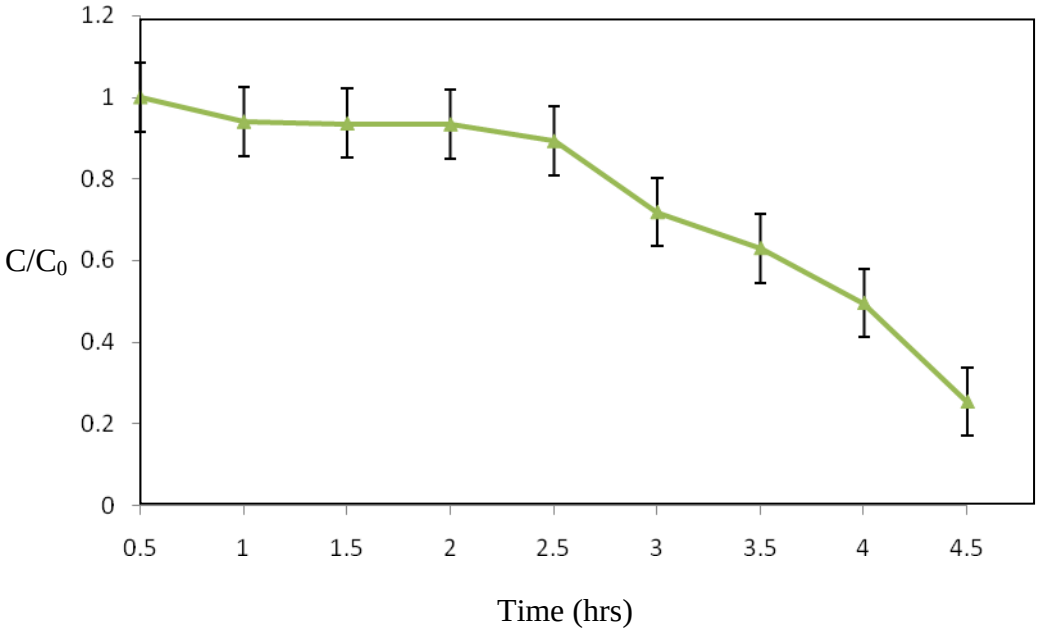

Figure 72 The photodegradation of 20 ppm phenanthrene using 0.1 g of 13.57 %wt Sm doped TiO_2 calcined at 500^{o}C.

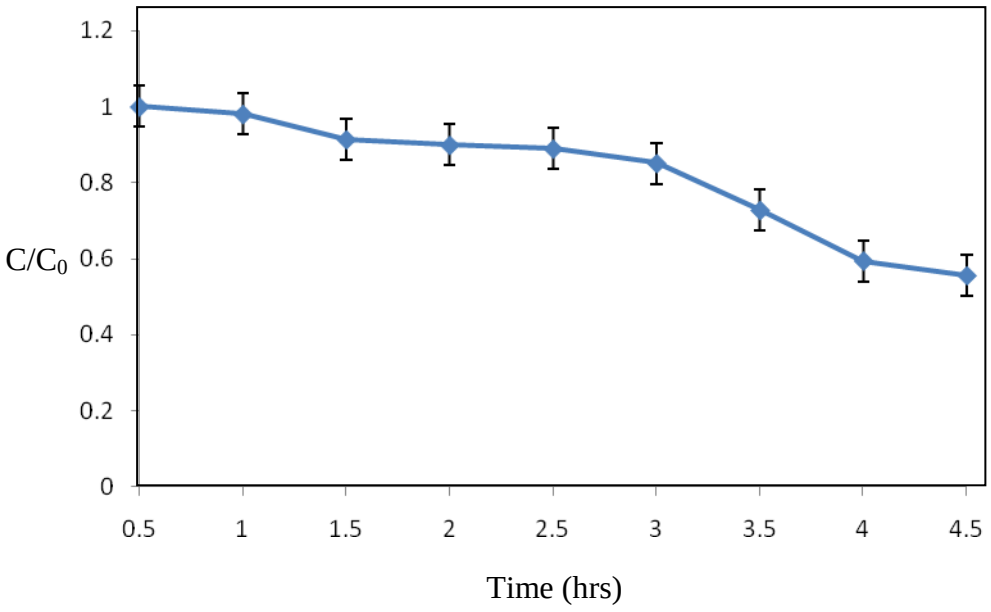

Figure 73 The photodegradation of 20 ppm phenanthrene using 0.1 g of 13.57 %wt Sm doped TiO_2 calcined at 600°C.

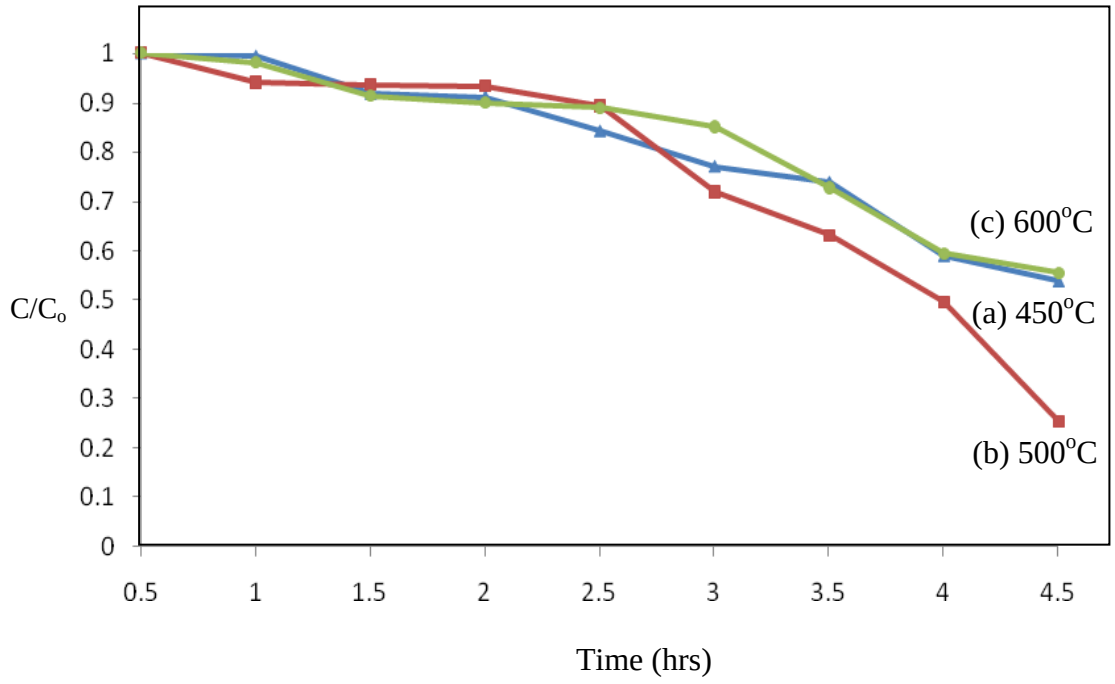

Figure 74 The Photodegradation of 20 ppm phenanthrene using 0.1 g of 13.57 %wt Sm doped TiO_2 catalysts calcined at different temperatures (a) 450°C, (b) 500°C and (c) 600°C.

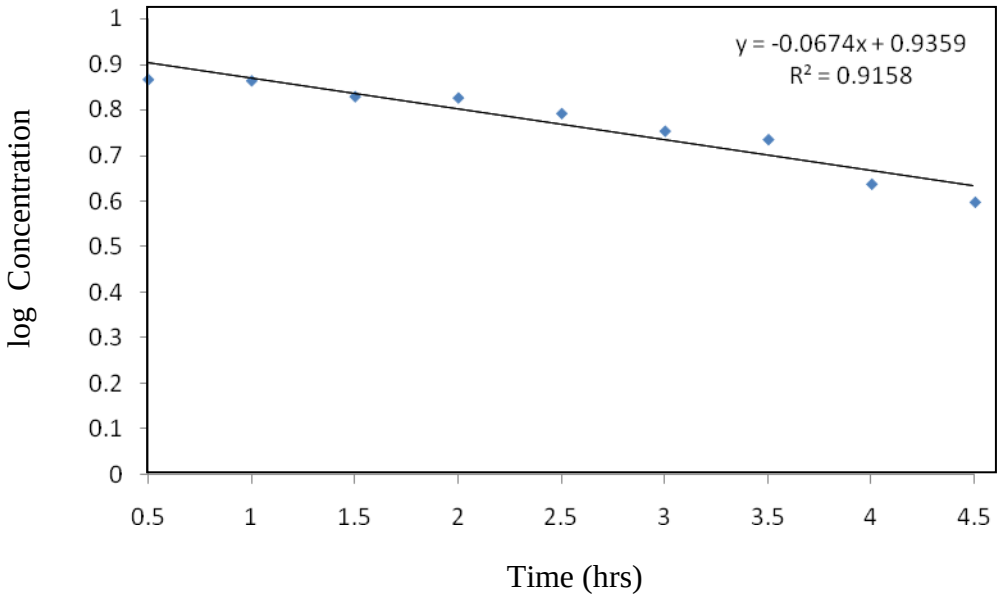

Figure 75 Plotted of log concentration versus time to determine the photodegradation rate of 20 ppm phenanthrene under visible light using 0.1 g of 13.57 %wt Sm doped TiO_2 catalyst calcined at 450^{o}C.

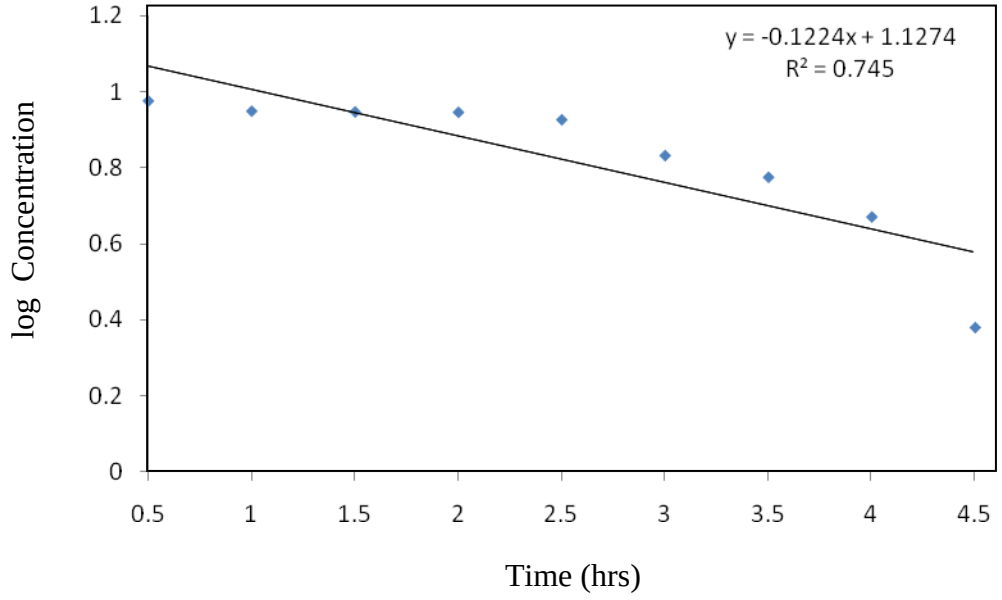

Figure 76 Plotted of log concentration versus time to determine the photodegradation rate of 20 ppm phenanthrene under visible light using 0.1 g of 13.57 %wt Sm doped TiO_2 catalyst calcined at 500^{o}C.

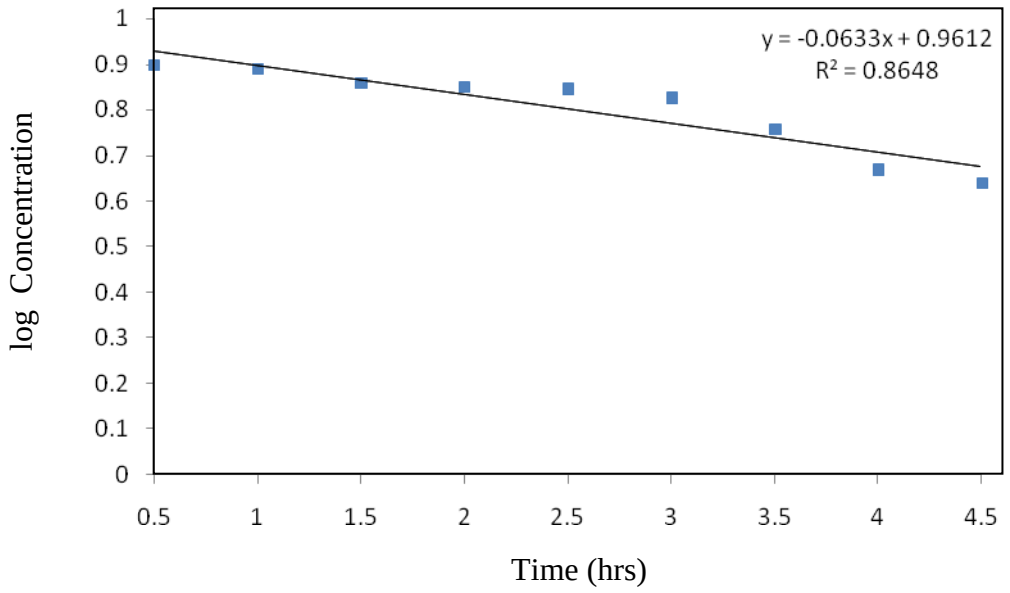

Figure 77 Plotted of log concentration versus time to determine the photodegradation rate of 20 ppm phenanthrene under visible light using 0.1 g of 13.57 %wt Sm doped TiO_2 catalyst which calcined at 600^oC.

Table 17 Rate constant and half life of photodegradation of 20 ppm phenanthrene using 0.1 g of 13.57 %wt Sm doped TiO_2 calcined with different temperatures.

Calcination temperature (^oC)	% Conversion	R^2	Rate constant (hrs^{-1})	$t_{1/2}$ (hrs)
450	46.24	0.916	0.1548	4.48
500	74.62	0.745	0.2819	2.46
600	44.50	0.865	0.1458	4.75

Table 17 showed the rate constant and % conversion of phenanthrene using Sm doped TiO_2 with different calcination temperatures. The results showed that catalyst which calcined at 450^o has less % conversion and rate constant compared to 500^oC. This due to the crystallinity of anatase TiO_2 calcined at 500^oC was higher than 450^oC. Moreover, catalyst which calcined at 600^o also had less % conversion and rate constant compared to 500^oC. This because TiO_2 calcined at 600^oC has larger crystallite size and smaller surface area than TiO_2 which calcined at 500^oC, resulted in the lower photocatalytic activity.

Also the different percentages of Sm loading gave different results which shown in Figure 78. As increasing amount of Sm on doping, the degradation rate was decreased. This due to exceeding of Sm loaded on catalyst, as a consequence, the catalyst was amorphous solid or Sm species dispersed on anatase surface. These reduce the activity of catalyst as a result.

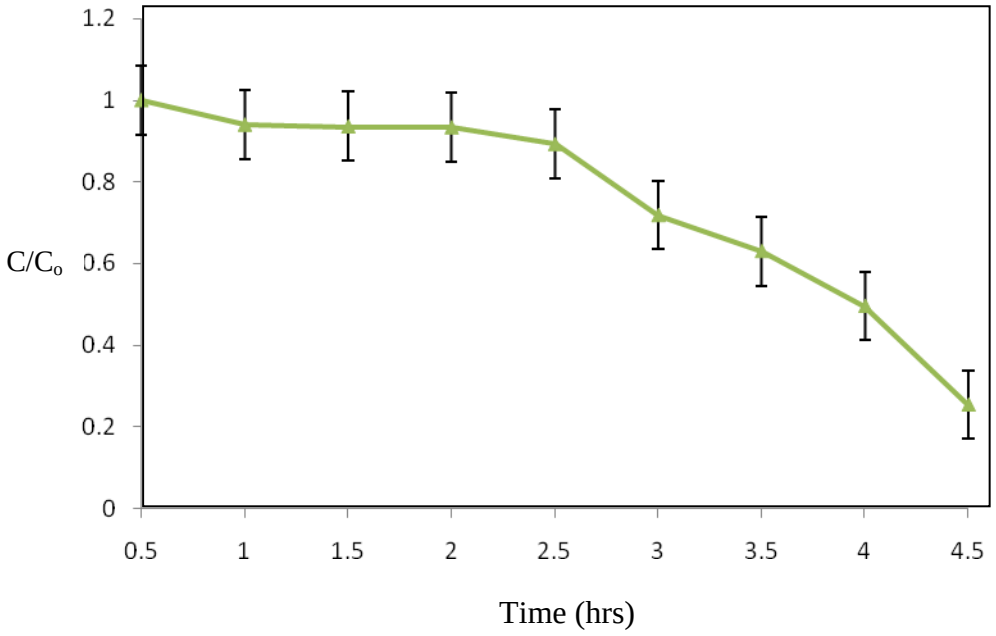

Figure 78 The photodegradation of 20 ppm phenanthrene using 0.1g of 13.57 %wt Sm doped TiO_2 calcined at 500^{o}C.

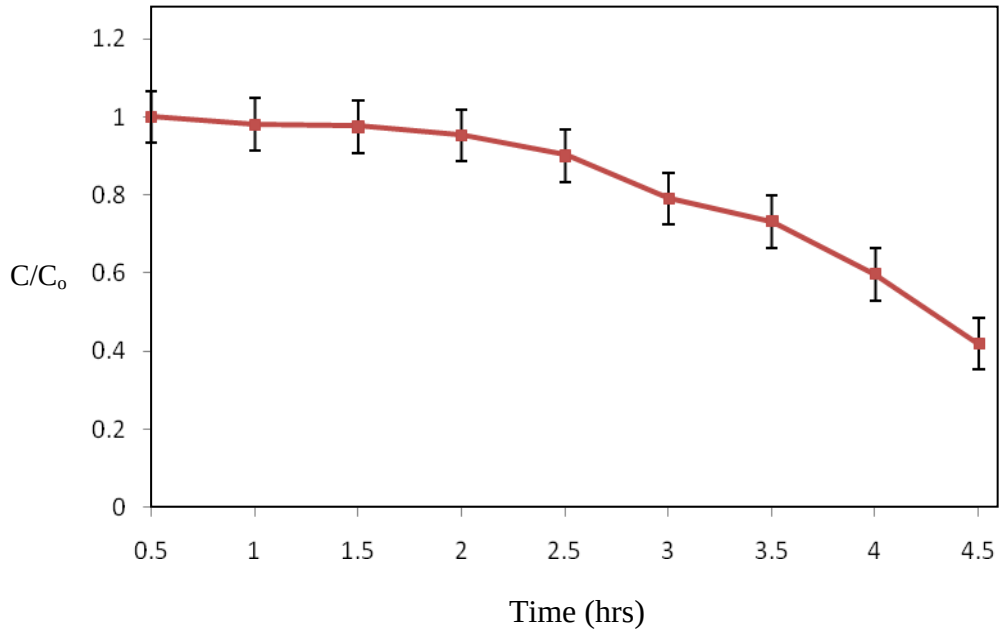

Figure 79 The photodegradation of 20 ppm phenanthrene using 0.1g of 23.90 %wt Sm doped TiO_2 calcined at 500^{o}C.

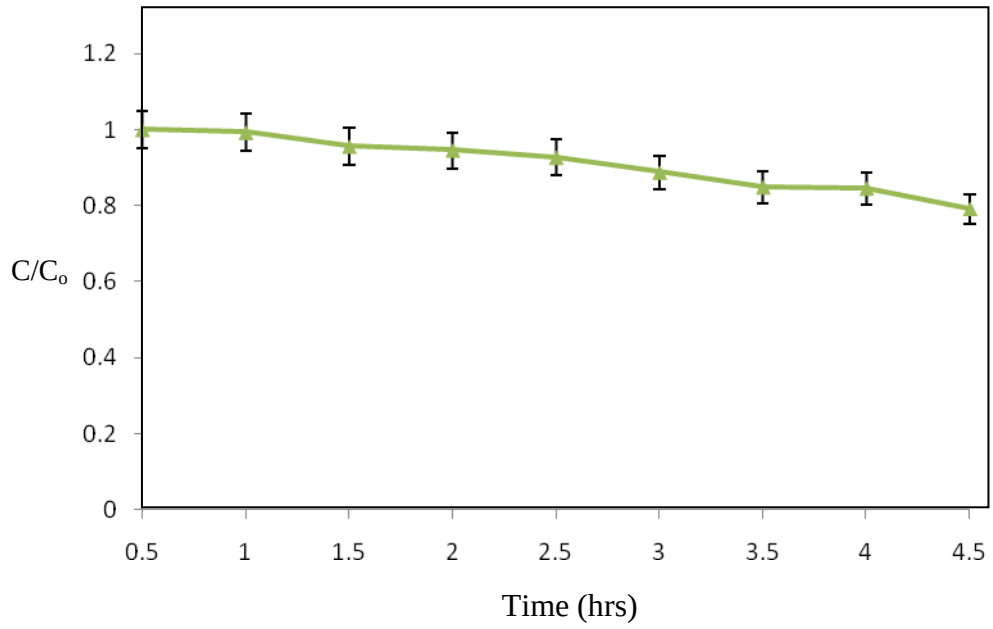

Figure 80 The photodegradation of 20 ppm phenanthrene using 0.1g 55.68 %wt Sm doped TiO_2 calcined at 500°C.

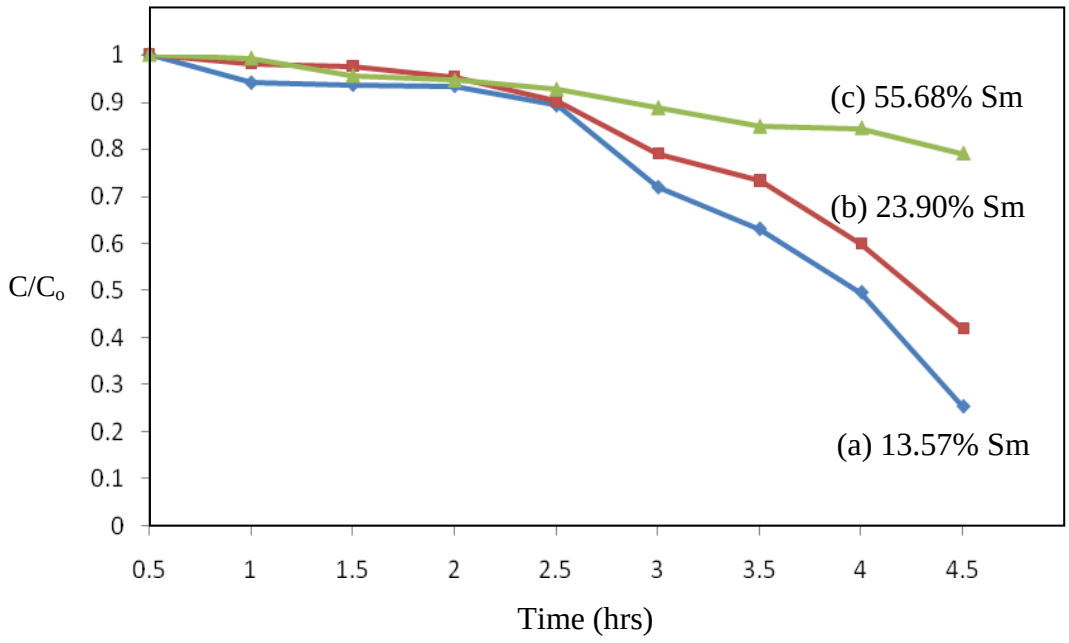

Figure 81 The photodegradation of 20 ppm phenanthrene using 0.1 g of Sm doped TiO_2 catalysts with various amount of Sm doping (a) 13.57 %wt Sm, (b) 23.90 %wt Sm and (c) 55.68 %wt Sm doped TiO_2 calcined at 500°C.

With the same procedure of calculation which mention above, rate constant of photocatalytic degradation of phenanthrene using Sm doped TiO_2 with various amount of Sm were shown in Table18.

Table 18 Rate constant and half life of photodegradation of 20 ppm phenanthrene using 0.1 g of Sm doped TiO_2 with various amount of Sm.

% Sm doping	% Conversion	R^2	Rate constant (hrs^{-1})	$t_{1/2}$ (hrs)
13.57	74.62	0.745	0.2819	2.46
23.60	58.08	0.798	0.1907	3.63
55.68	20.91	0.964	0.0573	12.08

Due to the exceeding of Sm doping on TiO_2, the activity of catalyst was decreased as discussed before. The results in Table 18 confirmed this assumption, the higher amount of Sm doping the lower % conversion and rate constant as a result. However we can conclude that Sm doped TiO_2 catalyst prepared by sol-gel technique could improve activity in photocatalysis degradation of phenanthrene over undoped TiO_2.

3.3 Calibration curve of standard benzo[a]anthracene

A series of solutions of benzo[a]anthracene was quantified by fluorescene spectroscopy. The intensity of fluorescent at excitation wavelength at 287 nm and emission wavelength at 527 nm were plot against concentration of benzo[a]anthracene from 0 to 2 ppm as shown in Figure 82.

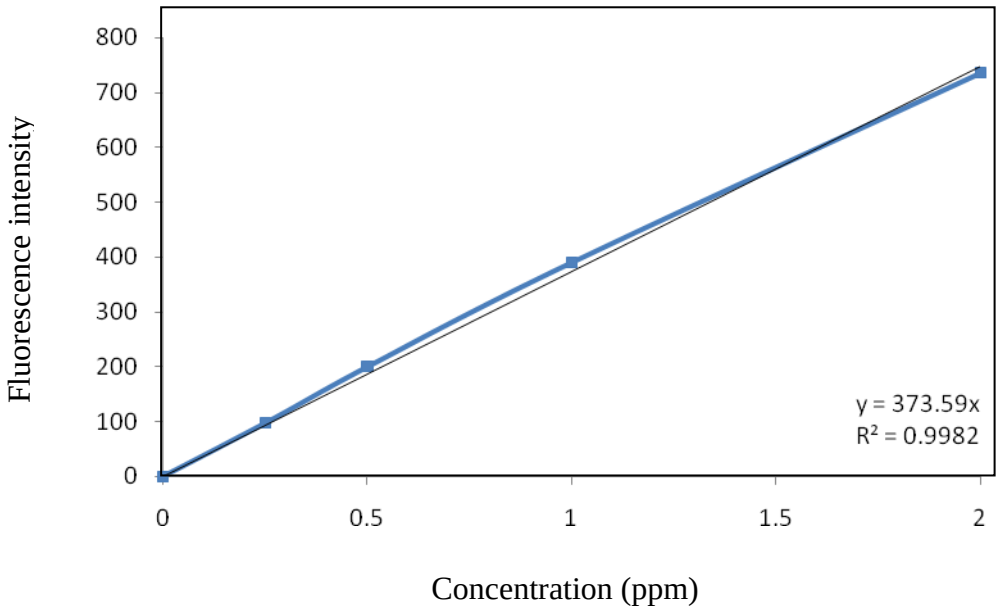

Figure 82 Calibration curve of benzo[a]anthracene at concentration from 0-2 ppm.

3.4 Photodegradation of benzo[a]anthracene

The fluorescence of benzo[a]anthracene after degraded in each 30 minutes interval under visible light were quantified by fluorescene spectroscopy at excitation wavelength at 287 nm and emission wavelength at 527 nm, excitation slit width 10 nm and emission slit width 2.5 nm with scanning rate 1000 nm/min were used.

The photodegradation results showed in Figure 83 to 86. Figure 83 presented the photodegradation of benzo[a]anthracene under visible light for 4.5 hours without catalyst under optimized condition, 125 ml of 20 ppm benzo[a]anthracene solution.

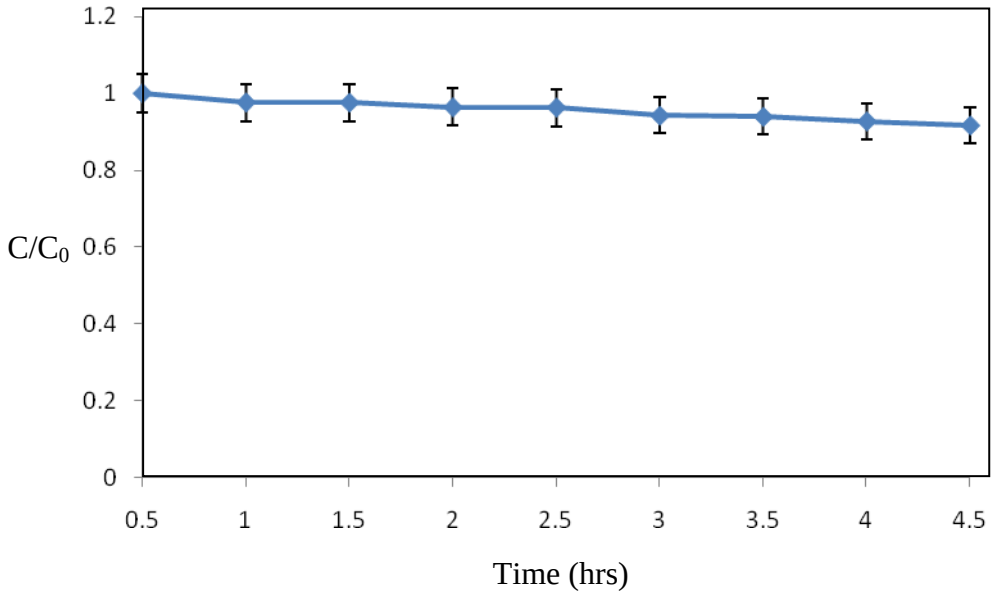

Figure 83 Photodegradation of 20 ppm benzo[a]anthracene without catalyst.

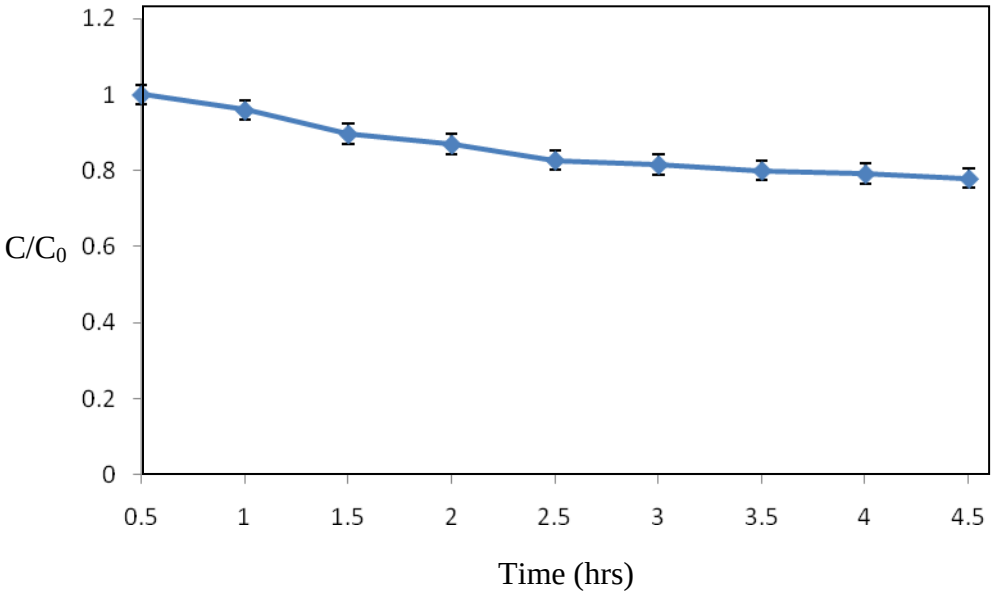

Figure 84 Photodegradation of 20 ppm benzo[a]anthracene using 0.1 g of P-25 TiO_2.

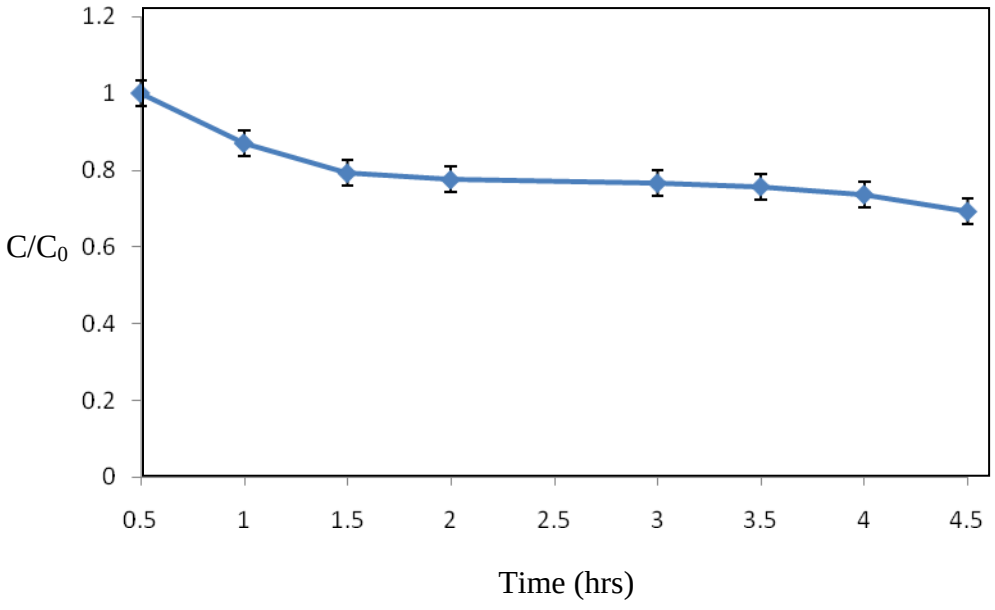

Figure 85 Photodegradation of 20 ppm benzo[a]anthracene using 0.1 g of 13.57 %wt Sm doped TiO_2 catalyst calcined at 500^{o}C.

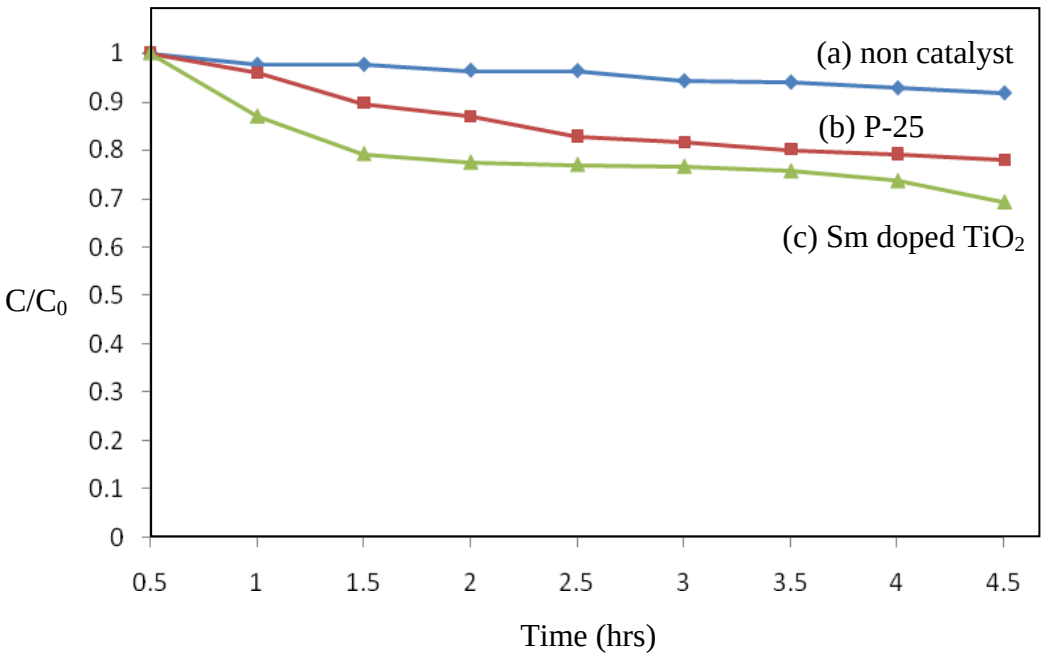

Figure 86 Photodegradation of 20 ppm benzo[a]anthracene (a) without catalyst, (b) using 0.1 g of P-25 TiO_2 and (c) using 0.1 g of 13.57 %wt Sm doped TiO_2 catalysts calcined at 500^oC.

The results indicated that Sm doped TiO_2 catalyst was more effective for degradation of benzo[a]anthracene at optimized condition. In case of Sm doped catalyst, the degradation rate of benzo[a]anthracene was faster than in non-catalyst condition and also using P-25 TiO_2. To propose the rate of degradation, the graph of log concentration versus time was plotted. The calculation was similar to degradation of phenanthrene as discussed before. The degradation of benzo[a]anthracene was the first order reaction. The rate constant, % conversion and half life are shown in Table 19.

With the same calculation method which mentioned before, the rate constant of photocatalytic degradation of phenanthrene using Sm doped TiO_2 with various amount of Sm are shown in Table 19.

Table 19 Rate constant and half life of photodegradation of 20 ppm benzo[a]anthracene without catalyst and using 0.1 g of P-25 TiO_2 and 0.1 g of 13.57 %wt Sm doped TiO_2.

Catalyst	% Conversion	R^2	Rate constant (hrs^{-1})	$t_{1/2}$ (hrs)
Non catalyst	8.23	0.969	0.0198	34.99
P-25 TiO_2	22.04	0.928	0.0619	11.19
Sm doped TiO_2	30.74	0.794	0.0691	10.03

It can notice that the rate constant of benzo[a]anthracene was lower than phenanthrene. This due to the structure of four aromatic rings of benzo[a]anthracene which more difficult to brake the C-C bond than in three rings of phenanthrene. Also half life of benzo[a]anthracene was much longer than phenanthrene, 229 - 1400 days and 16 - 200 days in soil and atmosphere respectively (Sanghvi, 2005). As a results, the degradation rate of benzo[a]anthracene was lower than phenanthrene. However, same to degradation of phenanthrene, Sm doped TiO_2 was more effective catalyst for degrade benzo[a]anthracene under visible light.

3.6 Photodegradation of phenol

The absorbance of phenol after the degradation in each 30 minutes interval under visible light were quantified by UV-Vis spectroscopy at 270 nm which was the maximum wavelength. The degradation was run under the same condition of phenanthrene and benzo[a]anthracene. Figure 87 to 90 showed the absorbance of phenol after degraded with Sm doped TiO_2 catalyst within 4 hours. The concentration of phenol remained more than 80% after the degradation with catalyst within 4 hours. This result showed that in case of phenol, the degradation rate is much lower than phenanthrene and also benzo[a]anthracene. This may due to the structure of phenol was only one aromatic ring which was more stable, then it was more difficult to degrade compared with phenanthrene and benzo[a]anthracene. The degradation rate of phenol via preparing 13.57% Sm doped TiO_2 catalyst calcined at 500^oC, which the most effective catalyst to degrade phenanthrene, has higher rate constant compared to P-25 and undoped TiO_2. The reason was the same as previously mentioned. With the same calculation method which mentioned before, the rate constant of photocatalytic degradation of phenol using P-25, undoped and Sm doped TiO_2 are shown in Table 20.

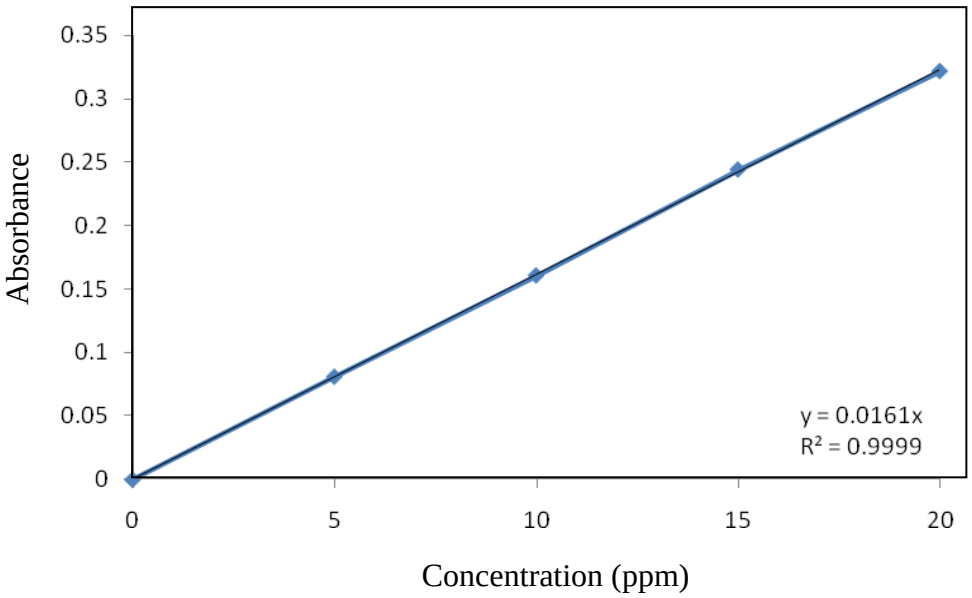

Figure 87 Calibration curve of phenol at concentration from 0-20 ppm.

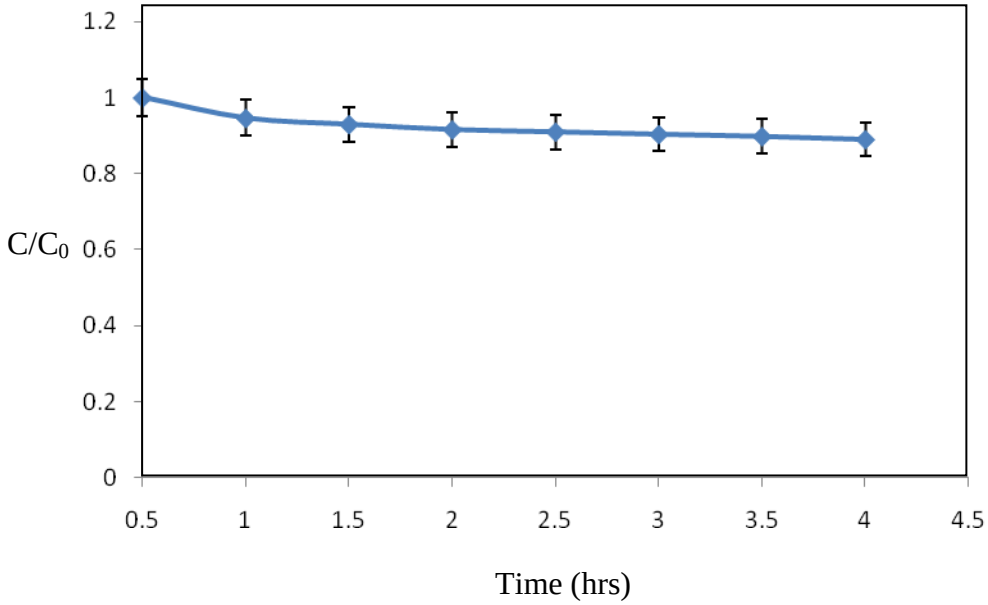

Figure 88 The photodegradation of 20 ppm phenol using 0.1 g of P-25 TiO_2.

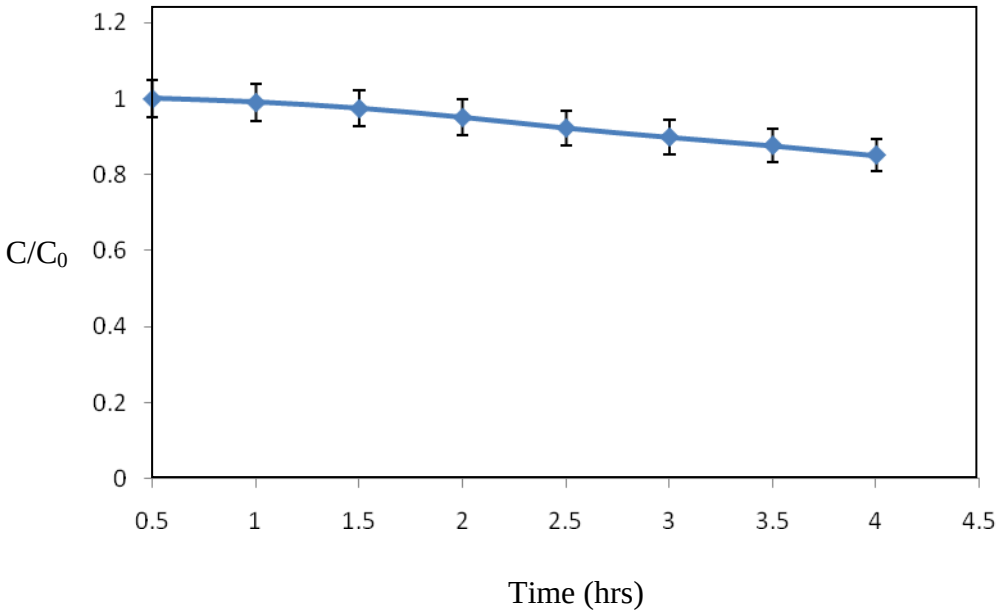

Figure 89 The photodegradation of 20 ppm phenol using 0.1 g of undoped TiO_2.

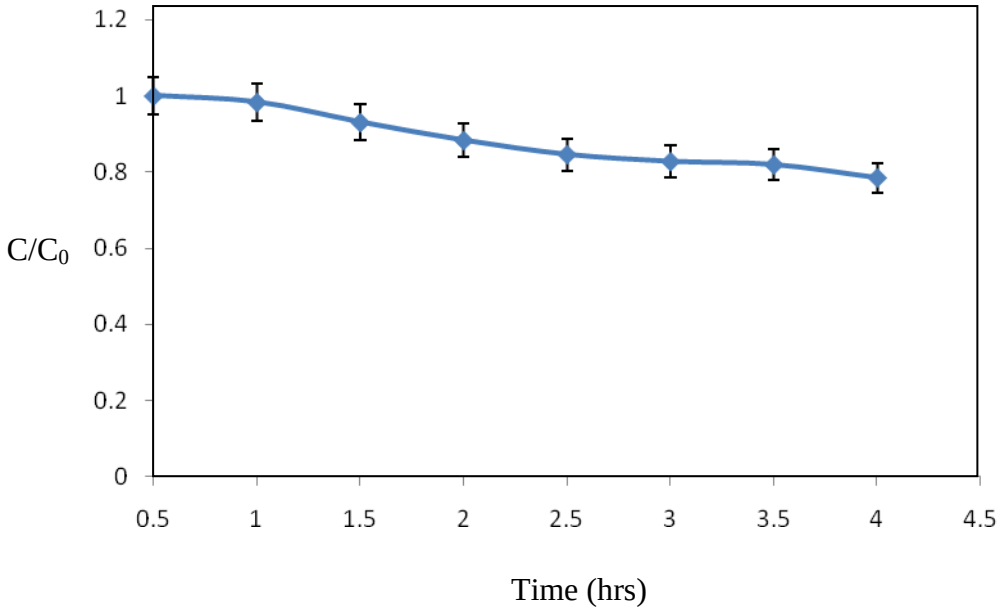

Figure 90 The photodegradation of 20 ppm phenol using 0.1 g of 13.57 %wt Sm doped TiO_2.

\

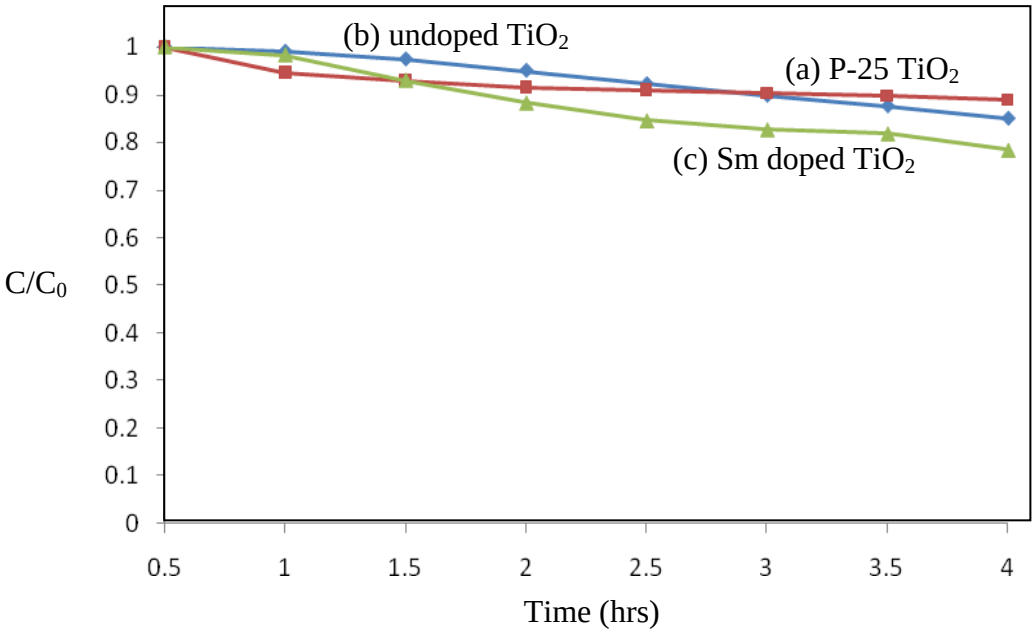

Figure 91 The photodegradation of 20 ppm phenol using (a) 0.1 g of P-25 TiO_2, (b) 0.1 g of undoped TiO_2 and (c) 0.1 g of 13.57%wt Sm doped TiO_2.

The reason that degradation rate of phenol was lower than phenanthrene and benzo[a]anthracene was due to the structure of these compounds. Phenol has one aromatic ring which presence less strain of C-C bond within the structure compared with phenanthrene which has three aromatic rings that bond distortion would more easily occur. Therefore, the degradation of phenanthrene was faster than phenol.

Table 20 Rate constant and half life of photodegradation of 20 ppm phenol using 0.1 g of P-25 TiO_2, 0.1 g of undoped TiO_2 and 0.1 g of 13.57 %wt Sm doped TiO_2.

Catalyst	% Conversion	R^2	Rate constant (hrs^{-1})	$t_{1/2}$ (hrs)
P-25 TiO_2	11.01	0.823	0.0279	24.87
Undoped TiO_2	14.90	0.985	0.0479	14.47
Sm doped TiO_2	21.57	0.971	0.0716	9.68

The proposed degradation mechanism of phenanthrene using catalyst compared with hydrothermal degradation showed in Figure 92 and 93. The structure of two main intermediates, bis(2-ethylhexyl)benzene-1,2-dicarboxylate and dimethyl-4-methyl-1,2-benzene dicarboxylate, from the photodegradation of phenanthrene using N-doped TiO_2 were detected by Sirisaksoontorn *et al*. (2009) are shown in Figure 92. The proposed photocatalytic degradation mechanism of phenanthrene involved the oxidation reaction by OH radicals, followed by ring opening of phenanthrene was studied by Wen *et at.* (2002) as shown in Figure 93.

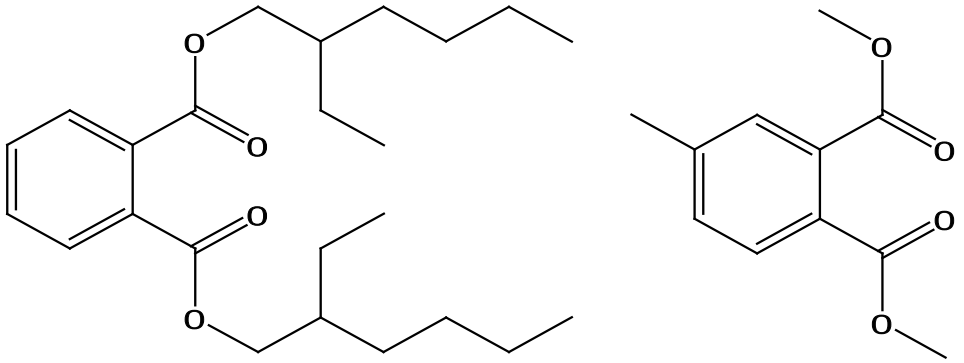

(a) (b)

Figure 92 The chemical structures of two detected intermediate products;
(a) bis(2-ethylhexyl)benzene-1,2-dicarboxylate and
(b) dimethyl-4-methyl-1,2-benzene dicarboxylate.

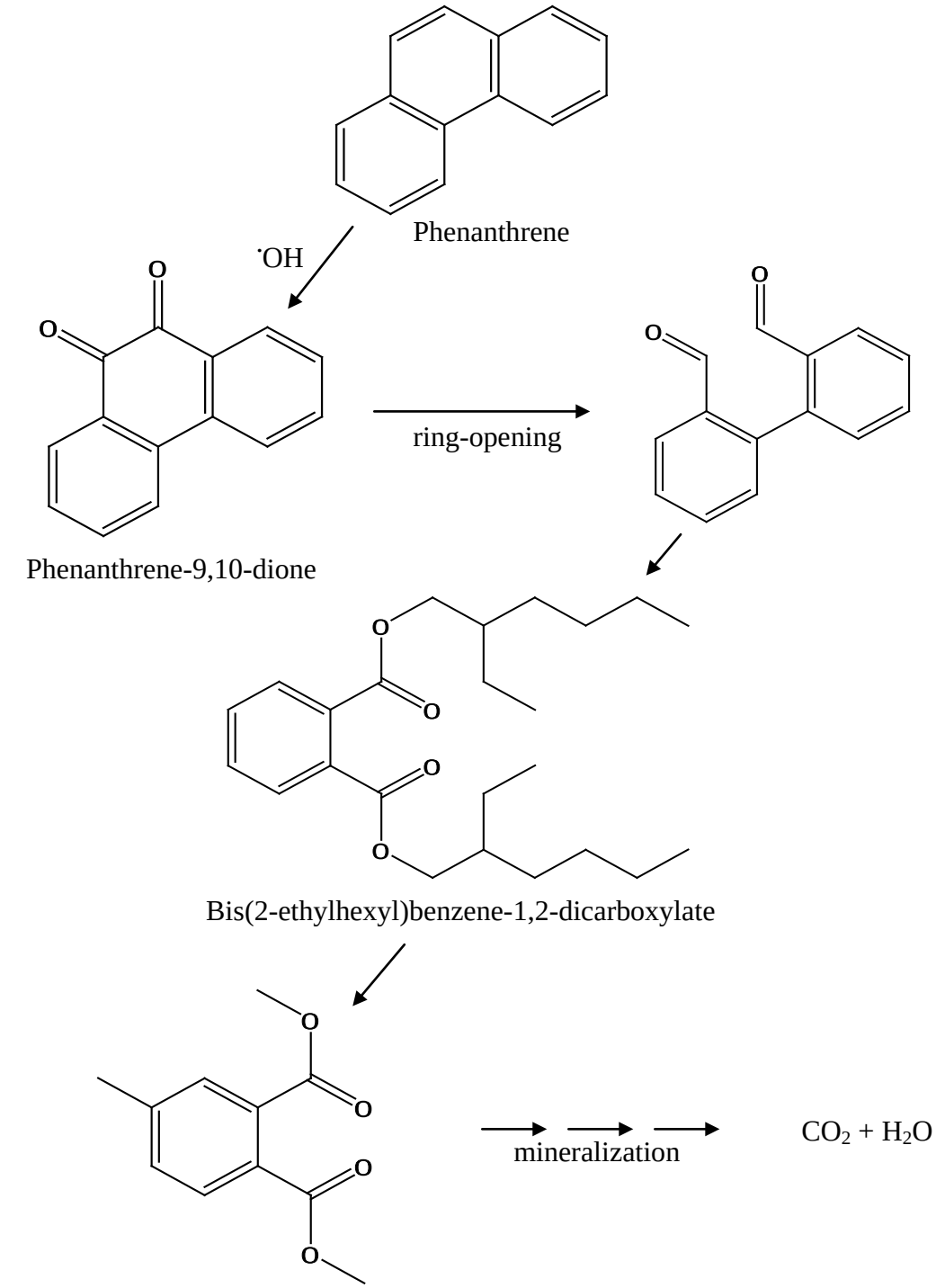

Figure 93 Proposed mechanism of photocatalytic degradation of phenanthrene using Sm doped TiO_2.

Source: Sirisaksoontorn *et al*. (2009)

CONCLUSION

The Sm doped TiO_2 were prepared with the variation of synthesis conditions by sol-gel method. With different synthesis conditions, the calcination temperature had effected on the crystal structure of TiO_2. As increase temperature, crystallite size of TiO_2 was increased, and transformation from anatase to rutile phase was occurred then the activity of TiO_2 catalyst could be decreased. The characterization results showed that Sm doping can improve the photocatalytic properties, decrease particle size and phase transformation. All Sm ions dispersed homogeneity in TiO_2 structure and possessed in anatase hole. Amount of Sm doped had effected to crystallite size and ratio of anatase to rutile in catalyst structure. Higher amount of Sm doped gave smaller crystallite size and decreased in percentage of anatase. The Sm ion could hinder the increase of crystallite size during calcinations and also inhibitted the phase transformation which occurred at high temperature.

From the photocatalytic activity results, Sm doped TiO_2 provided the highest %conversion and rate constant of photodegadation of phenanthrene, benzo[a]anthracene and phenol under visible light. The rate constants in photocatalytic degradation of phenanthrene for Sm doped TiO_2 was 0.2819 h^{-1}, undoped TiO_2 was 0.1608 h^{-1} and P-25 TiO_2 was 0.1891 h^{-1}. The rate constants in photocatalytic degradation of benzo[a]anthracene for Sm doped TiO_2 was 0.0691 h^{-1} and P-25 TiO_2 was 0.0619 h^{-1}. The rate constants in photocatalytic degradation of phenol for Sm doped TiO_2 was 0.0716 h^{-1}, undoped TiO_2 was 0.0479 h^{-1} and P-25 TiO_2 was 0.0279 h^{-1}. From these results, rate constants in photocatalytic degradation of all compounds using Sm doped TiO_2 are higher than using undoped TiO_2 and also P-25 TiO_2. Indicated that Sm can extend the photoresponse to visible light of TiO_2.

Sm doped TiO_2 catalyst prepared by sol-gel technique could improve the photocatalytic activity of PAHs such as phenanthrene and benzo[a]anthracene over undoped TiO_2. With smaller crystallite size, higher surface area as a consequence and extended photoresponse to visible light improved as more efficient photocatalyst.

LITERATURE CITED

Abhijeet. 2008. **Raman effect.** Raman scattering: Stokes and anti-Stokes. Available source: http://scisoft.blogspot.com/2008/07/raman-effect.html, Feb 23, 2008.

Arena network. 1995. **Mechanism of TiO_2 Photomineralisation.** Available source: http://www.arenanetwork.org/About/AboutUs.aspx, May 3, 2009.

Carp, O., C.L. Huisman and A. Reller. 2004. Photoinduced reactivity of titanium dioxide. **Prog. Solid State Chem.** 32: 33-177.

Callahan, M.A., M.W. Slimak, N.W. Gabelc, I.P. May, C.F. Fowler, J.R. Freed, P. Jennings, R.L. Durfee, F.C. Whitmore, B. Maestri, W.R. Mabey, B.R. Holt, and C.Gould. 1979. **Water-Related Environmental Fate of 129 Priority Pollutants.** US Environmental Protection Agency, Washington, DC. EPA-440/4-79-029.

Du, H., H.Chen, B.K. Moom, J.H. Shin and S.W. Lee. 2004. Effect of plasma spraying condition on deposition efficiency, microstructure and microhardness of TiO_2 coating. **Advances in Technology of Materials and Materials Processing Journal.** 6 (2): 152-157.

Garcia, T., B. Solsona and S.H. Taylor. 2006. Naphthalene total oxidation over metal oxide catalysts. **Appl. Catal. B: Environ.** 66: 92-99.

Gnaser, H., A. Orendorz, A. Brodyanski, J. Losch, L.H. Bai, Z.H. Chen, Y.K. Le and C. Ziegler. 2007. Phase transformation and particle growth in nanocrystalline anatase TiO_2 films analyzed by X-ray diffraction and Raman spectroscopy. **Surf. Sci.** 601: 4390-4394.

Hoffmann, M.R., S.T. Martin, W. Choi, and D.W. Bahnemannt. 1995. Environmental applications of semiconductor photocatalysis. **Chem. Rev.** 95: 69-96.

Iliev, V., D. Tomova, L. Bilyarska, A. Eliyas and L. Petrov. 2006. Photocatalytic properties of TiO_2 modified with platinum and silver nanoparticles in the degradation of oxalic acid in aqueous solution. **Appl. Catal. B: Environ.** 63: 266-271.

Instituto de Ciencia de Materiales de Madrid. 2008. **SEM of a titania microparticle sample**. Nano photonic gallery. Available source: http://reilucis.icmm.csic.es, March 27, 2009.

Ireland, J.C., B.D. Davila and H. Moreno. 1995. Heterogeneous photocatalytic decomposition of polyaromatic hydrocarbons over titanium dioxide. **Chemosphere.** 30(5): 965-984.

Kelf, T.A. 2005. **Surface Enhanced Raman Spectroscopy.** Available source: http://www.timkelf.com/Research.html, April 8, 09.

Krumeich, F. 2008. **Electron microscopy.** Bragg's law of diffraction. Available source: http://www.microscopy.ethz.ch/bragg.htm, Feb 23, 2009

Kumar, K. P. 1995. Growth of rutile crystallites during the initial stage of anatase-to-rutile transformation in pure titania and titania-alumina nanocomposites. **Scr. Metall. Mater.** 32(6): 873-877.

Lange, N.A. 1956. **Handbook of Chemistry.** 9th ed. Handbook Publisher, Ohio.

Li, F.B., X.Z. Li and M.F. Hou. 2003. Photocatalytic degradation of 2-mercaptobenzothiazole in aqueous La^{3+} - TiO_2 suspension for odor control. **Appl. Catal. B: Environ.** 48:185-194.

Lin, H.F. and K.T. Valsaraj. 2003. A titania thin film annular photocatalytic reactor for the degradation of polycyclic aromatic hydrocarbons in dilute water streams. **J. Hazard. Mater. B.** 99: 203-219.

Liqiang, J., S. Xiaojun, X. Baifu, W. Baiqi, C. Weimin and F. Honggang. 2004. The preparation and characterization of La doped TiO_2 nanoparticles and their photocatalytic activity. **J. Solid State Chem.** 177: 3375–3382.

Liu, T., Y. Zhang, H. Shao and X. Li. 2003. Synthesis and Characteristics of Sm_2O_3 and Nd_2O_3 nanoparticles. **Langmuir.** 19 (18): 7569-7572.

Miller, J.S. and D. Olejnik. 2001. Photolysis of polycyclic aromatic hydrocarbons in water. **Wat. Res.** 35: 233-243.

Mills, A. and S.L. Hunte. 1997. An overview of semiconductor photocatalysis. **J. Photochem. Photobiol. A: Chem.** 108: 1-35.

Muggli, D.S. and L. Ding. 2001. Photocatalytic performance of sulfated TiO_2 and Degussa P-25 TiO_2 during oxidation of organics. **Appl. Catal. B: Environ.** 32: 181-194.

Nagpal, N. K. 1993. **PAHs and their characteristics.** Structure of PAHs. Available source: http://www.scielo.br 20pah, Jan 16, 2009.

Pal, B. and M. Sharon. 2000. Photodegradation of polyaromatic hydrocarbons over thin film of TiO_2 nanoparticles; a study of intermediate photoproducts. **J. Mol. Catal. A: Chem.** 160: 453-460.

Patterson, A.L. 1939. The Scherrer formula for X-Ray particle size determination. **Phys. Rev.** 56: 978-982.

Ravindraa, K., R. Sokhia and R.V. Griekenb. 2008. Atmospheric polycyclic aromatic hydrocarbons: Source attribution, emission factors and regulation. **Atmos. Environ.** 42: 2895-2921.

Saif, M. 2007. Titanium dioxide nanomaterial doped with trivalent lanthanide ions of Tb, Eu and Sm: Preparation, charavterization and potential applications. **Inorg. Chim. Acta.** 360: 2863-2874.

Sanghvi, S. 2005. Bioremediation of polycyclic aromatic hydrocarbon contamination using Mycobacterium vanbaalenii. **MMG 445 eJournal.** 1: 1-7.

Sano, T., E. Puzenat, C. Guillard, C. Geantet and S. Matsuzawa. 2008. Degradation of C_2H_2 with modified TiO_2 photocatalysts under visible light irradiation. **J. Mol. Catal. A: Chem.** 284: 127-133.

Sariyusriati. 2008. **Sol Gel Technology**. Available source: http://www.chemat.com, Feb 23, 2009.

Sirisaksoontorn, W. and A. Songsasen. 2009. Photodegradation of phenanthrene by N-doped TiO_2 photocatalyst. **J. Environ. Sci. Health, Part A.** 44 (9).

Smyth, J. 2009. **Mineral Structure and Property Data.** TiO_2 Group. Available source: http://ruby.colorado.edu/%7Esmyth/min/tio2.html, Feb 23, 2009.

University of Bristol. 2000. **Film Characterisation Techniques.** Scanning Electron Microscopy (SEM). Available source: http://www.chm.bris.ac.uk/pt/diamond/stuthesis/chapter2.htm, Jan 16, 2009.

Wang, W. and J.P. Lewis. 2006. Second-generation photocatalytic materials: anion-doped TiO_2. **J. Phys.: Condens. Matter.** 18: 421-434.

Wen, S., J. Zhao, G. Sheng, J. Fu, P. Peng. 2002. Photocatalytic reactions of phenanthrene at TiO_2/water interfaces. **Chemosphere.** 46 (6): 871-877.

Wikimedia commons. 2008. **TEM ray diagram.** Available source: http://www.uiowa.edutem diagram, April 8, 09.

Winter, M. J. 1993. **The periodic table**. Titanium. Available source: http://www.webelements.com, Feb 23, 2009.

_____ M. J. 1993. **The periodic table**. Samarium. Available source: http://www.webelements.com/samarium/atom_sizes.html, Feb 23, 2009.

Wikipedia. 2009. **Development of the Bravais lattices.** Bravais lattice. Available source: http://en.wikipedia.org/wiki/Bravais_lattice, April 8, 2009.

Xiao, Q., Z. Si, J. Zhang, C. Xiao and Z. Yu. 2007. Effects of Samarium dopant on photocataytic activity of TiO_2 nanocrystallite for methylene blue degradation. **J. Matter. Sci.** 42: 9194-9199.

Xie, Y. and C. Yuan. 2004. Photocatalysis of neodymium ion modified TiO_2 sol under visible light irradiation. **Surf. Sci.** 221: 17-24.

_____ _____ and X. Lib. 2005. Photosensitized and photocatalyzed degradation of azo dye using Ln^{n+}- TiO_2 sol in aqueous solution under visible light irradiation. **J. Mater. Sci. Eng. B**. 117: 325-333.

Yan, Q.Z., X.T. Sua, Z.Y. Huangb and C.C. Gea. 2006. Sol–gel auto-igniting synthesis and structural property of cerium-doped titanium dioxide nanosized powders. **J. Eur. Ceram. Soc.** 26: 915–921.

Yates, J.T., A.L. Linsebigler and G. Lu. 1995. Photocatalysis on TiO_2 Surfaces: Principles, Mechanisms, and Selected Results. **Chem. Rev.** 95: 735-758.

Zhang, Y., H. Xu, Y. Xu, H. Zhang and Y. Wang. 2005. The effect of lanthanide on the degradation of RB in nanocrystalline Ln/TiO_2 aqueous solution. **J. Photochem. Photobiol. A: Chem.** 170: 279-285.

APPENDICES

APPENDIX A

Calculation of anatase and rutile phase composition by the Liqiang's equation.

The percentage of anatase (%X_A) and rutile (%X_R) were calculated from Liqiang's equation as follows:

$$\%X_A = \frac{100}{(1+1.265\frac{I_R}{I_A})}$$

and $$\%X_B = 100 - \%X_A$$

where $\%X_A$ is the percentage of anatase phase in TiO_2

$\%X_B$ is the percentage of rutile phase in TiO_2

I_A is the intensity anatase peak at 2Θ = 25.25

I_R is the intensity rutile peak at 2Θ = 27.42

An example of finding all constants involved in the Liqiang's equation.

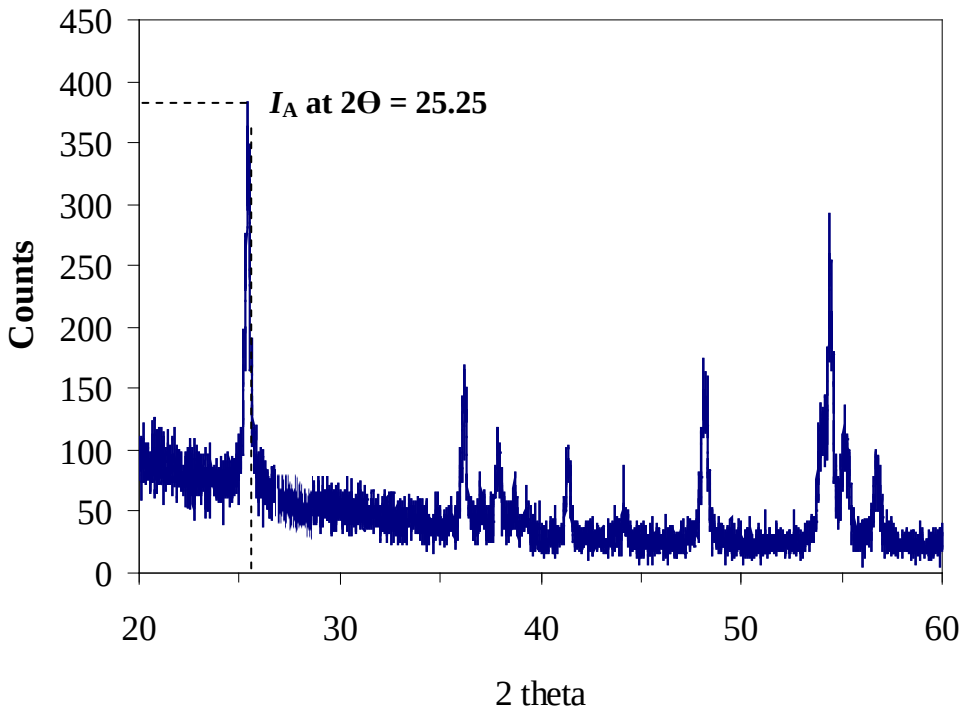

Appendix Figure A1 The phase composition calculation of undoped TiO_2 calcined at 500°C.

APPENDIX B

Calculation of crystallite size from Sherrer's formula.

The crystallite size was calculated applying the Sherrer's equation (Patterson, 1939) as follows:

$$L = \frac{K\lambda}{\beta \cos\theta}$$

where L is crystallite size (nm)

K is a constant whose value is approximately 0.9

λ is the wavelength of the X-ray radiation source (0.1542 nm for Cu Kα)

β is the linewidth at half-maximum height (radians)

θ is the Bragg's angle at the position of the maximum peak

An example of finding all constants involved in the Sherrer's equation.

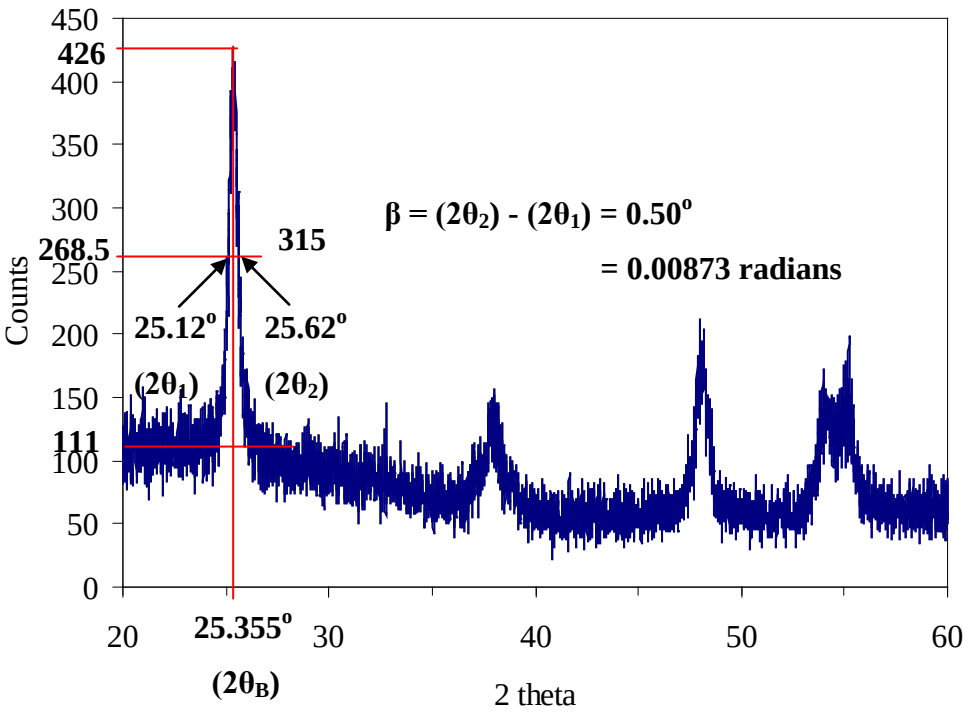

Appendix Figure B1 Crystallite size calculation of undoped TiO_2 calcined at 500°C.

APPENDIX C

Calculation of unit cell parameters.

Unit cell parameters of Tetragonal structure (a, c and unit cell volume) were calculated from equation 1 as follows:

$$\frac{1}{d^2} = \frac{h^2 + k^2}{a^2} + \frac{l^2}{c^2} \qquad (1)$$

and unit cell volume calculated from equation as follows:

$$V = a^2c \qquad (2)$$

where d : the distance between two lattice planes (nm) which calculated from Bragg's law as follows:

$$n\lambda = 2d\sin\Theta \qquad (3)$$

h, k, l : Miller indices which is characteristic value from each 2Θ

V : unit cell volume (nm^3)

a, c : unit cell side (nm)

n : the integer called order of the reflection (n=1)

λ : the wavelength of the X-rays (0.1542 nm for Cu Kα)

Θ : the angle between the incident X-rays and the normal to the reflecting lattice plane

An example to calculated unit cell parameters was showed below

Sample of 13.57 %wt Sm doped TiO_2 gave anatase peak at $2\Theta = 25.35^o$ and 37.87^o which corresponded to Miller indices (h l k) = 101 and 004 respectively. Place each value in equation (3):

$$0.1542 = 2d_{101}\sin(25.35/2)$$

$$d_{101} = 0.3514 \text{ nm}$$

and

$$0.1542 = 2d_{004}\sin(37.87/2)$$

$$d_{004} = 0.2376 \text{ nm}$$

from placing each d values in equation (1) will give

$$a = 0.3781 \text{ nm and } c = 0.9528 \text{ nm}$$

then calculated unit cell volume (V) from equation (2)

$$\begin{aligned} V &= a^2c \\ &= (0.3781)^2(0.9528) \\ &= 0.1362 \text{ nm}^3 \end{aligned}$$

APPENDIX D

Calculation of absorption edge and energy gap from UV-Vis/DRS data.

Band gap or energy gap (E_g) was calculated from equation as follows (Fernandes et al., 2005):

$$E_g = \frac{1239.8}{\lambda} \quad (1)$$

where E_g is band gap energy (eV)

λ is wavelength at absorption edge (nm)

Absorption edge derived from extrapolated the cross line on UV-Vis/DRS spectrum as showed below:

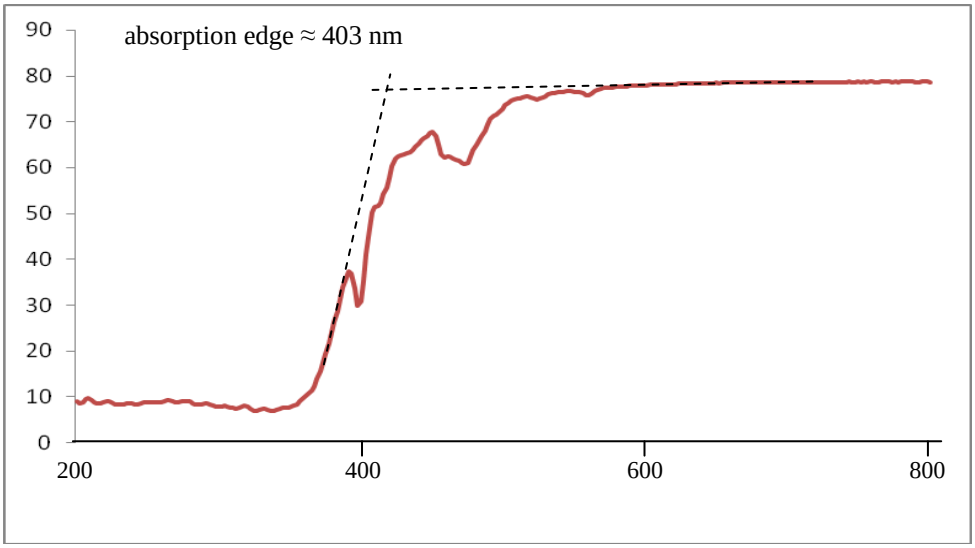

Appendix Figure D1 UV-Vis/DRS spectrum of 33.58 %wt Sm doped TiO_2 catalyst calcined at 500 ^oC.

Then E_g can be calculated from placing the estimated absorption edge value in equation (1)

$$E_g = \frac{1239.8}{403}$$

$$= 3.08 \text{ eV}$$

APPENDIX E

The full data of % weight Sm in Sm doped TiO_2 catalysts from SEM/EDX.

Appendix Table E1 Weight percentage of Sm from SEM/EDX in prepared Sm doped TiO_2 catalysts.

Catalyst	%wt of Sm			Average %wt of Sm
	1	2	3	
13.57%wt Sm doped TiO_2	14.53	14.36	12.01	13.63
23.90%wt Sm doped TiO_2	29.86	24.65	30.42	28.31
38.58%wt Sm doped TiO_2	37.16	34.62	34.72	35.50
55.68%wt Sm doped TiO_2	50.46	50.91	50.70	50.69

APPENDIX F

The full data of particle size from TEM.

Appendix Table F1 Full data of particle size of P-25 and all prepared TiO_2 catalysts.

P-25	13.57 %wt Sm at 500°C	13.57 %wt Sm at 600°C	13.57 %wt Sm at 700°C	23.90 %wt Sm at 500°C	55.68 %wt Sm at 500°C
75.57	9.96	12.66	17.10	12.27	9.24
64.71	8.53	11.28	17.41	9.35	12.60
39.77	10.81	13.33	17.46	12.18	15.07
53.57	8.95	11.30	17.38	10.56	9.32
36.59	10.58	15.48	13.82	14.24	8.02
21.12	10.27	14.92	16.30	9.11	9.31
48.88	12.83	14.42	18.02	7.78	12.27
15.34	11.67	12.52	17.35	10.34	12.78
48.02	10.96	11.32	20.06	10.38	14.74
27.21	7.94	13.18	21.90	7.57	9.91
39.48	9.60	14.48	13.00	23.59	10.02
28.68	11.97	14.01	14.71	19.39	9.39
24.89	7.72	12.50	11.59	21.35	
24.89	9.53	17.58	13.56	23.46	
31.16	12.24	10.72	13.52	23.64	
144.57	11.06	12.79	17.20	24.73	
180.38	10.34	18.67	13.11	19.72	
67.96	12.70	15.34	16.70		
56.84	9.84	13.93	17.53		
80.05	8.97	10.33	15.88		
49.99		13.88	15.19		
31.45		10.08	15.74		
27.45		12.14	10.58		
43.49		12.85	13.06		
32.21		9.38	13.87		
30.50		14.60	12.38		
41.38		12.21			

APPENDIX G

Calculation of % conversion, rate constant and half life in photodegradation.

The % conversion of each samples in photodegradation were calculated using equation as follows:

$$\% \text{ conversion} = \frac{(\text{initial concentration} - \text{final concentration})}{\text{initial concentration}} \times 100$$

To determined the order of photodegradation reaction, log concentration versus time was plotted to determined the order of reaction and calculated the rate constant (k) from slope extrapolation, for example:

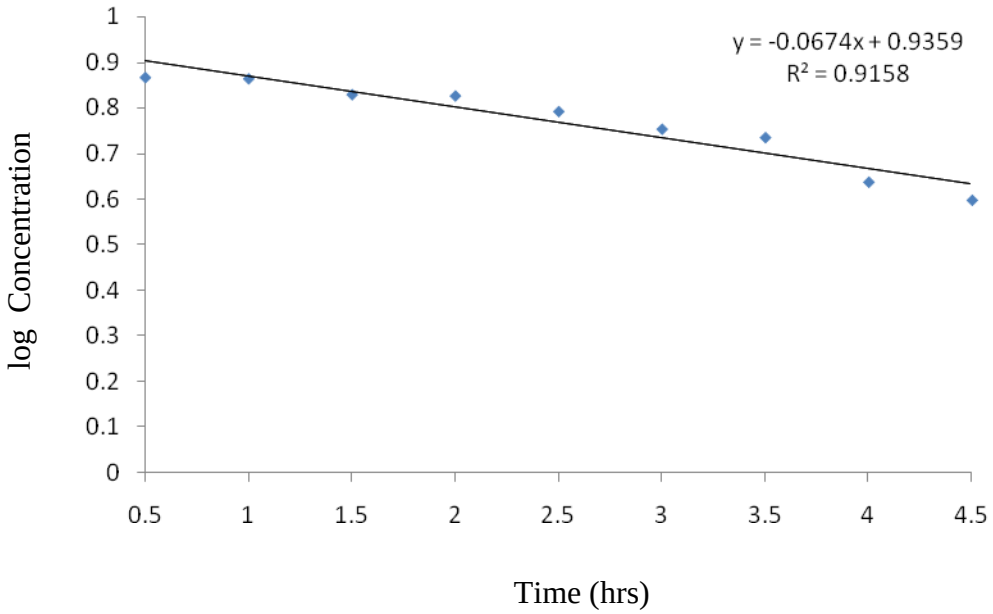

Appendix Figure G1 Plotted of log concentration versus time to determine the rate constant using prepared 13.57 %wt Sm doped TiO_2 catalyst.

.

Half life was calculated from rate constant using equation as follows:

$$t_{1/2} = \frac{0.693}{k}$$

where $t_{1/2}$ is half life (hrs)

k is rate constant (hrs^{-1})

APPENDIX H

Full data from photodegradation of phenanthrene, benzo[a]anthracene and phenol.

Appendix Table H1 Raw data of the photodegradation of 20 ppm phenanthrene without catalyst.

Degrading time	Absorbance at λ_{max} 251 nm			Concentration* (ppm)			Relative concentration (C/C_o)				
(hrs)	Abs_1	Abs_2	Abs_3	C_1	C_2	C_3	C_1/C_o	C_2/C_o	C_3/C_o	$(C/C_o)_{ave}$	Std $_{(C/Co)}$
0.5	1.3555	1.2843	1.3673	6.8047	6.4472	6.8639	1	1	1	1	2.20431E-08
1	1.3553	1.2839	1.3601	6.8037	6.4452	6.8278	0.9998	0.9996	0.9944	0.9980	0.002375
1.5	1.3426	1.2743	1.3546	6.7399	6.3970	6.8002	0.9904	0.9922	0.9907	0.9911	0.000767
2	1.3416	1.2731	1.3504	6.7349	6.3910	6.7791	0.9897	0.9912	0.9876	0.9895	0.001491
2.5	1.3337	1.2549	1.3421	6.6952	6.2996	6.7374	0.9839	0.9771	0.9815	0.9808	0.002824
3	1.3332	1.2502	1.3394	6.6927	6.2761	6.7238	0.9835	0.9734	0.9795	0.9788	0.004155
3.5	1.3311	1.2448	1.3252	6.6822	6.2489	6.6526	0.9819	0.9692	0.9692	0.9734	0.006021
4	1.3165	1.2215	1.3118	6.6089	6.1320	6.5853	0.971228	0.951102	0.959409	0.96058	0.008258
4.5	1.3086	1.2122	1.3037	6.5692	6.0853	6.54467	0.9654	0.94386	0.953485	0.954249	0.008810

* concentrations were converted from absorbance by using linear calibration of phenanthrene .

Appendix Table H2 Raw data of the photodegradation of 20 ppm phenanthrene using 0.1 g of P-25 TiO_2.

Degrading time	Absorbance at λ_{max} 251 nm			Concentration (ppm)			Relative concentration (C/C_o)				
(hrs)	Abs_1	Abs_2	Abs_3	C_1	C_2	C_3	C_1/C_o	C_2/C_o	C_3/C_o	$(C/C_o)_{ave}$	Std $_{(C/Co)}$
0.5	1.560632	1.365357	1.700033	7.8345	6.8542	8.5343	1	1	1	1	0
1	1.529576	1.072215	1.261084	7.678593	5.382603	6.330744	0.7853	0.9801	0.7418	0.8357	0.126903
1.5	1.460908	1.014733	1.229294	7.333875	5.094041	6.171152	0.7432	0.9361	0.7231	0.8008	0.117603
2	1.445458	0.996983	1.223173	7.256314	5.004937	6.140429	0.7302	0.9262	0.7195	0.7919	0.116373
2.5	1.347918	0.953155	1.162652	6.766658	4.784917	5.836608	0.6981	0.8637	0.6839	0.7485	0.099961
3	1.119129	0.947558	1.176423	5.61812	4.756815	5.905736	0.694	0.7171	0.692	0.7010	0.013950
3.5	0.873642	0.868776	1.074931	4.385753	4.361327	5.396238	0.6363	0.5598	0.6323	0.6094	0.043059
4	0.841181	0.652504	0.845596	4.222796	3.275622	4.244961	0.4779	0.539	0.4974	0.5047	0.031209
4.5	0.775166	0.560889	0.780995	3.891396	2.815705	3.920657	0.4108	0.4967	0.4594	0.4556	0.043074

Appendix Table H3 Raw data of the photodegradation of 20 ppm phenanthrene using 0.1 g of undoped TiO_2.

Degrading time	Absorbance at λ_{max} 251 nm			Concentration (ppm)			Relative concentration (C/C_o)				
(hrs)	Abs_1	Abs_2	Abs_3	C_1	C_2	C_3	C_1/C_o	C_2/C_o	C_3/C_o	$(C/C_o)_{ave}$	Std $_{(C/Co)}$
0.5	2.100205	1.8267	1.847241	10.5432	9.170181	9.27330	1	1	1	1	0
1	2.050851	1.822882	1.840222	10.29543	9.151015	9.238061	0.9765	0.9979	0.9962	0.9902	0.011898
1.5	2.068912	1.813073	1.829085	10.38611	9.101771	9.182153	0.9851	0.9925	0.9901	0.9892	0.003801
2	1.986122	1.782183	1.751721	9.970493	8.946704	8.793778	0.9456	0.9756	0.9482	0.9565	0.01659
2.5	1.976398	1.763259	1.747254	9.921678	8.851701	8.771355	0.9410	0.9652	0.9458	0.9507	0.01282
3	1.902009	1.639281	1.617022	9.548238	8.22932	8.117578	0.9056	0.8974	0.8753	0.8928	0.015645
3.5	1.44261	1.323773	1.345732	7.242019	6.645447	6.755683	0.6868	0.7246	0.7285	0.7133	0.023003
4	1.362403	1.152903	1.13979	6.839374	5.787668	5.721839	0.6487	0.6311	0.6170	0.6322	0.01587
4.5	1.040904	0.965722	0.892463	5.225421	4.8480	4.480237	0.4956	0.5286	0.4831	0.5024	0.02353

Appendix Table 4 Raw data of the photodegradation of 20 ppm phenanthrene using 0.1 g of 13.57 %wt Sm doped TiO_2 calcined at 450 ^{o}C.

Degrading time	Absorbance at λ_{max} 251 nm			Concentration (ppm)			Relative concentration (C/C_o)				
(hrs)	Abs_1	Abs_2	Abs_3	C_1	C_2	C_3	C_1/C_o	C_2/C_o	C_3/C_o	$(C/C_o)_{ave}$	Std $_{(C/Co)}$
0.5	1.468	1.699813	1.781468	7.369478	8.5332	8.94311	1	1	1	1	0
1	1.429526	1.708232	1.785476	7.176335	8.575464	8.963233	0.9737	1.0049	1.0022	0.9936	0.01726
1.5	1.319864	1.57719	1.648508	6.625823	7.917622	8.275644	0.8990	0.9278	0.9253	0.9174	0.01593
2	1.311044	1.566651	1.637492	6.581546	7.864712	8.220342	0.8930	0.9216	0.9191	0.9113	0.01583
2.5	1.21128	1.447436	1.512887	6.080723	7.266246	7.594814	0.8251	0.8515	0.8492	0.8419	0.0146
3	1.107988	1.324006	1.383875	5.562189	6.646616	6.947166	0.7547	0.7789	0.7768	0.7701	0.01338
3.5	1.06183	1.268849	1.326224	5.330472	6.369723	6.657752	0.7233	0.7464	0.7444	0.7380	0.01282
4	0.847582	1.012831	1.058629	4.254932	5.084491	5.314404	0.5773	0.5958	0.5942	0.5891	0.01023
4.5	0.773514	0.924322	0.966118	3.883102	4.640168	4.84999	0.5269	0.5437	0.5423	0.5376	0.00934

Appendix Table H5 Raw data of the photodegradation of 20 ppm phenanthrene using 0.1 g of 13.57 %wt Sm doped TiO_2 calcined at 500 ^oC.

Degrading time	Absorbance at λ_{max} 251 nm			Concentration (ppm)			Relative concentration (C/C_o)				
(hrs)	Abs_1	Abs_2	Abs_3	C_1	C_2	C_3	C_1/C_o	C_2/C_o	C_3/C_o	$(C/C_o)_{ave}$	Std $_{(C/Co)}$
0.5	1.8790	1.936931	1.728881	9.432731	9.72355	8.67912	1	1	1	1	0
1	1.791758	1.83993	1.584645	8.994769	9.236595	7.955047	0.9535	0.9499	0.9165	0.9400	0.020388
1.5	1.777985	1.823175	1.589915	8.925627	9.152486	7.981501	0.9462	0.9412	0.9196	0.9357	0.014154
2	1.768383	1.817887	1.592152	8.877426	9.125941	7.992732	0.9411	0.9385	0.9209	0.9335	0.01010
2.5	1.714681	1.747887	1.489567	8.607839	8.774532	7.477748	0.9125	0.9024	0.8615	0.8921	0.02698
3	1.382268	1.403326	1.201455	6.939094	7.044809	6.031398	0.7356	0.7245	0.6949	0.7183	0.021039
3.5	1.207258	1.256817	1.035869	6.06053	6.30932	5.200147	0.6425	0.6488	0.5991	0.6301	0.027052
4	0.985667	0.9926	0.778282	4.948128	4.98293	3.907036	0.5245	0.5124	0.4501	0.4957	0.039924
4.5	0.512666	0.555008	0.349405	2.573626	2.786186	1.754041	0.2728	0.2865	0.2020	0.2538	0.045318

Appendix Table H6 Raw data of the photodegradation of 20 ppm phenanthrene using 0.1 g of 13.57 %wt Sm doped TiO_2 calcined at 600 ^oC.

Degrading time	Absorbance at λ_{max} 251 nm			Concentration (ppm)			Relative concentration (C/C_o)				
(hrs)	Abs_1	Abs_2	Abs_3	C_1	C_2	C_3	C_1/C_o	C_2/C_o	C_3/C_o	$(C/C_o)_{ave}$	Std $_{(C/Co)}$
0.5	1.56752	2.189766	1.461196	7.868976	10.9928	7.33532	1	1	1	1	0
1	1.538281	2.142306	1.433689	7.722293	10.75455	7.197236	0.9813	0.9783	0.981175	0.9802	0.0017
1.5	1.433666	1.996613	1.336188	7.197121	10.02316	6.707771	0.9146	0.9117	0.914448	0.9136	0.00158
2	1.410241	1.96399	1.314355	7.079522	9.859385	6.598169	0.8996	0.8968	0.899507	0.8986	0.00155
2.5	1.395224	1.943077	1.30036	7.004139	9.754401	6.52791	0.8900	0.8873	0.889929	0.8891	0.001542
3	1.334959	1.859147	1.244192	6.701599	9.333066	6.245941	0.8516	0.8490	0.851489	0.8507	0.001476
3.5	1.141247	1.589372	1.063651	5.729151	7.978774	5.339612	0.7280	0.7258	0.727932	0.7272	0.001262
4	0.931718	1.297569	0.868368	4.677299	6.513899	4.359278	0.5943	0.5925	0.594286	0.5937	0.00103
4.5	0.870932	1.212914	0.811715	4.372147	6.088924	4.074874	0.5556	0.5539	0.555514	0.5550	0.000963

Appendix Table H7 Raw data of the photodegradation of 20 ppm phenanthrene using 0.1 g of 23.90 %wt Sm doped TiO_2 calcined at 500 ^oC.

Degrading time	Absorbance at λ_{max} 251 nm			Concentration (ppm)			Relative concentration (C/C_o)				
(hrs)	Abs_1	Abs_2	Abs_3	C_1	C_2	C_3	C_1/C_o	C_2/C_o	C_3/C_o	$(C/C_o)_{ave}$	Std $_{(C/Co)}$
0.5	1.32951	1.29670	1.570184	6.674197	6.509538	7.88245	1	1	1	1	0
1	1.301353	1.275605	1.537558	6.532898	6.403641	7.718663	0.9788	0.9837	0.9792	0.9805	0.002725
1.5	1.294366	1.268756	1.529302	6.497821	6.369258	7.677219	0.9735	0.9784	0.9739	0.9753	0.00271
2	1.26442	1.239403	1.493921	6.34749	6.221901	7.499602	0.9510	0.9558	0.9514	0.9527	0.002647
2.5	1.195844	1.172183	1.412897	6.003231	5.884454	7.092858	0.8994	0.9039	0.8998	0.9010	0.002504
3	1.049108	1.028351	1.239528	5.266607	5.162405	6.222532	0.7819	0.7930	0.7894	0.7905	0.002196
3.5	0.971937	0.952707	1.148351	4.879204	4.782666	5.764812	0.7310	0.7347	0.7313	0.7323	0.002035
4	0.793329	0.777633	0.937324	3.982577	3.90378	4.705442	0.5967	0.5997	0.5969	0.5977	0.001661
4.5	0.556447	0.545437	0.657445	2.793407	2.738138	3.300429	0.4185	0.4206	0.4187	0.4192	0.001165

Appendix Table H8 Raw data of the photodegradation of 20 ppm phenanthrene using 0.1 g of 55.68 %wt Sm doped TiO_2 calcined at 500 ^oC.

Degrading time	Absorbance at λ_{max} 251 nm			Concentration (ppm)			Relative concentration (C/C_o)				
(hrs)	Abs_1	Abs_2	Abs_3	C_1	C_2	C_3	C_1/C_o	C_2/C_o	C_3/C_o	$(C/C_o)_{ave}$	Std $_{(C/Co)}$
0.5	1.60610	1.566595	1.702025	8.062249	7.864435	8.544303	1	1	1	1	0
1	1.582186	1.595841	1.657337	7.942703	8.011248	8.319964	0.9851	1.0186	0.9737	0.9925	0.023348
1.5	1.523227	1.536372	1.595577	7.64672	7.712711	8.009923	0.9484	0.9807	0.9374	0.9555	0.022478
2	1.507444	1.520454	1.579045	7.567492	7.632799	7.926932	0.9386	0.9705	0.9277	0.9456	0.022245
2.5	1.476972	1.489718	1.547125	7.414518	7.478505	7.766692	0.9196	0.9509	0.9089	0.9265	0.021795
3	1.414439	1.426645	1.481622	7.100597	7.161874	7.43786	0.8807	0.9106	0.8705	0.8872	0.020872
3.5	1.352104	1.363773	1.416326	6.787672	6.846249	7.110072	0.8419	0.8705	0.8321	0.8481	0.019953
4	1.347141	1.358767	1.411128	6.762758	6.82112	7.083975	0.8388	0.8673	0.8290	0.8450	0.019879
4.5	1.260786	1.271667	1.320671	6.329248	6.383869	6.629874	0.7850	0.8117	0.7759	0.7909	0.018605

Appendix Table H9 Raw data of the photodegradation of 20 ppm benzo[a]anthracene without catalyst.

Degrading time	Fluorescence at λ_{em} 527 nm			Concentration* (ppm)			Relative concentration (C/C_o)				
(hrs)	F_1	F_2	F_3	C_1	C_2	C_3	C_1/C_o	C_2/C_o	C_3/C_o	$(C/C_o)_{ave}$	Std $_{(C/Co)}$
0.5	795.54	794.08	797.09	2.129447	2.125539	2.133596	1	1	1	1	1.55549E-08
1	778.39	775.11	777.09	2.083541	2.074761	2.080061	0.9784	0.9761	0.9749	0.9764	0.001796648
1.5	778.05	774.89	776.87	2.082631	2.074172	2.079472	0.9780	0.9758	0.9746	0.9761	0.001714633
2	767.85	765.84	767.99	2.055328	2.049948	2.055703	0.9651	0.9644	0.9634	0.9643	0.00085237
2.5	767.43	765.22	766.85	2.054204	2.048288	2.052651	0.9646	0.9636	0.9620	0.9634	0.001312663
3	750.52	748.16	751.28	2.00894	2.002623	2.010975	0.9434	0.9421	0.9425	0.9427	0.000636996
3.5	748.44	745.97	748.92	2.003373	1.996761	2.004658	0.9407	0.9394	0.9395	0.9399	0.000756784
4	738.68	737.16	739.53	1.977248	1.973179	1.979523	0.9285	0.9283	0.9277	0.9282	0.000381359
4.5	730.11	726.74	733.61	1.954308	1.945288	1.963677	0.9177	0.9151	0.9203	0.9177	0.002581456

* concentrations were converted from absorbance by using linear calibration of benzo[a]anthracene.

Appendix Table H10 Raw data of the photodegradation of 20 ppm benzo[a]anthracene using 0.1 g of P-25 TiO_2.

Degrading time	Fluorescence at λ_{em} 527 nm			Concentration (ppm)			Relative concentration (C/C_o)				
(hrs)	F_1	F_2	F_3	C_1	C_2	C_3	C_1/C_o	C_2/C_o	C_3/C_o	$(C/C_o)_{ave}$	Std $_{(C/Co)}$
0.5	927.47	953.29	915.01	2.482588	2.551701	2.449236	1	1	1	1	5.636E-08
1	893.04	916.83	872.131	2.390428	2.454107	2.33446	0.9628	0.9617	0.9531	0.9592	0.005328
1.5	835.75	852.82	818.89	2.237078	2.28277	2.191948	0.9011	0.8946	0.8949	0.8968	0.003657
2	802.21	835.27	794.109	2.147301	2.235793	2.125616	0.8649	0.8761	0.8678	0.8696	0.005838
2.5	775.46	786.72	752.655	2.075698	2.105838	2.014655	0.8361	0.8252	0.8225	0.8279	0.007164
3	765.64	774.609	742.06	2.049412	2.07342	1.986295	0.8255	0.8125	0.8109	0.8163	0.007971
3.5	751.61	761.15	726.1922	2.011858	2.037394	1.943821	0.8103	0.7984	0.7936	0.8008	0.008621
4	742.02	757.28	715.4898	1.986188	2.027035	1.915174	0.8001	0.7943	0.7819	0.7921	0.009259
4.5	730.55	748.4665	701.0579	1.955486	2.003444	1.876544	0.7876	0.7851	0.7661	0.7796	0.011751

Appendix Table H11 Raw data of the photodegradation of 20 ppm benzo[a]anthracene using 0.1 g of 13.57 %wt Sm doped TiO_2 calcined at 500^{o}C.

Degrading time (hrs)	Fluorescence at λ_{em} 527 nm			Concentration (ppm)			Relative concentration (C/C_o)				
	F_1	F_2	F_3	C_1	C_2	C_3	C_1/C_o	C_2/C_o	C_3/C_o	$(C/C_o)_{ave}$	Std $_{(C/Co)}$
0.5	877.62	877.62	877.62	2.349153	2.349153	2.349153	1	1	1	1	1.359E-16
1	762.63	771.61	755.91	2.041355	2.065393	2.023368	0.8689	0.8792	0.8613	0.8698	0.008975
1.5	706.58	702.5	676.74	1.891325	1.880404	1.811451	0.8051	0.8004	0.7711	0.7922	0.018435
2	686.71	681.35	672.72	1.838138	1.823791	1.800691	0.7824	0.7763	0.7665	0.7751	0.008047
3	670.02	677.22	670.41	1.793463	1.812736	1.794507	0.7634	0.7716	0.7638	0.7663	0.004613
3.5	665.83	666.42	661.15	1.782248	1.783827	1.769721	0.7586	0.7593	0.7533	0.7571	0.003290
4	653.66	656.29	629.16	1.749672	1.756712	1.684092	0.7448	0.7478	0.7168	0.7365	0.017048
4.5	613.58	614.73	595.31	1.642389	1.645467	1.593485	0.6991	0.7004	0.6783	0.6926	0.012414

Appendix Table H12 Raw data of the photodegradation of 20 ppm phenol using 0.1 g of P-25 TiO_2.

Degrading time	Absorbance at λ_{max} 270 nm			Concentration* (ppm)			Relative concentration (C/C_o)				
(hrs)	Abs_1	Abs_2	Abs_3	C_1	C_2	C_3	C_1/C_o	C_2/C_o	C_3/C_o	$(C/C_o)_{ave}$	Std $_{(C/Co)}$
0.5	0.103631	0.144486	0.134216	6.4367	8.9743	8.3364	1	1	1	1	0
1	0.095829	0.142425	0.124492	5.952113	8.846255	7.732453	0.9247	0.9857	0.9275	0.9460	0.03443
1.5	0.094168	0.139956	0.122334	5.848926	8.692895	7.598402	0.9086	0.9686	0.9114	0.9296	0.03384
2	0.09277	0.137878	0.120518	5.762098	8.563848	7.485603	0.8951	0.9542	0.8979	0.9158	0.03333
2.5	0.092172	0.13699	0.119742	5.724976	8.508676	7.437377	0.8894	0.9481	0.8921	0.9099	0.03312
3	0.091524	0.136026	0.1189	5.684708	8.448828	7.385065	0.8831	0.9414	0.8858	0.9035	0.03289
3.5	0.090957	0.135183	0.118163	5.649474	8.396461	7.339291	0.8776	0.9356	0.8803	0.8979	0.03268
4	0.090146	0.133979	0.11711	5.599139	8.321651	7.2739	0.8698	0.9272	0.8725	0.8899	0.03239

* concentrations were converted from absorbance by using linear calibration of phenol.

Appendix Table H13 Raw data of the photodegradation of 20 ppm phenol using 0.1 g of undoped TiO_2.

Degrading time	Absorbance at λ_{max} 270 nm			Concentration (ppm)			Relative concentration (C/C_o)				
(hrs)	Abs_1	Abs_2	Abs_3	C_1	C_2	C_3	C_1/C_o	C_2/C_o	C_3/C_o	$(C/C_o)_{ave}$	Std $_{(C/Co)}$
0.5	0.094198	0.118226	0.100165	5.8508	7.3432	6.22142	1	1	1	1	0
1	0.093209	0.117351	0.099073	5.789367	7.28886	6.153607	0.9895	0.9926	0.9891	0.9904	0.00191
1.5	0.09205	0.116027	0.096589	5.717402	7.206616	5.999315	0.9772	0.9814	0.9643	0.9743	0.008911
2	0.090402	0.11378	0.093153	5.615013	7.067096	5.785921	0.9597	0.9624	0.9300	0.9507	0.01797
2.5	0.088386	0.109329	0.090654	5.489806	6.790624	5.630696	0.9383	0.92475	0.90505	0.9227	0.01672
3	0.084914	0.106297	0.089704	5.274145	6.602271	5.571655	0.90144	0.8991	0.89556	0.8987	0.00296
3.5	0.081396	0.103589	0.089097	5.055676	6.434112	5.533953	0.8641	0.8762	0.8895	0.8766	0.012705
4	0.082461	0.100622	0.082786	5.12179	6.249798	5.142004	0.8754	0.8511	0.8265	0.851	0.02445

Appendix Table H14 Raw data of the photodegradation of 20 ppm phenol using 0.1 g of 13.57 %wt Sm doped TiO_2 calcined at 500^oC.

Degrading time	Absorbance at λ_{max} 270 nm			Concentration (ppm)			Relative concentration (C/C_o)				
(hrs)	Abs_1	Abs_2	Abs_3	C_1	C_2	C_3	C_1/C_o	C_2/C_o	C_3/C_o	$(C/C_o)_{ave}$	Std $_{(C/Co)}$
0.5	0.090952	0.125954	0.134194	5.64927	7.82321	8.3350	1	1	1	1	0
1	0.08794	0.121336	0.136713	5.462128	7.536401	8.491488	0.9668	0.9633	1.0187	0.9830	0.03103
1.5	0.083224	0.114829	0.129381	5.169185	7.132211	8.036074	0.9150	0.9116	0.9641	0.9302	0.02936
2	0.078977	0.108969	0.122778	4.905398	6.76825	7.625988	0.8683	0.8651	0.9149	0.8828	0.02787
2.5	0.075648	0.104376	0.117604	4.698653	6.482992	7.30458	0.8317	0.8286	0.8763	0.8456	0.02669
3	0.074002	0.102105	0.115045	4.596411	6.341924	7.145634	0.8136	0.8106	0.8573	0.8272	0.02611
3.5	0.07324	0.101053	0.11386	4.549069	6.276603	7.072036	0.8052	0.8023	0.8484	0.8186	0.02584
4	0.070166	0.096811	0.10908	4.358115	6.013133	6.775176	0.7714	0.7686	0.8128	0.7843	0.02476

CIRRICULUM VITAE

NAME : Mr. Rattana Phatinavin

BIRTH DATE : June 30, 1983

BIRTH PLACE : Saraburi, Thailand

EDUCATION :	**YEAR**	**INSTITUTE**	**DEGREE/DIPLOMA**
	2005	Kasetsart Univ.	B.Sc. (Chemistry)

POSITION/TITLE : Graduated student

WORKPLACE : Faculty of Science, Kasetsart University

SCHOLARSHIP/AWARDS : Center for Innovation in Chemistry: Postgraduate Education and Research Program in Chemistry (PERCH-CIC)